



## **Terms and Conditions of Use of Digitised Theses from Trinity College Library Dublin**

### **Copyright statement**

All material supplied by Trinity College Library is protected by copyright (under the Copyright and Related Rights Act, 2000 as amended) and other relevant Intellectual Property Rights. By accessing and using a Digitised Thesis from Trinity College Library you acknowledge that all Intellectual Property Rights in any Works supplied are the sole and exclusive property of the copyright and/or other IPR holder. Specific copyright holders may not be explicitly identified. Use of materials from other sources within a thesis should not be construed as a claim over them.

A non-exclusive, non-transferable licence is hereby granted to those using or reproducing, in whole or in part, the material for valid purposes, providing the copyright owners are acknowledged using the normal conventions. Where specific permission to use material is required, this is identified and such permission must be sought from the copyright holder or agency cited.

### **Liability statement**

By using a Digitised Thesis, I accept that Trinity College Dublin bears no legal responsibility for the accuracy, legality or comprehensiveness of materials contained within the thesis, and that Trinity College Dublin accepts no liability for indirect, consequential, or incidental, damages or losses arising from use of the thesis for whatever reason. Information located in a thesis may be subject to specific use constraints, details of which may not be explicitly described. It is the responsibility of potential and actual users to be aware of such constraints and to abide by them. By making use of material from a digitised thesis, you accept these copyright and disclaimer provisions. Where it is brought to the attention of Trinity College Library that there may be a breach of copyright or other restraint, it is the policy to withdraw or take down access to a thesis while the issue is being resolved.

### **Access Agreement**

By using a Digitised Thesis from Trinity College Library you are bound by the following Terms & Conditions. Please read them carefully.

I have read and I understand the following statement: All material supplied via a Digitised Thesis from Trinity College Library is protected by copyright and other intellectual property rights, and duplication or sale of all or part of any of a thesis is not permitted, except that material may be duplicated by you for your research use or for educational purposes in electronic or print form providing the copyright owners are acknowledged using the normal conventions. You must obtain permission for any other use. Electronic or print copies may not be offered, whether for sale or otherwise to anyone. This copy has been supplied on the understanding that it is copyright material and that no quotation from the thesis may be published without proper acknowledgement.

# Anisotropic Discretisations and Practical All-to-All Propagators for Lattice QCD

by

Ailein Ó Cais

B.A. (Mod.), M.Sc.

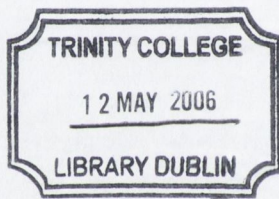
A Project submitted to  
The University of Dublin  
for the degree of

Doctor in Philosophy

School of Mathematics  
University of Dublin  
Trinity College



April, 2006

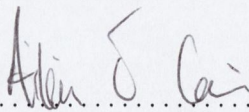


*THOS'S*  
*7842.*

## Declaration

This project has not been submitted as an exercise for a degree at any other University. Except where otherwise stated, the work described herein has been carried out by the author alone. This project may be borrowed or copied upon request with the permission of the Librarian, University of Dublin, Trinity College. The copyright belongs jointly to the University of Dublin and Ailein Ó Cais.

Signature of Author .....



Ailein Ó Cais  
10 April, 2006

## Summary

In this thesis, we concern ourselves primarily with improving the accuracy of the determination of correlation functions in lattice QCD. We detail two avenues of improvement and implement them both, separately and in combination.

Firstly, we formulate an improved anisotropic action which is classically correct to  $O(a_s^3, a_t^2)$ . The employment of an anisotropic lattice introduces the anisotropy ratio,  $\xi = a_s/a_t$ , which we tune non-perturbatively. In a quenched lattice simulation, we find that the mass dependence of the tuning of this parameter is weak, and a single tuning suffices for a range of quark masses from the strange quark mass to well above charm quark mass. The primary benefit of an anisotropic action is that it allows us an increased number of lattice sites in the temporal direction with which to study the exponential decay of correlation functions.

The second improvement we apply is in the accuracy of the determination of the correlation function itself. This involves the computation of the full lattice Feynman propagator, or *all-to-all* propagator.

We propose and implement a novel procedure for the calculation of the all-to-all propagator. This is a hybrid method that combines the dominating effects of the low-lying fermion modes (for light quarks) with a stochastic estimation technique, *dilution*, that gives the exact inverse in a finite number of steps. This maintains the reflection positivity of the propagator, which in turn allows us to apply variational techniques in our determination of effective masses of correlation functions.

In quenched Wilson simulations, we find that it is possible to dramatically reduce the errors of correlation functions with different dilution combinations, and ultimately to a level of gauge field noise. The dominance of the low-lying eigenmodes was found to depend strongly on the quark mass but, for sufficiently light quarks, their use in union with a diluted stochastic correction gave even further decreases in error, particularly for traditionally noisy states.

Using the two methods in combination we find that it is possible to achieve high accuracy mass determinations for all states attempted, including a hybrid exotic meson. The level of accuracy achievable also allows the extraction of both a first and second excited state in a static-light study using the variational technique.

Use of the all-to-all propagator technique also allows us to evaluate disconnected diagram contributions to both the  $0^{++}$  and  $0^{-+}$  isoscalar mesons and extract effective mass for both these states.

## Acknowledgements

I would like to thank all those who helped me directly and indirectly in completing this thesis. Not too surprisingly, first and foremost I'd like to thank my supervisor Dr. Mike Peardon. If it wasn't for his ideas, insight and guidance there would be a lot more pressing issues than writing these acknowledgments. I'm also indebted to the rest of the Trinlat group, many hands make light work, so thanks to Sinéad, Jimmy, Justin, Jon-Ivar, Richie, Bugra and Waseem.

Ba mhaith liom buíochas a ghabháil le chuile duine a bhíonn bainteach le mo shaol laethúil freisin. Ní bheinn comh sona sásta seo gan sibh. Go háirithe caithfidh mé buíochas a ghabháil le mo chlann Mum, Dad, PJ, Karina, Michelle agus Philip agus na leaids go léir ins an choláiste Daithí, Tina, Karen, Mick, Eabh, Shane, Taylor, Eoin agus Dan agus na leaids, atá agus a bhí, ins an Chlub Dornálaíochta agus an Chlub Taekwon-do. Ansin tá na daoine nach bhfuil sé comh easca sin teacht orthu a thuile, Eoin Ó hÓgáin agus na daoine eile ón Choláiste, Eoin Whelan, Peter Mac agus an KK crew, Richie O'D (agus Amy), Sarah agus Eoin Pól. Mura bhfuil d'ainm san áireamh, tá brón orm ach ná bí buartha, ní dóigh liom gur best-seller atá scríobhtha agam.

*Do mo thuistí,  
Ní saol gan grá.*

# Contents

<b>1</b>	<b>Introduction</b>	<b>1</b>
1.1	$SU(3)$ Gauge Fields on the Lattice . . . . .	4
1.2	Quark Fields on the Lattice . . . . .	6
1.2.1	Wilson Quarks . . . . .	8
1.3	Observables in Lattice QCD . . . . .	10
<b>2</b>	<b>QCD on an Anisotropic Lattice</b>	<b>12</b>
2.1	Improved Gauge Action . . . . .	12
2.1.1	Gauge Actions on Anisotropic Lattices . . . . .	13
2.1.2	Symanzik Improvement . . . . .	15
2.1.3	Tadpole Improvement . . . . .	17
2.1.4	Further Improvement . . . . .	20
2.2	Improved Dirac Action . . . . .	22
2.2.1	The Class of D234 Actions . . . . .	22
2.2.2	D234 Actions on Anisotropic Lattices . . . . .	26
2.2.3	ARIA . . . . .	27
2.2.4	Analytic results for ARIA . . . . .	29
2.3	Tuning . . . . .	32
2.3.1	Tuning the Anisotropies in a Quenched Simulation . . . . .	32
2.3.2	Tuning the Anisotropy in a Dynamical Simulation . . . . .	37
2.3.3	Other parameters . . . . .	38
<b>3</b>	<b>Propagators</b>	<b>39</b>
3.1	Point-to-All Propagators . . . . .	40

3.2	All-to-All Propagators . . . . .	43
3.3	Stochastic Estimation . . . . .	45
3.3.1	Noise Reduction with Subspace Thinning . . . . .	47
3.3.2	Dilution . . . . .	49
3.3.3	Recycling Noise Vectors . . . . .	59
3.4	Truncated Spectral Decomposition . . . . .	59
3.4.1	Extracting Low-lying Modes . . . . .	60
3.5	A Hybrid Method . . . . .	66
<b>4</b>	<b>Correlation Functions . . . . .</b>	<b>75</b>
4.1	Meson Operators . . . . .	76
4.2	Mesonic Interpolating Operators . . . . .	78
4.2.1	Hybrid Mesons . . . . .	82
4.3	Smearing . . . . .	85
4.4	Variational Approach . . . . .	86
4.5	Isvector Mesons . . . . .	88
4.5.1	Dynamical Simulation . . . . .	89
4.5.2	Static-light Mesons . . . . .	94
4.6	Isoscalar mesons . . . . .	95
4.6.1	Flavour Singlet Correlation Functions . . . . .	97
4.6.2	Mixing of Scalar Glueballs and Flavour-Singlet Scalar Mesons . . . . .	101
<b>5</b>	<b>Conclusions . . . . .</b>	<b>104</b>
<b>A</b>	<b>Appendix - Algorithm Implementation . . . . .</b>	<b>107</b>
A.1	Propagator Data . . . . .	107
A.2	Meson Operators . . . . .	108
A.3	Correlation Functions . . . . .	110
A.4	A Black Box . . . . .	111
	<b>References . . . . .</b>	<b>112</b>

# List of Figures

1-1	An elementary Wilson loop . . . . .	5
2-1	ARIA free field dispersion relations . . . . .	31
2-2	Example of an effective mass plot and a dispersion relation . . . . .	34
3-1	Schematic of a 2-point correlation function . . . . .	42
3-2	Schematic of a the disconnected contribution to a 2-point correlation function . . . . .	43
3-3	Cartoon of the noise contributions to the stochastic estimate of a matrix inverse . . . . .	46
3-4	Pseudoscalar propagator computed with and without temporal subspace thinning. . . . .	48
3-5	Cartoon of possible deviations of the stochastic estimates of the exact solution for different dilution paths . . . . .	50
3-6	Dilution dependence of the pion for the $4^3 \times 8$ Wilson simulation . . .	54
3-7	Dilution dependence of the pion with a momentum injection for the $4^3 \times 8$ Wilson simulation . . . . .	55
3-8	Dilution dependence of the $\rho$ meson for the $4^3 \times 8$ Wilson simulation	56
3-9	Dilution dependence of the $1^{++}$ P-state for the $4^3 \times 8$ Wilson simulation	57
3-10	Eigenmode dependence of the $\pi$ , $\rho$ and $1^{++}$ mesons for the $4^3 \times 8$ and $4^3 \times 4$ Wilson simulations . . . . .	63
3-11	Pion correlation function determined using eigenvectors and also dilution on the $4^3 \times 8$ and $12^3 \times 24$ Wilson simulations . . . . .	65
3-12	Recovery of reflection positivity with the hybrid method . . . . .	69

3-13	Error behaviour (at $t = 3$ ) of the pion on the $12^3 \times 24$ Wilson simulation using dilution and the hybrid method . . . . .	71
3-14	Error behaviour (at $t = 3$ ) of the $\rho$ meson on the $12^3 \times 24$ Wilson simulation using dilution and the hybrid method . . . . .	71
3-15	Error behaviour (at $t = 3$ ) of the $1^{++}$ meson on the $12^3 \times 24$ Wilson simulation using dilution and the hybrid method . . . . .	73
3-16	Comparison of point and hybrid method propagators . . . . .	73
4-1	Effective masses for isovector mesons using the hybrid method in the $12^3 \times 24$ Wilson simulation . . . . .	89
4-2	Effective masses for isovector mesons for the dynamical $8^3 \times 48$ ARIA simulation. . . . .	91
4-3	The ground and first excited states of the $T_1^{+-}$ and $T_1^{++}$ lattice operators	93
4-4	Effective masses for the $\rho$ ( $1^{--}$ ) meson using the three different interpolating operators . . . . .	93
4-5	Effective masses for the three lowest-lying states of the static-light S-wave. . . . .	94
4-6	Schematic of contributions to the propagator . . . . .	97
4-7	Vacuum effects on disconnected diagrams . . . . .	98
4-8	Effective masses for isovector and isoscalar $0^{-+}$ meson in the dynamical $8^3 \times 48$ ARIA simulation . . . . .	99
4-9	Effective masses for isovector and isoscalar $0^{++}$ meson in the dynamical $8^3 \times 48$ ARIA simulation . . . . .	100
4-10	Correlation of the mixing of the $0^{-+}$ glueball with the $0^{-+}$ flavour-singlet meson. . . . .	102
4-11	Correlation of the mixing of the $0^{++}$ glueball with the $0^{++}$ flavour-singlet meson. . . . .	103

# List of Tables

2.1	Details of the quenched $10^3 \times 120$ ARIA simulation . . . . .	35
2.2	Speed of light determinations for a variety of degenerate quark masses in the quenched ARIA simulation . . . . .	36
2.3	Speed of light determinations for a variety of non-degenerate quark masses in the quenched ARIA simulation . . . . .	37
3.1	Dilutions available and their reference codes . . . . .	52
3.2	Parameters of the $4^3 \times 8$ quenched Wilson simulation . . . . .	52
3.3	Dilutions employed in the $4^3 \times 8$ quenched Wilson simulation . . . . .	53
3.4	Parameters of the $4^3 \times 4$ quenched Wilson simulation . . . . .	62
3.5	Details of the quenched $12^3 \times 24$ Wilson simulation . . . . .	70
3.6	Dilutions used on the $12^3 \times 24$ Wilson simulation . . . . .	70
4.1	The 16 independent $\gamma$ -matrix bilinears . . . . .	79
4.2	Subduction of the $SU(2)$ rotation group to $O_h$ . . . . .	80
4.3	Clebsch-Gordan decomposition of the product of $T_1$ with the $O_h$ rep- resentations . . . . .	81
4.4	$O_h$ representations given by a straight line path along a lattice axis joining the quark and antiquark. . . . .	81
4.5	$O_h$ representations given by some of the combinations of the quark bilinears with straight-path representations . . . . .	82
4.6	Interpolating operators used and the $J$ values corresponding to their $O_h$ representations. . . . .	84
4.7	Run parameters for the dynamical $8^3 \times 48$ ARIA simulation. . . . .	90

4.8	Effective masses for isovector mesons for the dynamical $8^3 \times 48$ ARIA simulation . . . . .	92
-----	---	----

# Chapter 1

## Introduction

The Standard Model of particle physics is a theory which describes the strong, weak, and electromagnetic fundamental forces, as well as the fundamental particles that make up all matter. Developed between 1970 and 1973, it is a quantum field theory, and consistent with both quantum mechanics and special relativity. To date, almost all experimental tests of the three forces described by the Standard Model have agreed with its predictions. However, the Standard Model is not a complete theory of fundamental interactions, primarily because it does not describe gravity.

Quantum chromodynamics (QCD) is the theory describing one of these fundamental forces, the strong interaction. It describes the interactions of quarks (massive spin-1/2 fermions) and gluons (spin-1 bosons), each of which carry a *colour charge*. QCD is a gauge theory of the SU(3) gauge group obtained by taking the colour charge to define a local symmetry.

The Lagrangian of QCD (with colour, flavor and spin indices suppressed) looks exactly like that of QED:

$$L = -\frac{1}{4}F_{\mu\nu}F_{\mu\nu} + \bar{\psi}(i\gamma_{\mu}D_{\mu} - M)\psi \quad (\text{summation over } \mu, \nu \text{ understood}) \quad (1.1)$$

where  $F$  denotes the gluon field tensor,  $\psi$  the quark field,  $D$  the covariant derivative and  $\gamma_{\mu}$  are  $4 \times 4$  Dirac matrices satisfying the anticommutation relations

$$\{\gamma_{\mu}, \gamma_{\nu}\} = 2g_{\mu\nu}. \quad (1.2)$$

Part of its content lies in the Feynman rules which state that all processes which occur in the theory can be resolved into the elementary interactions (called vertices). A quark may emit (or absorb) a gluon, a gluon may emit (or absorb) a gluon, and two gluons may directly interact. In QED, only the first kind of vertex occurs, since photons have no charge.

Among non-perturbative approaches to QCD, the most well established one is lattice QCD (for detailed reviews see Ref. [1, 2]). Lattice Quantum Chromodynamics (Lattice QCD) is the theory of quarks and gluons formulated on a space-time lattice. The formulation of quantum chromodynamics on a discrete rather than continuous space-time resolves many difficulties (e.g. divergences) associated with the continuum field theories. Most importantly, Lattice QCD provides the framework for the investigation of non-perturbative phenomena, such as confinement, which are intractable by means of analytic field theories. While it is a slow and resource-intensive approach, it has wide applicability, giving insight into parts of the theory inaccessible by other means.

Lattice field theory can be thought of as a quantisation procedure for a field theory. It has the advantage that it is not restricted to being a perturbative method, and can easily deal with trivial as well as complicated vacuum states of quantum field theories. Usually the method is applied to numerical computation of quantum amplitudes.

The method is particularly appealing for the quantisation of a gauge theory. Most quantisation methods keep Poincare invariance manifest but sacrifice manifest gauge symmetry by requiring gauge fixing. Only after renormalisation can gauge invariance be recovered. Lattice field theory differs from these in that it keeps manifest gauge invariance, but sacrifices manifest Poincare invariance - recovering it only after renormalisation.

In lattice gauge theory the first step is to Wick rotate the spacetime into Euclidean

space. The Euclidean form of the QCD action is given by

$$\begin{aligned}
S^E &= S_G^E + S_F^E \\
&= \frac{1}{4} \int d^4x F_{\mu\nu} F_{\mu\nu} + \int d^4x \bar{\psi}(x) (\gamma_\mu^E \partial_\mu + M) \psi(x),
\end{aligned} \tag{1.3}$$

where the superscript  $E$  denotes the Euclidean formulation and we have taken the hermitean choice  $\gamma_0^E = \gamma_4$  and  $\gamma_i^E = -i\gamma_i$ . From now on we are interested only in the Euclidean formulation so we shall drop the label reminding us of this.

Euclidean spacetime is then discretised and replaced by a lattice. The relative position of each lattice site is given by

$$x_\mu = n_\mu a_\mu, \quad n_\mu \in \mathbb{Z}, \quad 0 \leq n_\mu < N_\mu \tag{1.4}$$

where the lattice spacing along the direction denoted  $\mu$  is equal to  $a_\mu$  and  $N_\mu$  is the number of sites along that direction. The hypercubic lattice possesses a discrete translational symmetry which requires that energy and momenta occur in discrete units. The allowed momenta are

$$p_\mu = \frac{2\pi n_\mu}{N_\mu a_\mu}. \tag{1.5}$$

Discretising space-time, therefore, imposes a cutoff corresponding to the minimum physical distance which can be modeled on a discrete grid and the lattice acts as an ultra-violet regulator for QCD.

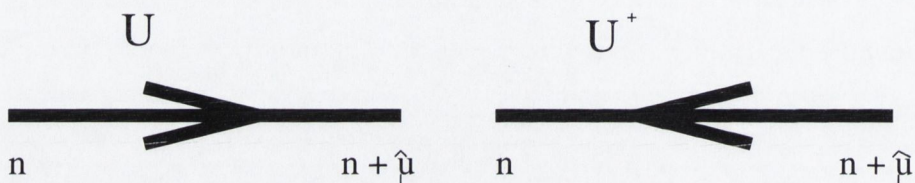
The quark fields are only defined at the elements of the lattice. Instead of a vector potential as in the continuum case, the gauge fields variables are defined on the links of the lattice and correspond to the parallel transport along the edge which takes on values in the Lie group. The faces of the lattice are called plaquettes. More precisely, we have a lattice with vertices, edges and faces. In lattice theory, the alternative terminology sites, links and plaquettes for vertices, edges and faces is most commonly used.

## 1.1 $SU(3)$ Gauge Fields on the Lattice

To simulate QCD, for which the Lie group is  $SU(3)$ , there is a  $3 \times 3$  special unitary matrix defined on each link  $U$  connecting two neighbouring lattice sites where

$$U_{n+\hat{\mu},n} = U_{n,n+\hat{\mu}}^+ \quad (1.6)$$

This gives us the graphical representations,



These matrix-valued link variables can be written in the form (with no summation),

$$U_{\mu}(n) \equiv U_{n,n+\hat{\mu}} = e^{ig_0 a_{\mu} A_{\mu}(n)} \quad \text{where} \quad ig_0 a_{\mu} A_{\mu}(n) \in \text{Lie Algebra of } SU(3), \quad (1.7)$$

and  $A_{\mu}(n)$  is a dimensioned matrix valued lattice field,  $a_{\mu}$  is the lattice spacing in the  $\hat{\mu}$  direction and  $g_0$  is a bare coupling constant. They are invariant under the local gauge transformations

$$\begin{aligned} U_{\mu}(n) &\rightarrow G(n)U_{\mu}(n)G^{-1}(n+\hat{\mu}) \\ U_{\mu}^{\dagger}(n) &\rightarrow G(n+\hat{\mu})U_{\mu}^{\dagger}(n)G^{-1}(n) \end{aligned} \quad (1.8)$$

where  $G(n)$  is an element of  $SU(3)$  in the fundamental representation.

A Wilson loop is the trace of a path ordered product of link variables around a closed loop. It is a gauge invariant quantity. The simplest of these loops is the Wilson loop around an elementary plaquette (see Fig. (1-1))

$$U_{\mu\nu}(n) = \text{Tr}[U_{\mu}(n)U_{\nu}(n+\hat{\mu})U_{\mu}^{\dagger}(n+\hat{\nu})U_{\nu}^{\dagger}(n)] \quad (1.9)$$

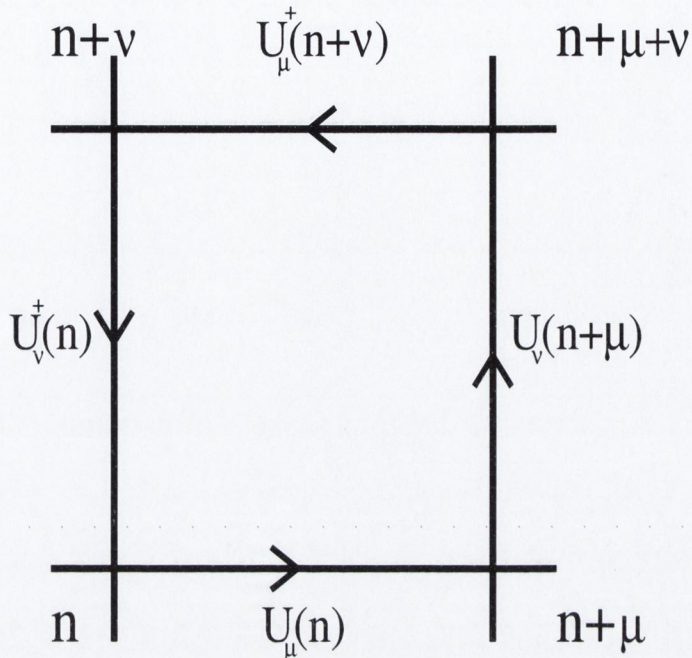


Figure 1-1: The Wilson loop  $U_{\mu\nu}(n)$  of an elementary plaquette with base at  $n$  lying in the  $\mu\nu$ -plane.

The Yang-Mills action is rewritten using Wilson loops over plaquettes in such a way that the limit  $a_{\mu} \rightarrow 0$  formally gives the original continuous action.

There are many possible lattice Yang-Mills actions, depending on which Wilson loop is used. The simplest is the Wilson action, in which the Wilson loop is just around an elementary plaquette. The Wilson action is given by

$$S_G^{SU(3)}[U] = \beta \sum_{x, \mu > \nu} \frac{1}{3} \text{ReTr}[1 - U_{\mu\nu}(x)] \quad (1.10)$$

where the sum is over all elementary distinct plaquettes and  $\beta$  is defined as  $6/g_0^2$ . Taking the real part of the trace is equivalent to averaging over the plaquette and its charge conjugate and ensures the hermiticity of the action.

A disadvantage of the Wilson action is that the leading correction between it and the continuous action is  $O(a_{\mu}^2)$ , which we can see by Taylor expansion of the gauge links in Eq. (1.10). It is possible to use more complicated Wilson loops to form actions where this correction is  $O(a_{\mu}^3)$  or smaller, thus making computations more

accurate. These are known as improved actions. This comes at the cost of extending the locality of the computation of the action which is computationally expensive.

## 1.2 Quark Fields on the Lattice

The matter fields  $\psi(x)$  are represented by anticommuting Grassmann variables defined at each site of the lattice. They transform according to the fundamental representation of  $SU(3)$ . The effect of the local gauge transformation,  $G(n)$  of Eq. (1.8), on the variables  $\psi(n)$  is defined to be

$$\begin{aligned}\psi(n) &\rightarrow G(n)\psi(n) \\ \bar{\psi}(n) &\rightarrow \bar{\psi}(n)G^\dagger(n).\end{aligned}\tag{1.11}$$

Apart from a Wilson loop, another gauge invariant object is a string consisting of a path-ordered product of links capped by a fermion and an antifermion. Similar to the gauge action, we build a gauge invariant quark action from these gauge invariant objects. We note, again, that these objects can be of arbitrary size and shape, the only constraint is that the action gives the familiar continuum theory in the limit of  $a_\mu \rightarrow 0$ .

To discretise the Dirac action in Eq. (1.3), we replace the covariant derivative with a symmetrized difference, and include appropriate gauge links to maintain gauge invariance

$$\bar{\psi}\not{D}\psi = \bar{\psi}(n) \sum_\mu \frac{1}{2a_\mu} \gamma_\mu [U_\mu(n)\psi(n + \hat{\mu}) - U_\mu^\dagger(n - \hat{\mu})\psi(n - \hat{\mu})].\tag{1.12}$$

We use a symmetrized difference to ensure an hermitian action. This is called the *naive* lattice action for fermions. If we Taylor expand the gauge and quark fields we can see that it is, to  $O(a_\mu^2)$  the kinetic part of the standard continuum Dirac action of Eq. (1.3). Thus, we arrive at what is called the simplest (*naive*, denoted by  $N$ )

lattice action for fermions,

$$S_F^N = m_q \sum_n \bar{\psi}(n)\psi(n) + \sum_{n,\mu} \frac{1}{2a_\mu} \bar{\psi}(n)\gamma_\mu [U_\mu(n)\psi(n + \hat{\mu}) - U_\mu^\dagger(n - \hat{\mu})\psi(n - \hat{\mu})] \quad (1.13)$$

$$\equiv \sum_n \bar{\psi}(n) M_{nm}^N[U] \psi(m), \quad (1.14)$$

where the interaction, or Dirac, matrix  $M^N$  is

$$M_{nm}^N[U] = m_q \delta_{nm} + \sum_\mu \frac{1}{2a_\mu} [\gamma_\mu U_\mu(n) \delta_{n+\hat{\mu},m} - \gamma_\mu U_\mu^\dagger(n - \hat{\mu}) \delta_{n-\hat{\mu},m}]. \quad (1.15)$$

The invariance group of the fermion action under rotations in space and time is the hypercubic group. Full Euclidean invariance will only be recovered in the continuum limit. The action is invariant under translations by  $a_\mu$  in the  $\hat{\mu}$  direction, as well as space inversion, time reversal and charge conjugation. In the limit  $m_q \rightarrow 0$ , it is also invariant under chiral transformations

$$\begin{aligned} \psi(n) &\rightarrow e^{i\theta\gamma_5} \psi(n) \\ \bar{\psi}(n) &\rightarrow \bar{\psi}(n) e^{i\theta\gamma_5}. \end{aligned} \quad (1.16)$$

Massless quarks do not exist but the  $u$ ,  $d$ ,  $s$  quarks are light enough to preserve an approximate chiral symmetry.

The problem with this naive discretisation of the Dirac action is that it gives rise to 16 flavours of fermions rather than one. We can demonstrate this if we take the fourier transform of the action with all  $U_\mu(n) = 1$  and calculate the inverse of the free field propagator

$$S^{-1}(p) = m_q + \sum_\mu \frac{i}{a_\mu} \gamma_\mu \sin p_\mu a_\mu. \quad (1.17)$$

This has 16 zeros within the Brillouin cell in the limit  $m_q \rightarrow 0$ . If we define the momentum range of the Brillouin cell to be  $-\pi/2, 3\pi/2$ , the zeros lie at  $p_\mu = 0$  and  $\pi$ . Removing these *doublers* is problematic since their presence is a pathology of the

lattice and intimately related to chiral symmetry. In fact, the Nielsen-Ninomiya no-go theorem [3] states that it is not possible to define a local, translationally invariant, hermitian lattice action that preserves chiral symmetry and does not have doublers.

### 1.2.1 Wilson Quarks

We have said that the lattice action is not unique and we can add an arbitrary number of irrelevant operators since these do not change the continuum limit. Wilsons solution to the doubling problem was to add a dimension five operator,  $\frac{r_\mu}{2} a_\mu \bar{\psi} \Delta_\mu \psi$  where  $\Delta_\mu$  is the second order lattice derivative in the  $\mu$  direction. The extra fifteen species at  $p_\mu = \pi$  get a mass proportional to  $r_\mu/a_\mu$  [4]. These masses diverge as we take the continuum limit and eventually decouple completely from the theory. For simplicity we shall assume an isotropic lattice,  $a_\mu = a$ , with identical Wilson parameters,  $r_\mu = r$ . The Wilson action, with these simplifications, is given by

$$\begin{aligned}
S^W &= m_q \sum_n \bar{\psi}(n) \psi(n) \\
&\quad + \frac{1}{2a} \sum_{n,\mu} \bar{\psi}(n) \gamma_\mu [U_\mu(n) \psi(n + \hat{\mu}) - U_\mu^\dagger(n - \hat{\mu}) \psi(n - \hat{\mu})] \\
&\quad - \frac{r}{2a} \sum_{n,\mu} \bar{\psi}(n) [U_\mu(n) \psi(n + \hat{\mu}) - 2\psi(n) + U_\mu^\dagger(n - \hat{\mu}) \psi(n - \hat{\mu})] \\
&= \frac{m_q a + 4r}{a} \sum_n \bar{\psi}(n) \psi(n) \\
&\quad + \frac{1}{2a} \sum_{n,\mu} \bar{\psi}(n) [(\gamma_\mu - r) U_\mu(n) \psi(n + \hat{\mu}) - (\gamma_\mu + r) U_\mu^\dagger(n - \hat{\mu}) \psi(n - \hat{\mu})] \\
&\equiv \sum_{n,m} \bar{\psi}^L(n) M_{nm}^W \psi^L(m) \tag{1.18}
\end{aligned}$$

where the interaction matrix  $M^W$  can be written as

$$M_{nm}^W[U]a = \delta_{nm} - \kappa \sum_\mu [(r - \gamma_\mu) U_\mu(n) \delta_{n+\mu,m} + (\gamma_\mu + r) U_\mu^\dagger(n - \hat{\mu}) \delta_{n-\mu,m}] \tag{1.19}$$

with the rescaling

$$\begin{aligned}\kappa &= 1/(2m_q a + 8r) \\ \psi^L &= \sqrt{(m_q a + 4r)}\psi = \psi/\sqrt{2\kappa}.\end{aligned}\tag{1.20}$$

We can interpret this form of the Wilson action as a statistical mechanics model. The local term acts like an inertia keeping the fermion at the same site while the non-local term makes the fermion hop to the nearest neighbour site with strength  $\kappa$ . During this hop the fermion acquires a twist by  $(\gamma_\mu - r)$  and by  $U_\mu$  in colour space. The case  $r = 1$  is a special case as the spin twist  $1 \pm \gamma_\mu$  is a projection operator of rank 2, and for this choice the dispersion relation determined from the free field theory has a single branch, i.e., there are no doublers in the free field limit.

The removal of doublers by the Wilson term comes at a heavy cost however. Wilson fermions explicitly break chiral symmetry at  $O(a)$ . This is a big issue for simulations of light quarks. Other formulations, such as staggered fermions or domain wall fermions, attempt to retain some form of chiral symmetry but suffer from their own complications.

To calculate a quantity (such as the mass of a particle) in lattice gauge theory, it should be calculated for every possible value of the gauge field on each link, and then averaged. In practice this is impossible. Instead the Monte Carlo method is used to estimate the quantity. Random configurations (values of the gauge fields) are generated with probabilities proportional to  $e^{-S_G + \log(\det M)}$ , where  $S$  is the lattice gauge action and  $M$  is the Dirac matrix for that configuration. The quantity is calculated for each configuration. The true value of the quantity is then found by taking the average of the value from a large number of configurations. To find the value of the quantity in the continuous theory this is repeated for various values of  $a$  and extrapolated to  $a = 0$ .

### 1.3 Observables in Lattice QCD

Lattice QCD calculations are a non-perturbative implementation of path integrals using the Feynman path integral approach. The calculations proceed exactly as if the field theory was being solved analytically had we the ability to do the calculations. The starting point is the partition function on a Euclidean space-time lattice

$$Z = \int \mathcal{D}U \mathcal{D}\psi \mathcal{D}\bar{\psi} e^{-S} \quad (1.21)$$

where  $\mathcal{D}U$  is the Haar measure,  $S$  is the continuum Euclidean QCD action

$$S = \int d^4x \left( \frac{1}{4} F_{\mu\nu} F_{\mu\nu} - \sum_f \bar{\psi} M_f \psi \right) \quad (1.22)$$

and  $M_f$  is the Dirac operator for quark flavour  $f$ . Since the fermions are represented by Grassmann variables  $\psi$  and  $\bar{\psi}$ , these can be integrated out exactly and we get the result

$$Z = \int \mathcal{D}U e^{\int d^4x \left( -\frac{1}{4} F_{\mu\nu} F_{\mu\nu} \right) + \sum_f \log(\det M_f)} = \int \mathcal{D}U e^{-\tilde{S}}. \quad (1.23)$$

where the fermionic contribution is now contained in the highly non-local term  $\det M_f$  and the partition function is only an integral over the background gauge configurations.

Results for physical observables are obtained by calculating expectation values

$$\langle \mathcal{O} \rangle = \frac{1}{Z} \int \mathcal{D}U \mathcal{O} e^{-\tilde{S}}, \quad (1.24)$$

where  $\mathcal{O}$  is any given combination of operators expressed in terms of time-ordered products of gauge and quark fields. In the path-integral approach these correspond to time-ordered correlation functions. In practice, the quark fields are re-expressed in terms of quark propagators using Wick's Theorem for contracting fields. In this way all dependence on quarks as dynamical fields is removed. For fermionic quantities the basic building block is, therefore the Feynman propagators, which are the inverses of the Dirac operators  $M_f$ .

We can use a Monte Carlo method to then perform the integration of Eq. (1.24). Using our lattice formulations of the gauge and quark actions, we generate an ensemble of gauge configurations,  $U$ , according to the probability distribution  $e^{-\tilde{S}}$ , and take the ensemble average of the observable  $\mathcal{O}(U)$ .

We shall concern ourselves with extraction of accurate physical results from correlation functions of the form of Eq. (1.24). We shall define improved gauge and quark actions to reduce the lattice spacing dependence of the error of our lattice actions. These improved actions shall be defined on *anisotropic* lattices with an increased number of lattice sites in the temporal direction. As we will see, the signal from the observable decays according to  $e^{-E_n t}$ , where  $E_n$  are the energy levels of the observable. The main advantage of an anisotropic lattice is that it allows us a larger temporal window to study this decay. At sufficiently large  $t$  the signal should be dominated by the lowest energy level,  $E_0$ . In particular, the anisotropic lattice allows us a larger number of temporal sites to study this large  $t$  region and accurately extract  $E_0$  from the correlation function.

The Wick contraction procedure introduces the Feynman propagator, which is the inverse of the Dirac operator  $M_f$ . Since the size of the Dirac operator scales as the square of the lattice volume, this inversion becomes computationally unfeasible at current lattice volumes. This problem is avoided in standard calculations by the use of *point-propagator* techniques, which relaxes the requirement of a full inversion to that of the calculation of a single column of the inverse, but at the cost of sacrificing the self-averaging effects of translational invariance on the correlation function. We shall propose a method for the estimation of the full propagator which combines its spectral decomposition, truncated to lowest-lying modes, with a stochastic estimation procedure. The stochastic estimator technique uses a sub-space thinning method to dramatically reduce the variance of our estimate.

# Chapter 2

## QCD on an Anisotropic Lattice

### 2.1 Improved Gauge Action

For all  $N > 1$ , the gauge part of the lattice QCD Wilson action is given by

$$S_G^{SU(N)}[U] = \beta \sum_{x, \mu > \nu} \left[ 1 - \frac{\text{Tr}}{2N} (U_{\mu\nu}(x) + U_{\mu\nu}^\dagger(x)) \right] \quad (2.1)$$

where  $\beta = \frac{2N}{g_0^2}$ .

For  $SU(N \geq 3)$  the trace of any Wilson loop in the fundamental representation is complex, with the two possible path-orderings giving complex conjugate values. Thus, taking the real part is equivalent to averaging the loop and its charge conjugate. For  $SU(3)$  we may write,

$$S_G^{SU(3)}[U] = \beta \sum_{x, \mu > \nu} \frac{1}{3} \text{ReTr}[1 - U_{\mu\nu}(x)] \quad (2.2)$$

If we examine the plaquette,  $U_{\mu\nu}(x)$ , by means of Stokes theorem [5],

$$\oint_{\square} A \cdot dx = \int_{-\frac{a}{2}}^{\frac{a}{2}} dx_\mu dx_\nu [\partial_\mu A_\nu(x_0 + x) - \partial_\nu A_\mu(x_0 + x)] \quad (2.3)$$

$$= a^2 F_{\mu\nu}(x_0) + \frac{a^2}{24} (D_\mu^2 + D_\nu^2) F_{\mu\nu}(x_0) + O(a^6, A^2) \quad (2.4)$$

we find that Eq. (2.2) has the correct limit for small lattice spacings up to corrections

of order  $a^2$ :

$$S_G^{SU(3)} = \int d^4x \sum_{\mu,\nu} \left\{ \frac{1}{2} \text{Tr} F_{\mu\nu}^2 + \frac{a^2}{24} \text{Tr} F_{\mu\nu} (D_\mu^2 + D_\nu^2) F_{\mu\nu} + \dots \right\} \quad (2.5)$$

The higher dimensional operators in this equation are suppressed by powers of the lattice spacing and are therefore irrelevant operators.

The choice of lattice action is not unique and one is free to add any irrelevant operator with a sensible strength and still recover the continuum limit. Symanzik's improvement program [6] employs this strategy to reduce discretisation errors. The single most important determinant of the cost of a lattice QCD simulation is the lattice spacing,  $a$ , and the cost varies roughly as  $(\frac{1}{a})^6$  [5]. Improving the gauge action beyond  $O(a^2)$  allows access to continuum physics on coarser lattices and consequently reduces simulation time for a given accuracy.

The representation of the gauge fields by the links of Eq. (1.7) gives rise to lattice artifacts due to the presence of higher order terms of  $g_0 a A_\mu$  and the  $A_\mu$ 's if contracted with each other generate tadpole contributions. Parisi, Lapage and Mackenzie, in [7, 8], proposed a mean-field improvement to reduce the effect of these artifacts. Morningstar and Peardon, in [9], found that the use of analytic smearing of the link variables in the generation of the gauge fields also minimised the tadpole contributions.

These improvements shall be briefly explained and discussed in the context of an anisotropic formalism outlined below.

### 2.1.1 Gauge Actions on Anisotropic Lattices

Once the gauge degrees of freedom and the action have been defined, the expectation value of any observable  $O[U]$  can be determined by the computation of the path integral

$$\langle \mathcal{O} \rangle = \frac{1}{\mathcal{Z}} \int D[U] \mathcal{O}[U] e^{-\tilde{S}[U]}, \quad (2.6)$$

where  $\mathcal{Z} = \int D[U] e^{-\tilde{S}[U]}$  is the partition function and  $D[U] = \prod_{x,\mu} dU_\mu(x)$  is the Haar measure. Expectation values in the path integral approach correspond to time-

ordered correlation functions.

The high dimensional integral is then evaluated by means of a stochastic Monte-Carlo method as an average over an ensemble of  $n$  representative gauge configurations

$$C_i = U_\mu^i(x)_{i=1\dots n},$$

$$\langle \mathcal{O} \rangle = \frac{1}{n} \sum_{i=1}^n \mathcal{O}[C_i] + \Delta O\left(\frac{1}{\sqrt{n}}\right). \quad (2.7)$$

While the use of improved actions makes accurate simulations on coarse lattices possible, for some calculations, such as glueball masses [10], the coarseness of the temporal lattice spacing can be a severe drawback, greatly reducing the number of time intervals which can be measured. This problem can be circumvented by using anisotropic lattices in which the temporal lattice spacing is much smaller than that in the spatial directions, enabling one to exploit the enhanced signal-to-noise ratio of the correlation functions at smaller temporal separations. In fact, anisotropic lattices will be useful whenever one is faced with a four-momentum in which one component is unusually large, such as in the calculation of glueball masses [11], the heavy quarkonium spectrum [62], or hadronic form factors at large momentum transfers.

If we define the spatial ( $sp$ ) and temporal ( $tp$ ) plaquettes

$$U_{sp} = U_i(x)U_j(x+\hat{i})U_i^\dagger(x+\hat{j})U_j^\dagger(x), \quad (2.8)$$

$$U_{tp} = U_t(x)U_i(x+\hat{t})U_t^\dagger(x+\hat{i})U_i^\dagger(x), \quad (2.9)$$

it is possible to define a simple lattice gauge action analogous to Eq. (2.2), which one can verify, as before, possesses the naive correct continuum limit

$$S_G^{SU(3)}[U] = \beta\left(\frac{1}{\xi_g}\Omega_{sp} + \xi_g\Omega_{tp}\right) = \frac{1}{2} \int d^4x \text{Tr} F_{\mu\nu} F_{\mu\nu} + O(a_s^2, a_t^2), \quad (2.10)$$

where  $\xi_g$ , at tree-level, is the anisotropic parameter  $a_s/a_t$  and the  $\Omega$ s are explicitly

given in terms of the plaquettes by,

$$\Omega_{sp} = \sum_{x,i < j} \frac{1}{3} \text{ReTr}(1 - U_{sp}), \quad (2.11)$$

$$\Omega_{tp} = \sum_{x,i} \frac{1}{3} \text{ReTr}(1 - U_{tp}). \quad (2.12)$$

### 2.1.2 Symanzik Improvement

To remove  $O(a^2)$  errors from all Greens functions at tree level in perturbation theory, one needs only to eliminate  $O(a^2)$  artifacts in the lattice action. This can be done by performing a small- $a$  expansion of some suitable lattice action and adjusting the interaction coupling so that the leading terms in the expansion reproduce the correct continuum QCD action and the  $O(a^2)$  terms are absent. Any lattice operator  $\mathcal{O}$ , constructed from the link variables, will have an asymptotic expansion for  $a_s, a_t \rightarrow 0$  of the form

$$\mathcal{O} \approx \sum_k a_s^{k_s} a_t^{k_t} \left( \sum_{\alpha}^{M(k)} r_{\alpha}^{(k)} O_{\alpha}^{(k)} \right), \quad (2.13)$$

where  $r_{\alpha}^{(k)}$  are the expansion coefficients and  $O_{\alpha}^{(k)}$  are local continuum operators of dimension  $k = k_s + k_t$  which are invariant under gauge transformations and all symmetries of the anisotropic lattice. There are no such operators for dimensions less than four and only two dimension four operators,

$$\mathcal{O}_1^{(4)} = g^2 \sum_{ij} \text{Tr} F_{ij} F_{ij} \quad \text{and} \quad \mathcal{O}_2^{(4)} = g^2 \sum_i \text{Tr} F_{it} F_{it}. \quad (2.14)$$

There are no dimension five operators and eighteen independent, dimension six operators, ten of which may be expressed as unimportant total derivatives [12].

For instance, a general improved action can be written as

$$S_G^{SU(N)} = \frac{2N}{g_0^2} \sum_i c_i(g_0^2) \mathcal{O}_i[U], \quad (2.15)$$

where  $\mathcal{O}_i[U]$  are the lattice operators defined by

$$\mathcal{O}_i[U] = \sum_C \frac{1}{N} \text{ReTr}(1 - U_C), \quad (2.16)$$

$U_C$  being the ordered product of link variables around the closed loop  $C$ . Thus, to remove the  $O(a^2)$  errors we adjust the couplings,  $c_i$ , of the  $\mathcal{O}_i[U]$  lattice operators so that the coefficients of the eight dimension six operators vanish and the two coefficients of the two dimension four operators equal each other.

There are several elementary loops that can occur in the improved action of Eq. (2.15). We will follow the choice of C. Morningstar and M. Peardon [13, 14] who adopted an improved action with the spatial and temporal plaquette  $U_{sp}$ ,  $U_{tp}$ , the planar  $2 \times 1$  spatial rectangle  $U_{sr}$  and the short temporal rectangle  $U_{str}$  given respectively by Eq. (2.8), Eq. (2.9) and

$$U_{sr} = U_i(x)U_i(x + \hat{i})U_j(x + 2\hat{i})U_i^\dagger(x + \hat{i} + \hat{j})U_i^\dagger(x + \hat{j})U_j^\dagger(x), \quad (2.17)$$

$$U_{str} = U_i(x)U_i(x + \hat{i})U_t(x + 2\hat{i})U_i^\dagger(x + \hat{i} + \hat{t})U_i^\dagger(x + \hat{t})U_t^\dagger(x). \quad (2.18)$$

We can find the asymptotic expansion of the spatial and temporal rectangles using Stokes theorem. For small lattice spacings the expansion of the spatial rectangles gives

$$\frac{1}{N} \text{ReTr}(1 - U_{sr}) = \frac{g^2}{N} \left[ 2a_s^4 \text{Tr} F_{ij} F_{ij} + \frac{2a_s^6}{3} \text{Tr} F_{ij} D_i^2 F_{ij} + \frac{2a_s^6}{12} \text{Tr} F_{ij} D_j^2 F_{ij} \right], \quad (2.19)$$

and similarly for the temporal rectangles,

$$\frac{1}{N} \text{ReTr}(1 - U_{str}) = \frac{g^2}{N} \left[ 2a_s^2 a_t^2 \text{Tr} F_{it} F_{it} + \frac{2a_s^4 a_t^2}{3} \text{Tr} F_{it} D_i^2 F_{it} + \frac{2a_s^2 a_t^4}{12} \text{Tr} F_{it} D_t^2 F_{it} \right]. \quad (2.20)$$

We can now chose the interaction couplings  $c_i$  in the improved action

$$S_G^{SU(3)} = \frac{1}{\xi_g} c_1 \Omega_{sp} + \xi_g c_2 \Omega_{tp} + \frac{1}{\xi_g} c_3 \Omega_{sr} + \xi_g c_4 \Omega_{str}, \quad (2.21)$$

to eliminate  $O(a_s^2)$  errors. Here  $\Omega_{sp}$  and  $\Omega_{tp}$  are given by Eq. (2.11) and Eq. (2.12) and  $\Omega_{sr}$ ,  $\Omega_{str}$  by

$$\Omega_{sr} = \sum_{x,i \neq j} \frac{1}{3} \text{ReTr}(1 - U_{sr}), \quad (2.22)$$

$$\Omega_{str} = \sum_{x,i} \frac{1}{3} \text{ReTr}(1 - U_{str}). \quad (2.23)$$

Using the asymptotic expansion above, we find that imposing the following three constraints at tree level

$$\frac{1}{4}c_1 + \frac{1}{4}c_2 + 2c_3 + c_4 = \frac{1}{2}, \quad (2.24)$$

$$\frac{1}{24}c_1 + \frac{5}{6}c_3 = 0, \quad (2.25)$$

$$\frac{1}{24}c_2 + \frac{2}{3}c_4 = 0, \quad (2.26)$$

yields a classical lattice gauge action

$$S_G^{SU(3)} = \beta \left\{ \frac{5}{3\xi_g} \Omega_{sp} + \frac{4\xi_g}{3} \Omega_{tp} - \frac{1}{12\xi_g} \Omega_{sr} - \frac{\xi_g}{12} \Omega_{str} \right\}, \quad (2.27)$$

that has  $O(a_t^2, a_s^4)$  discretisation errors.

The  $O(a_t^2)$  error can be removed by the addition of counterterms which next-nearest neighbour time-slices, for instance by adding the tall temporal rectangle in the lattice action [12]. However this introduces spurious high-energy states in the gluon spectrum. To exclude these modes we relax the improvement conditions, requiring that all dimension six operators *except*  $\text{Tr}[(D_t F_{it} F_{it})]$  vanish. The remaining  $O(a_t^2)$  errors are small, being suppressed by a factor of  $\xi^4$ .

### 2.1.3 Tadpole Improvement

The representation of the gauge fields by the exponentiated form

$$U_\mu(x) = e^{iag_0 A_\mu(x)} = 1 + iag_0 A_\mu(x) - \frac{a^2 g_0^2}{2} A_\mu^2(x) + \dots \quad (2.28)$$

rather than directly the vector potential  $A_\mu(x)$  gives rise to local quark-gluon vertices with one, two, ..., gluons. Of these, all but the lowest are lattice artifacts. Contracting the two gluons in  $\frac{a^2 g_0^2}{2} A_\mu^2(x)$  gives rise to tadpole diagrams. These artifacts, though naively suppressed by powers of  $a$ , are in fact only suppressed by powers of  $g_0^2$  due to the ultraviolet divergences generated by the tadpole loops [7, 8]. However, tadpole contributions are generally process independent and so it is possible to measure their contribution in one quantity and then correct for them in all other quantities.

Tadpole improvement starts by assuming that the lattice fields can be split into ultraviolet ( $UV$ ) and infrared ( $IR$ ) parts, and that the  $UV$  part can be integrated out [7, 8],

$$e^{iag_0 A_\mu(x)} = e^{iag_0(A_\mu^{IR}(x) + A_\mu^{UV}(x))} = u_0 e^{iag_0 A_\mu^{IR}(x)} = u_0 \frac{U_\mu(x)}{u_0} \equiv u_0 \tilde{U}_\mu(x). \quad (2.29)$$

The new fields  $\tilde{U}$  are much closer to their continuum values, since the average link field division cancels out most of the tadpole effects. The factors of  $u_0$  in the numerator can be absorbed into couplings and masses. The agreement between perturbation theory and non-perturbative simulations (of short distance quantities) is much better with this rescaling.

In the anisotropic case we have,

$$U_i = u_s \tilde{U}_i(x) \quad \text{and} \quad U_t = u_t \tilde{U}_t(x). \quad (2.30)$$

A common choice for tadpole factors  $u_s$  and  $u_t$  are the fourth root of the plaquettes,  $\langle \frac{1}{3} \text{ReTr} U_{sp} \rangle$  and  $\langle \frac{1}{3} \text{ReTr} U_{tp} \rangle$ , which are computed numerically in a simulation. They are determined by guessing input values for use in the action, measuring the plaquettes and readjusting the input values accordingly. Since, in Landau-gauge perturbation theory,

$$(1 - \langle \frac{1}{3} \text{ReTr} U_{tp} \rangle) \propto (a_t/a_s)^2,$$

when  $a_t$  is significantly smaller than  $a_s$  we can safely set  $u_t = 1$ . Applying tadpole

improvement to our action of Eq. (2.27) we get

$$S_G^{SU(3)} = \beta \left\{ \frac{5}{3\xi_g u_s^4} \Omega_{sp} + \frac{4\xi_g}{3u_s^2 u_t^2} \Omega_{tp} - \frac{1}{12\xi_g u_s^6} \Omega_{sr} - \frac{\xi_g}{12u_s^4 u_t^2} \Omega_{str} \right\}. \quad (2.31)$$

Tadpole improvement is the first step in a systematic procedure for improving the action. The next step is to add in renormalisations due to contributions from the  $k > \pi/a$  physics not already included in the tadpole improvement. However, the coefficients of the correction terms in Eq. (2.31) are only known to leading order in  $\alpha_s$  (so that the action has leading  $O(a_s^4, a_t^2, \alpha_s a_s^2)$  discretisation errors). In principle the coefficients of the correction terms should be computed by “matching” physical quantities computed using perturbation theory on the lattice with the analogous quantities in the continuum. It is, however, clear from the simulations [5, 14, 15] that tree level tadpole, improvement automatically captures most of  $O(\alpha_s)$  corrections.

In [9], C. Morningstar and M. Peardon found that lattice actions and operators constructed out of smeared link variables were much less afflicted by radiative corrections since the usually dominant tadpole contributions were drastically reduced. The smeared link is a combination of the original link and the staples surrounding it,

$$U_\mu^{(1)}(x) = \mathcal{P}_{SU(3)} \left\{ U_\mu^{(0)}(x) + C_\mu^{(0)}(x) \right\}, \quad (2.32)$$

with

$$C_\mu^{(0)}(x) = \sum_{\nu \neq \mu} \rho_{\mu\nu} \left( U_\nu^{(0)}(x) U_\mu^{(0)}(x+\hat{\nu}) U_\nu^{\dagger(0)}(x+\hat{\mu}) + U_\nu^{\dagger(0)}(x-\hat{\nu}) U_\mu^{(0)}(x-\hat{\nu}) U_\nu^{(0)}(x-\hat{\nu}+\hat{\mu}) \right) \quad (2.33)$$

where  $\rho_{\mu\nu}$  is a free parameter and is usually chosen such that  $\rho_{jk} = \rho$  and  $\rho_{4\mu} = \rho_{\mu 4} = 0$ , where only the spatial links are smeared. The smeared link is projected back onto the gauge group by  $\mathcal{P}_{SU(3)}$ . The process can iterated  $n$ -times and one then constructs the action and operators from these smeared links,  $U_\mu^{(n)}$ .

In our calculations when we utilise link smearing we will use the smearing of  $SU(3)$  links proposed by C. Morningstar and M. Peardon [9]. Noting that the matrix

$Q_\mu(x)$  defined by

$$Q_\mu(x) \equiv \frac{i}{2} \left( \Omega_\mu^\dagger(x) - \Omega_\mu(x) \right) - \frac{i}{6} \text{Tr} \left( \Omega_\mu^\dagger(x) - \Omega_\mu(x) \right),$$

where  $\Omega_\mu(x) = C_\mu(x) U_\mu^\dagger(x)$ , (no summation over  $\mu$ ) (2.34)

is Hermitean and traceless, and hence  $e^{iQ_\mu(x)}$  is an element of  $SU(3)$ , they defined an iterative, analytic link smearing algorithm in which the links  $U_\mu^n(x)$  at step  $n$  are mapped into links  $U_\mu^{n+1}(x)$  using

$$U_\mu^{n+1}(x) = e^{iQ_\mu(x)} U_\mu^n(x). \quad (2.35)$$

The action and operators are then constructed using these *stout*, smeared links instead of simple  $U_\mu(x)$ . Operators constructed using link-variable smearing have dramatically reduced mixings with the high frequency modes of the theory.

### 2.1.4 Further Improvement

The lattice theory with a finite cut-off at  $\mu = \pi/a$  can be regarded as an effective theory. The integration over momenta in the range  $\{\pi/a, \infty\}$  renormalises the couplings and generates additional effective interactions. One can therefore regard the lattice theory as a point in an infinite dimensional space of couplings, and taking the continuum limit as a flow in this space to the critical point at  $a = 0$  that defines the physical theory.

It is possible to construct an action from plaquettes in both the fundamental and adjoint representations of  $SU(N)$

$$S = \beta_F \sum \left( 1 - \frac{1}{N} \text{ReTr} U_{\mu\nu} \right) + \beta_A \sum \left( 1 - \frac{1}{N^2} |\text{ReTr} U_{\mu\nu}|^2 \right), \quad (2.36)$$

where the effective bare coupling, obtained using a Taylor expansion, is

$$\beta_{eff} \equiv \frac{2N}{g_{eff}^2} = \beta_F + 2\beta_A. \quad (2.37)$$

This allows simulations in the negative  $\beta_A$  region so long as  $\beta_F > 2|\beta_A|$ . Various authors have revealed a non-trivial phase structure in this space and, in particular, a critical endpoint. C. Morningstar and M. Peardon found that for the lightest scalar glueball state  $0^{++}$ , using the action of Eq. (2.31), the mass was seen to fall rapidly to a minimum when the spatial lattice spacing was  $\sim 0.25fm$ , where the scaling violations are  $\sim 25\%$  and then rise as the lattice spacing is increased further: the so-called “scalar dip” [14]. It has been conjectured that this dip may be related to the presence of the critical endpoint [16, 17].

A current estimate (see Ref. [17]) of the location of this endpoint for  $SU(3)$  gauge theory is  $(\beta_F, \beta_A) = (4.00(7), 2.06(8))$ , that lies well above the  $\beta_F$  axis. This is consistent with the observation that there is no discontinuity in the behaviour of the expectation values of Wilson loops and in the glueball masses, obtained with fundamental loop actions ( $\beta_A = 0$ ). However, U. Heller[17] showed that at the critical endpoint the scalar glueball mass  $m_{0^{++}}$  vanishes and along the line  $\beta_A = 0$ , although there are no singularities, this critical endpoint could cause significant deviations in the scaling for the scalar glueball mass, the “scalar dip”. It is also expected that on a trajectory that lies below the  $\beta_F$  axis (negative  $\beta_A$ ) the influence of the endpoint should be less than along  $\beta_A = 0$ . To test this conjecture C. Morningstar and M. Peardon [11, 18] added adjoint-like terms to the anisotropic action of Eq. (2.31):

$$\Omega_{sp}^{(2t)} = \frac{1}{2} \sum_{x, i < j} \left[ 1 - \frac{1}{N^2} (\text{ReTr} U_{sp}(x)) (\text{ReTr} U_{sp}(x + t)) \right]. \quad (2.38)$$

This term correlates pairs of spatial plaquettes separated by one site temporally. The asymptotic expansion of this term is readily found to be identical to  $\Omega_{sp}$  up to  $O(a_s^4)$ . This implies that the operator combination

$$\tilde{\Omega}_{sp} = (1 + \omega)\Omega_{sp} - \omega\Omega_{sp}^{(2t)}, \quad (2.39)$$

has an identical expansion, in powers of the lattice spacing, to  $\Omega_{sp}$  for all values of  $\omega$  up to  $O(a_s^4)$ . Thus, starting from the improved action in Eq. (2.31) it is straightforward to construct a Symanzik improved, two plaquette action by simply replacing the

spatial plaquette term in Eq. (2.31) with the linear combination  $\tilde{\Omega}_{sp}$ .

In full this action is

$$S_G^{SU(3)} = \beta \left\{ \frac{5(1+\omega)}{3\xi_g u_s^4} \Omega_{sp} + \frac{4\xi_g}{3u_s^2 u_t^2} \Omega_{tp} - \frac{5\omega}{3\xi_g u_s^8} \Omega_{sp}^{(2t)} - \frac{1}{12\xi_g u_s^6} \Omega_{sr} - \frac{\xi_g}{12u_s^4 u_t^2} \Omega_{str} \right\}. \quad (2.40)$$

It has leading  $O(a_s^4, a_t^2, \alpha_s a_s^2)$  discretisation errors and only connects sites on adjacent time-slices, ensuring the free gluon propagator has only one real mode.

## 2.2 Improved Dirac Action

It turns out to be substantially harder to improve lattice fermions than gluons, even at the classical level. The reason, ultimately, is the first order nature of the fermion field equations, which leads to the doubler problem which we discussed in Section 1.2. As we saw, for Dirac fermions (quarks), Wilson solved this problem by adding a second-order derivative term to the action. This term breaks chiral symmetry at  $O(a)$ . Such errors are too large for this action to be useful in coarse lattice simulations.

We shall use the general tool of *field redefinitions* to introduce even-order terms and construct doubler-free quark actions that are classically improved to high order [19]. These shall be applied in the context of an anisotropic formalism to allow the simulation of heavy (as well as light) quark systems.

Since field redefinitions involve one or more free parameters, they lead to so-called redundant couplings whose values can be adjusted at will. This freedom can be used to solve the doubler problem, for example. Our choice of redundant couplings in the class of ‘‘D234’’ actions [19], and the reasons for their choosing, shall be outlined in the derivation of an anisotropic, rotated, improved action, ARIA [20].

### 2.2.1 The Class of D234 Actions

Were it not for the doubler problem, discussed in Section 1.2, *naive* fermions, specified by the fermion operator  $\gamma \cdot \nabla + m$ , which use the usual first order, anti-hermitean,

covariant lattice derivative,

$$\nabla_\mu \psi(x) \equiv \frac{1}{2a_\mu} \left[ U_\mu(x) \psi(x + \hat{\mu}) - U_\mu^\dagger(x - \hat{\mu}) \psi(x - \hat{\mu}) \right] \quad (2.41)$$

would provide a lattice discretisation of Dirac fermions with  $O(a^2)$  errors. Similarly, one could use an improved lattice derivative, such as

$$\nabla_{c\mu} \equiv \nabla_\mu \left( 1 - \frac{1}{6} a_\mu^2 \Delta_\mu \right) = D_\mu + O(a^4), \quad (2.42)$$

where

$$\Delta_\mu \equiv \frac{1}{a_\mu^2} \left[ U_\mu(x) \psi(x + \hat{\mu}) + U_\mu^\dagger(x - \hat{\mu}) \psi(x - \hat{\mu}) - 2\psi(x) \right] \quad (2.43)$$

and the subscript “c” stands for “continuum-like”, to provide a lattice action with  $O(a^4)$  errors - again, if we could ignore doublers.

As well as additional spatial doublers, naive improved fermions have *lattice ghosts*. These are extra unphysical branches in the free dispersion relation that are due to higher order time derivatives in the action. These branches do not describe independent particles; they are just related to the lattice “particle” described by the physical branch of the dispersion relation. Their energies are at the scale of the (temporal) cutoff, so they will eventually decouple as the lattice spacing is decreased.

The doubler problem is true of any fermion matrix of the form

$$\sum_\mu \gamma_\mu \nabla_\mu (1 - b_\mu a_\mu^2 \Delta_\mu + d_\mu a_\mu^4 \Delta_\mu^2 + \dots) \quad (2.44)$$

which preserves chiral symmetry. To avoid doublers we should, following Wilson, introduce chiral symmetry breaking, even-derivative terms  $\Delta_\mu$  (or powers thereof) into the action. However, we would like to avoid the  $O(a)$  errors that a naive addition of a Wilson term entails. This can be achieved by a *field redefinition*.

The simplest way to proceed is to perform the field redefinition in the continuum and only subsequently discretise the action. Starting with the continuum action

$$\int \bar{\psi}_c M_c \psi_c \equiv \int d^4x \bar{\psi}_c(x) (\not{D} + m_c) \psi_c(x) \quad (2.45)$$

we perform a field redefinition

$$\psi_c = \Omega_c \psi \quad (2.46)$$

$$\bar{\psi}_c = \bar{\psi} \bar{\Omega}_c \quad (2.47)$$

$$\bar{\psi}_c M_c \psi_c = \bar{\psi} M_\Omega \psi, \quad M_\Omega \equiv \bar{\Omega}_c M_c \Omega_c. \quad (2.48)$$

Note that the field transformation does not affect spectral quantities, at least if we take into account the Jacobian of the transformation. Classically the Jacobian does not matter. On the quantum level its leading effect is to renormalise the gauge coupling.

Following [19], the canonical choice of field redefinition is (with  $\bar{\Omega}_c$  acting to the right)

$$\bar{\Omega}_c = \Omega_c, \quad \bar{\Omega}_c \Omega_c = 1 - \frac{ra_t}{2} (\not{D} - m_c). \quad (2.49)$$

At this point  $a_t$  is just a constant with the dimension of length, but in the subsequent lattice discretisation  $a_t$  will become the temporal lattice spacing.

The transformed fermion operator  $M_\Omega$  reads

$$\begin{aligned} M_\Omega &= m_c + \not{D} - \frac{1}{2} ra_t (\not{D}^2 - m_c^2) \\ &= m_c \left( 1 + \frac{1}{2} ra_t m_c \right) + \not{D} - \frac{1}{2} ra_t \left( \sum_\mu D_\mu^2 + \frac{1}{2} \sigma \cdot F \right), \end{aligned} \quad (2.50)$$

where the hermitean  $\sigma_{\mu\nu}$  matrices are defined by

$$\sigma_{\mu\nu} = -\frac{1}{2} [\gamma_\mu, \gamma_\nu] = -\sigma_{\nu\mu} \quad (2.51)$$

and we have used

$$\frac{1}{2} \{ \gamma_\mu D_\mu, \gamma_\nu D_\nu \} = \delta_{\mu\nu} D_\mu^2 + \frac{1}{2} \sigma_{\mu\nu} F_{\mu\nu} \quad \text{and} \quad F_{\mu\nu} = i [D_\mu, D_\nu]. \quad (2.52)$$

Using the leading discretisation of the derivatives in Eq. (2.50) gives

$$M_{SW} = m_c(1 + \frac{1}{2}ra_t m_c) + \gamma \cdot \nabla - \frac{1}{2}ra_t \sum_{\mu} \Delta_{\mu} - \frac{1}{4}ra_t \sigma \cdot F, \quad (2.53)$$

which is the Sheikholeslami-Wohlert (SW) action on an anisotropic lattice. If one uses the so-called *clover* representation for  $F_{\mu\nu}$ ,

$$F_{\mu\nu}^{(cl)}(x) \equiv \frac{1}{4a_{\mu}a_{\nu}} \mathcal{T} \left( \begin{aligned} &U_{\mu}(x)U_{\nu}(x + \hat{\mu})U_{\mu}^{\dagger}(x + \hat{\nu})U_{\nu}^{\dagger}(x) + \\ &U_{\nu}(x)U_{\mu}^{\dagger}(x + \hat{\nu} - \hat{\mu})U_{\nu}^{\dagger}(x - \hat{\mu})U_{\mu}(x - \hat{\mu}) + \\ &U_{\mu}^{\dagger}(x - \hat{\mu})U_{\nu}^{\dagger}(x - \hat{\mu} - \hat{\nu})U_{\mu}(x - \hat{\nu})U_{\nu}(x) + \\ &U_{\nu}^{\dagger}(x - \hat{\nu})U_{\mu}(x - \hat{\nu})U_{\nu}(x - \hat{\nu} + \hat{\mu})U_{\mu}^{\dagger}(x) \end{aligned} \right), \quad (2.54)$$

where  $\mathcal{T}(M)$  is the (colour-)traceless imaginary part of an  $N \times N$  matrix,

$$\mathcal{T}(M) \equiv \frac{1}{2}(M - M^{\dagger}) - \frac{i}{N} \text{ImTr} M, \quad (2.55)$$

this action has classical  $O(a^2)$  errors for spectral quantities. This action has no doublers for any  $r > 0$  and no ghost branches either if and only if  $r = 1$ . If the clover term is hand-set to zero this becomes the Wilson action, thereby incurring an  $O(a)$  error.

Going to the next order in the expansion of the continuum derivatives in Eq. (2.50) gives the class of D234 actions,

$$\begin{aligned} M_{D234} = & m_c(1 + \frac{1}{2}ra_t m_c) + \sum_{\mu} \gamma_{\mu} \nabla_{\mu} (1 - b_{\mu} a_{\mu}^2 \Delta_{\mu}) \\ & - \frac{1}{2}ra_t \left( \sum_{\mu} \nabla_{\mu} + \frac{1}{2} \sigma \cdot F \right) + \sum_{\mu} c_{\mu} a_{\mu}^3 \nabla_{\mu}^2. \end{aligned} \quad (2.56)$$

If we use an improved representation of the field strength,

$$F_{\mu\nu}^{(cl)imp} \equiv \frac{5}{3}F_{\mu\nu}^{(cl)}(x) - \frac{1}{6} \left[ U_{\mu}(x)F_{\mu\nu}^{(cl)}(x + \hat{\mu})U_{\mu}^{\dagger}(x) + U_{\mu}^{\dagger}(x - \hat{\mu})F_{\mu\nu}^{(cl)}(x - \hat{\mu})U_{\mu}(x - \hat{\mu}) - (\mu \leftrightarrow \nu) \right] \quad (2.57)$$

this only has  $O(a^4)$  classical errors. The necessary “tuning” of this type of action introduces classical errors in addition to the  $O(a^4)$  ones. However, this is probably irrelevant since the latter errors are unlikely to dominate at the quantum level.

## 2.2.2 D234 Actions on Anisotropic Lattices

To simulate a bottom quark with a relativistic action requires a lattice spacing of less than 0.04fm, which is prohibitively expensive on an isotropic lattice where the simulation cost scales at least as  $O(1/a^4)$ . The anisotropic lattice offers the possibility of relativistic heavy-quark physics using reasonably modest computational resources.

The signal to noise ratio of a correlation function calculated in a Monte Carlo simulation decays exponentially in time. Choosing a smaller  $a_t$  gives more time-slices with an accurate signal, allowing for more precise and confident mass determinations. This is important for particles with bad signal/noise properties, like P-state mesons [44] and, as we have seen, the glueball spectrum [13]. Improved precision in effective mass fits (see Section 3.1) means that momentum-dependent errors of  $O(ap)$  can be disentangled from other discretisation effects and larger particle momenta may be considered.

However, because they have lost part of their axis permutation symmetry, anisotropic actions have more independent coefficients. This is not a problem at the classical level, but at the quantum level some of these coefficients will have to be tuned to restore space-time exchange symmetry.

For an anisotropic lattice, deriving a D234 class action is slightly more complicated. The allowed operators at  $O(a)$  consist of the spatial and temporal parts of the Wilson and clover terms, see Eq. (2.53), and the additional operator  $[\gamma_t D_t, \sum_i \gamma_i D_i]$ .

The most general field transformations in this situation lead to three redundant operators, so that one has to tune two coefficients at  $O(a)$ . These can be chosen to be spatial and temporal parts of the clover term. On an anisotropic lattice one must also allow a relative coefficient between the temporal and spatial kinetic terms at  $O(a)$ , which can be tuned non-perturbatively, e.g., to demand a relativistic dispersion relation for the pion.

The D234 action on the anisotropic lattice is given by [19, 21]

$$M_{D234}^{Anis} = m_0 + \sum_{\mu} \nu_{\mu} \gamma_{\mu} \nabla_{\mu} (1 - b_{\mu} a_{\mu}^2 \Delta_{\mu}) - \frac{1}{2} a_t \left( \sum_{\mu} r_{\mu} \Delta_{\mu} + \sum_{\mu < \nu} c_{SW}^{\mu} \sigma_{\mu\nu} F_{\mu\nu} \right) + \sum_{\mu} \nu_{\mu} d_{\mu} a_{\mu}^3 \Delta_{\mu}^2 \quad (2.58)$$

where  $a_0 = a_t$  and  $a_i = a_s$  are the temporal and spatial lattice spacings respectively.

### 2.2.3 ARIA

From the rotation of Eq. (2.49), for a fixed Wilson parameter  $r$ , we see that one will recover spatial doublers in the anisotropic case as  $a_t$  is made small, since  $\Omega_c \rightarrow 1$  as  $a_t \rightarrow 0$  [22]. This hinders simulations where  $a_t \ll a_s$ . To construct an action suitable for high anisotropies we begin by applying field rotations in the temporal direction only,

$$\bar{\Omega}_c = \Omega_c, \quad \bar{\Omega}_c \Omega_c = 1 - \frac{r a_t}{2} (\gamma_0 D_0 - m_c). \quad (2.59)$$

This amounts to the parameters  $\nu$ ,  $c_{SW}$  and  $r$  in Eq. (2.58) having the following values

$$\begin{aligned} (\nu_0, \nu_i) &= (1, \mu_r), \\ (c_{SW}^0, c_{SW}^i) &= (0, \frac{1}{2}), \\ (r_0, r_i) &= (r, 0) \end{aligned} \quad (2.60)$$

and  $\mu_r = 1 + \frac{1}{2} r_i a_t m_0$ .

Temporal derivatives usually cause problems when improving the discretisation

of an action. This is because successive improvements to the temporal derivatives involve operators that are increasingly non-local in time and, therefore, almost inevitably result in lattice ghosts of one sort or another. We retain the one-hop improvement of the rotation but remove the improved temporal discretisation that causes ghosts,

$$(b_0, b_i) = (0, \frac{1}{6}) \quad \text{and} \quad (d_0, d_i) = (0, s) \quad (2.61)$$

The lack of a spatial rotation potentially means that we retain spatial doublers. The removal of these doublers is assured by the choice of parameters  $b_i = \frac{1}{6}$  and  $d_i = s$ . The choice of  $b_i$  results in an improved spatial discretisation with a leading error of  $O(a_s^4)$ , the doublers are removed by the Wilson-like parameter  $s$  which introduces a leading spatial error of  $O(a_s^3)$ .

At the tree-level, the rotations of Eq. (2.59) do not generate a spatial clover term. Since we have removed the improved temporal discretisation, the temporal clover term (the chromoelectric field) does not need an improved representation and is discretised by a clover term with plaquettes in the three space-time planes only

$$gF_{i0} = \frac{1}{\xi a_t^2} \frac{1}{u_s^2 u_t^2} \frac{1}{8i} \left\{ \Omega_i(x) - \Omega_i^\dagger(x) \right\}, \quad (2.62)$$

with

$$\begin{aligned} \Omega_i(x) = & U_i(x) U_t(x + \hat{i}) U_i^\dagger(x + \hat{t}) U_t^\dagger(x) \\ & + U_t(x) U_i^\dagger(x - \hat{i} + \hat{t}) U_t^\dagger(x - \hat{i}) U_i(x - \hat{i}) \\ & + U_i^\dagger(x - \hat{i}) U_t^\dagger(x - \hat{i} - \hat{t}) U_i(x - \hat{i} - \hat{t}) U_t(x - \hat{t}) \\ & + U_t^\dagger(x - \hat{t}) U_i(x - \hat{t}) U_t(x + \hat{i} - \hat{t}) U_i^\dagger(x). \end{aligned} \quad (2.63)$$

where  $E_i = F_{i0}$ ,  $u_s$  and  $u_t$  are the tadpole improvement parameters and  $\xi_q = a_s/a_t$  is the anisotropy.  $u_s$  is determined from the spatial plaquette and  $u_t$  is set to unity.

Including the gauge fields and tadpole improvement factors, the lattice fermion

matrix is given by [20],

$$\begin{aligned}
M_{\text{ARIA}}\psi(x) = & \frac{1}{a_t} \left\{ \left( \mu_r m a_t + \frac{18s}{\xi_q} + r + \frac{r a_t^2 g}{4} \sigma_{i0} F_{i0} \right) \psi(x) \right. \\
& - \frac{1}{2u_t} [(r - \gamma_0) U_t(x) \psi(x + \hat{t}) + (r + \gamma_0) U_t^\dagger(x - \hat{t}) \psi(x - \hat{t})] \\
& - \frac{1}{\xi_q} \sum_i \left[ \frac{1}{u_s} (4s - \frac{2}{3} \mu_r \gamma_i) U_i(x) \psi(x + \hat{i}) + \frac{1}{u_s} (4s + \frac{2}{3} \mu_r \gamma_i) U_i^\dagger(x - \hat{i}) \psi(x - \hat{i}) \right. \\
& - \frac{1}{u_s^2} (s - \frac{1}{12} \mu_r \gamma_i) U_i(x) U_i(x + \hat{i}) \psi(x + 2\hat{i}) \\
& \left. \left. - \frac{1}{u_s^2} (s + \frac{1}{12} \mu_r \gamma_i) U_i^\dagger(x - \hat{i}) U_i^\dagger(x - 2\hat{i}) \psi(x - 2\hat{i}) \right] \right\}. \tag{2.64}
\end{aligned}$$

At the tree-level, the fermion anisotropy  $\xi_q$  is given by the ratio of scales,  $\xi = a_s/a_t$ . We call the action described here ARIA for Anisotropic, Rotated, Improved Action. It has leading errors of  $O(a_t^2, a_s^3)$ .

#### 2.2.4 Analytic results for ARIA

We now calculate the energy-momentum behaviour of the ARIA action. The free-quark dispersion relation is obtained by solving  $\det \widetilde{M}_{\text{ARIA}} = 0$  in momentum space where  $\widetilde{M}_{\text{ARIA}}$  is the Fourier transform of  $M_{\text{ARIA}}$  in Eq. (2.64). The energy-momentum relation is, for general  $r$  and  $s$ ,

$$\begin{aligned}
\cosh(E a_t) = & \frac{r^2 + r\omega(p)}{r^2 - 1} \pm \\
& \frac{\sqrt{(r + \omega(p))^2 + (1 - r^2)(1 + a_t^2 \tilde{\mathbf{p}}^2)}}{r^2 - 1}, \tag{2.65}
\end{aligned}$$

where  $\omega(p)$  and  $\tilde{\mathbf{p}}$  are defined as

$$\omega(p) = a_t \mu_r m_0 + a_t s \sum_i a_s^3 \hat{p}_i^4, \tag{2.66}$$

$$\tilde{\mathbf{p}} = \mu_r \bar{p}_i (1 + \frac{1}{6} a_s^2 \hat{p}_i^2), \tag{2.67}$$

with  $\bar{p}_i = \frac{1}{a_s} \sin(a_s p_i)$  and  $\hat{p}_i = \frac{2}{a_s} \sin(a_s p_i/2)$  [20]. Expanding the physical solution in powers of spatial momentum yields

$$E^2(\mathbf{p}) = M_1^2 + \frac{M_1}{M_2} \mathbf{p}^2 + O(\mathbf{p}^4), \quad (2.68)$$

where  $M_1$  is the rest mass, given by

$$M_1 = \frac{1}{a_t} \cosh^{-1} \left( \frac{r^2 + \mu_r m_0 r a_t - \sqrt{1 + 2\mu_r m_0 r a_t + m_0^2 \mu_r^2 a_t^2}}{r^2 - 1} \right). \quad (2.69)$$

The kinetic mass,  $M_2$  is given by

$$\frac{1}{M_2} = \frac{\mu_r^2 a_t}{\sqrt{1 + 2\mu_r m_0 r a_t + m_0^2 \mu_r^2 a_t^2}} \left[ \left( \frac{r^2 + \mu_r m_0 r a_t - \sqrt{1 + 2\mu_r m_0 r a_t + m_0^2 \mu_r^2 a_t^2}}{r^2 - 1} \right)^2 - 1 \right]^{-\frac{1}{2}}. \quad (2.70)$$

Eq. (2.69) and Eq. (2.70) indicate that at the tree-level  $M_1$  and  $M_2$  do not depend on  $O(a_s m_q)$  terms or on the ratio of scales,  $\xi$ .

To compare these expressions with the results of other studies, the particular choice  $r = 1$  was considered. In this case the lattice ghost (the unphysical solution of Eq. (2.65)) disappears and the dispersion relation is given by

$$4 \sinh^2 \left( \frac{E a_t}{2} \right) = \frac{a_t^2 \tilde{\mathbf{p}}^2 + \omega^2(p)}{1 + \omega(p)}, \quad (2.71)$$

with

$$M_1 = \frac{1}{a_t} \log(1 + \mu_r m_0 a_t), \quad (2.72)$$

$$\frac{1}{2M_2} = \frac{\mu_r}{m_0(2 + \mu_r m_0 a_t)}. \quad (2.73)$$

where now  $\mu_r = (1 + \frac{1}{2} a_t m_0)$ . These expressions are consistent with those obtained in Ref. [21] for the sD34 action and in Ref. [23] for the Fermilab action on an isotropic lattice.

The free-quark dispersion relations for massless and massive quarks are shown in

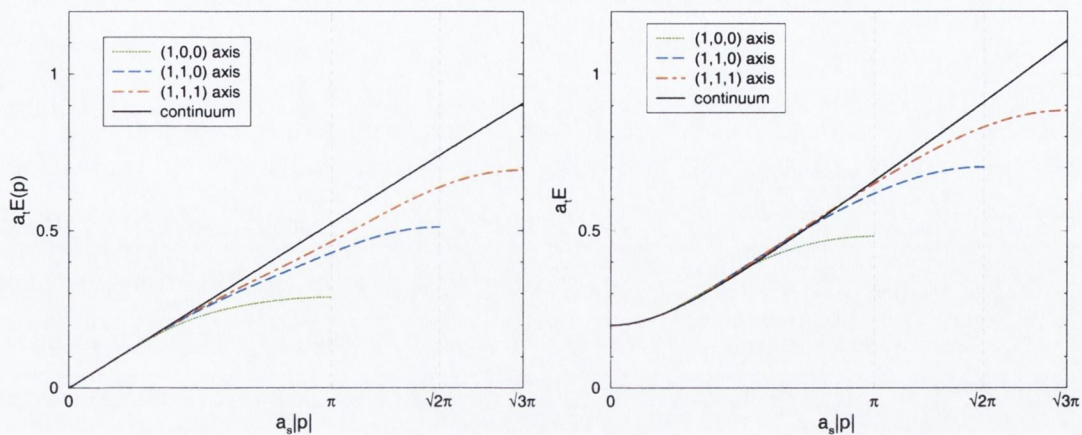


Figure 2-1: The dispersion relations given by Eq. 2.65 with  $\xi = 6$ ,  $r = 1$  and  $s = 1/8$ . The plot on the left is the massless case while the plot on the right shows the massive case, with  $a_t m_q = 0.2$ .

Fig. (2-1). The anisotropy parameter,  $\xi$  is six for both cases.

In analogy to the traditional Wilson  $r$ -parameter, the parameter  $s$  in this action can in principle take any positive value. We chose  $s = 1/8$ , demanding that the energy-momentum relations do not have negative slope for  $a_s |p| < \pi$ .

## 2.3 Tuning

Counting relevant dimension-4 operators with the appropriate symmetries implies both the gauge and fermion action have one free parameter, the “bare” anisotropies for these fields,  $\xi_g$  and  $\xi_q$ , defined in the gluon and quark actions of Eq. (2.40) and Eq. (2.64). They give the desired anisotropy at tree-level in perturbation theory. Quantum fluctuations renormalise these parameters however, so that the input parameters  $\xi_g$  and  $\xi_q$  in the gluon and quark actions are not the same as the anisotropy determined from a physical observable in a simulation. To ensure the low-momentum dispersion relations for both the quark and gluon degrees of freedom accurately reproduce their continuum forms,  $\xi_g$  and  $\xi_q$  should be determined non-perturbatively to give a single, target anisotropy.

For a simulation of either the pure gauge sector or the *quenched* approximation of the theory, we can tune the two parameters independently. It suffices to run simulations with an arbitrary anisotropic gauge action, and then make a non-perturbative measurement of the ratio of the scales by, e.g., comparing the potential between static colour sources separated along coarse and fine directions (the *sideways* potential). With the absence of vacuum polarisation effects, a similar method can then be adopted post hoc for the quark action, where the dispersion relation of the pion at low momentum, which should be relativistic, is used to tune  $\xi_q$  to also give the target anisotropy.

In dynamical simulations, this is no longer possible. An arbitrary anisotropic action could lead to quarks and gluons with different low-momentum dispersion relations, due to the presence of the fermion contribution to the path integral. The parameters in the action for a dynamical simulation must be tuned simultaneously so that the quarks and gluons have a common renormalised anisotropy,  $\xi$ . We employ a non-perturbative method to ensure this.

### 2.3.1 Tuning the Anisotropies in a Quenched Simulation

The quenched approximation of QCD (QQCD) consists of ignoring fermion contributions to the path integral, i.e., setting  $\det M = \text{constant}$  in Eq. (1.24). The sole

reason for this approximation is the computational expense of including the highly non-local determinant term in the generation of the background gauge configurations. However, since QCD is confining, asymptotically free, and shows spontaneous chiral symmetry breaking, and differs from full QCD only in the relative weighting of the background gauge configurations, the physics analyses are identical in most cases. It is, therefore, usually considered reasonable to do detailed quenched simulations to understand sources of errors before committing the additional computer resources required for a full QCD simulation.

Physically, the quenched approximation corresponds to turning off vacuum polarisation effects of quark loops. One important consequence of this is the effect on the potential between a  $q\bar{q}$  pair as a function of the separation. In the full theory the string breaks by the creation of a  $q\bar{q}$  pair out of the vacuum, therefore at large distances there is a screened potential between two mesons. In QCD the string does not break, and so the long distance behaviour of the two theories is very different and one might be led to believe that QCD is a bad approximation. However, because of confinement, the long distance scale that is relevant to hadronic physics has a natural cut-off of a few fermi.

With the absence of the fermion contribution to the path integral in QCD, it is possible to tune the anisotropies  $\xi_g$  and  $\xi_q$  independently such that the renormalised anisotropy in both cases equals the target anisotropy,  $\xi$ . For the gauge action, the renormalisation of the anisotropy  $\xi_g$  can be determined by measuring the static-quark potential  $V(x, y, z)$  from Wilson loops in different orientations. The potential between two static sources propagating along the  $z$ -axis, the *sideways* potential [24], separated along coarse and fine axes are measured by

$$V_s(\vec{x}, z) = \log \frac{W_{ss}(\vec{x}, z)}{W_{ss}(\vec{x}, z+1)} \quad \text{and} \quad V_t(t, z) = \log \frac{W_{ts}(t, z)}{W_{ts}(t, z+1)}, \quad (2.74)$$

where  $W_{ss}$  is a spatial-spatial rectangular Wilson loop and  $W_{ts}$  is a temporal-spatial rectangular Wilson loop. As  $z \rightarrow \infty$ ,  $V_s(\vec{x}, z) \rightarrow V_s(|\vec{x}|)$  and  $V_t(t, z) \rightarrow V_t(t)$ , where  $V_s(|\vec{x}|)$  and  $V_t(t)$  are the two versions of the interquark potential. The demand that the two measurements yield the same function of *physical* distance determines the

renormalised anisotropy. For a physical distance  $r$  we have  $|\vec{x}| = t = r$ , we can set  $|\vec{x}| = na_s$  and  $t = nma_t$  and tune  $\xi_g$  such that the ratio

$$\rho_n = \frac{V_s(na_s)}{V_t(mna_t)} \equiv 1 \quad (2.75)$$

and the renormalised anisotropy is, therefore, given by  $m$ .

Using background gauge configurations with a tuned anisotropy  $\xi_g$ , the parameter  $\xi_q$  in the quark action is tuned such that the value of the anisotropy determined from an energy momentum dispersion relation is equal to the required renormalised anisotropy  $\xi$ .

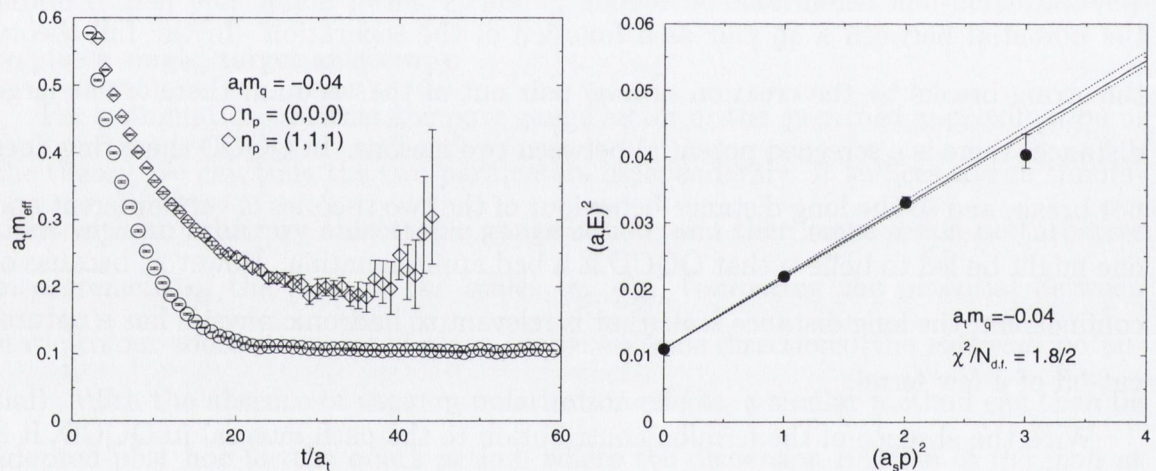


Figure 2-2: The plot on the left is a pseudoscalar meson effective mass plots of the lightest meson made from a degenerate combination of quarks with  $a_t m_q = -0.04$  for zero momentum and also for three units of momentum in lattice units. The second plot is the energy-momentum relation for this meson.

Increased resolution in the temporal direction on anisotropic lattices allows the determination of heavy mass quantities whose signal to noise ratio decreases rapidly. This allows us to accurately simulate a wide range of quark masses and, notably, a wide range of momenta. Particles such as the  $\pi$  and  $\rho$  mesons are good candidates for a determination of the anisotropy from a dispersion relation because of their high signal to noise ratio. If we determine the effective masses (see Section 3.1) of a particle,  $a_t E$  in lattice units, for a range of spatial momenta,  $a_s p$  in lattice units, we can plot the dispersion relation,  $(a_t E)^2$  versus  $(a_s p)^2$ . An example of a typical

effective mass plot and dispersion relation can be seen in Fig. (2-2). For a relativistic particle, the renormalised anisotropy is related to the slope of this plot,  $m$ , by

$$\xi^2 = \frac{c^2}{m} = \frac{1}{m} \quad \text{where} \quad c \equiv 1. \quad (2.76)$$

We tune  $\xi_q$  such that this relation gives the required renormalised anisotropy  $\xi$ .

The anisotropic action of Eq. (2.64) offers the possibility of precision studies of a range of phenomenologically interesting heavy quark quantities in the  $D$ ,  $B$ ,  $J/\psi$  and  $\Upsilon$  sectors. For this reason it is important to understand the dependence of  $\xi_q$  on the heavy quark mass used in simulations. In particular, a contribution of  $O(a_s m_q)$  to the renormalised anisotropy would spoil this tuning for charm and bottom quark masses.

In [20], we tuned the anisotropy  $\xi_q$  to give a renormalised anisotropy of  $\xi = 6$  for a pion at a bare quark mass of  $m_q = -0.04$ . Using the relation of Eq. (2.76), we then studied the mass-dependence of the speed of light at this fixed anisotropy. We used a simplified version of Eq. (2.64) in this exploratory study, where the clover term was set to zero and  $\mu_r$  was set to 1. This results in a leading  $O(a_t)$  classical discretisation error. However, since  $a_t$  is small in these simulations,  $a_t \sim 0.04$  fm, the effects should be under control at least when  $a_t m_q < 1$ . Details of the simulation and parameter values are summarised in in Table 2.1. A broad range of quark masses was investigated,

# gauge configurations	100
Volume	$10^3 \times 120$
$a_s$	0.21fm
$a_s/r_0$	0.4332(11)
$\xi = a_s/a_t$	6
$a_t m_q$	-0.04,0.1,0.2,0.3,0.4,0.5,1.0,1.5

Table 2.1: Details of the quenched simulation.

from  $a_t m_q = -0.04$  which is close to the strange quark on these lattices to heavy quarks with  $a_t m_q = 1.0$  and 1.5. Both degenerate and non-degenerate combinations are considered. The non-degenerate combination is made with the lightest quark and each of the heavier quarks. Note that  $a_t m_q = -0.04$  corresponds to a positive quark

mass since Wilson-type actions have an additive, as well as a multiplicative, mass renormalisation. We accumulated data at spatial momenta  $(0,0,0)$ ,  $(1,0,0)$ ,  $(1,1,0)$  and  $(1,1,1)$ , in units of  $2\pi/a_s L$ , averaging over equivalent momenta.

In Tables 2.2 and 2.3 we show the speed of light determined from the slope of the dispersion relation for each mass in the simulation. Results for both pseudoscalar and vector mesons are given. The tables indicate a stronger mass-dependence for mesons made with degenerate combinations of quarks (corresponding to heavy-heavy particles) compared with the non-degenerate (heavy-light) particles.

$a_t m_q$	Pseudoscalar			Vector		
	$a_t M_{PS}$	$c$	$\chi^2/N_{df}$	$a_t M_V$	$c$	$\chi^2/N_{df}$
-0.04	$0.1045^{+5}_{-5}$	$1.02^{+1}_{-1}$	6.3/2	$0.161^{+2}_{-2}$	$0.97^{+2}_{-2}$	0.66/2
0.10	$0.3831^{+4}_{-4}$	$0.983^{+6}_{-7}$	2.8/2	$0.3934^{+4}_{-4}$	$0.982^{+8}_{-8}$	2.1/2
0.20	$0.5418^{+3}_{-4}$	$0.995^{+7}_{-7}$	0.33/2	$0.5472^{+4}_{-4}$	$0.990^{+8}_{-8}$	2.1/2
0.30	$0.6887^{+4}_{-4}$	$1.010^{+8}_{-7}$	2.4/2	$0.6924^{+4}_{-4}$	$0.997^{+9}_{-9}$	4.5/2
0.40	$0.8269^{+4}_{-4}$	$1.022^{+5}_{-5}$	0.65/2	$0.8294^{+4}_{-4}$	$1.011^{+5}_{-5}$	2.3/2
0.50	$0.9569^{+4}_{-4}$	$1.035^{+5}_{-5}$	1.3/2	$0.9587^{+4}_{-4}$	$1.025^{+5}_{-5}$	1.6/2
1.00	$1.5086^{+3}_{-3}$	$1.069^{+5}_{-5}$	1.3/2	$1.5092^{+3}_{-3}$	$1.072^{+5}_{-5}$	1.2/2
1.50	$1.9428^{+3}_{-3}$	$1.075^{+5}_{-5}$	0.081/2	$1.9431^{+3}_{-4}$	$1.072^{+5}_{-5}$	0.058/2

Table 2.2: The ground state pseudoscalar and vector masses with degenerate quarks. The speed of light determined from the dispersion relation for each quark mass is shown with the associated  $\chi^2/N_{d.f.}$ . The errors in all cases are statistical only. The parameter,  $\xi_q$  is fixed in these simulations to 6.17, its value determined from the dispersion relation of the lightest degenerate pseudoscalar meson.

From Table 2.2 the data show an  $\sim 9\%$  shift in the value of  $c$  as the quark mass is changed from  $m_q = m_s$  (at  $a_t m_q \approx -0.04$  on these lattices) to  $m_q > m_b$  (at  $a_t m_q \approx 0.8$ ). For a more modest range of quark masses,  $m_q = m_s$  to  $m_q \sim m_c$  (at  $a_t m_q \approx 0.2$ ) the variation in  $c$  is only 3%. The conclusion is that a single anisotropy renormalisation at  $m_q = m_s$  is sufficient to reliably simulate physics from light hadrons to charmonium. If bottomonium physics is of interest then the renormalisation should be carried out at a heavier quark mass.

Table 2.3 shows that in the heavy-light case the variation in  $c$  is very small - approximately 4% over the range of quark masses considered. This is further reduced to  $\sim 2\%$  if only quark masses,  $m_s \leq m_q \leq m_c$  are considered.

$a_t m_q$	Pseudoscalar			Vector		
	$a_t M_{PS}$	$c$	$\chi^2/N_{df}$	$a_t M_V$	$c$	$\chi^2/N_{df}$
0.1	$0.2610^{+6}_{-6}$	$0.98^{+1}_{-1}$	0.23/2	$0.2802^{+8}_{-8}$	$0.98^{+2}_{-2}$	0.19/2
0.2	$0.3466^{+6}_{-6}$	$1.01^{+2}_{-2}$	0.56/2	$0.3601^{+8}_{-8}$	$0.99^{+2}_{-2}$	0.64/2
0.3	$0.4254^{+7}_{-7}$	$1.02^{+2}_{-2}$	2/2	$0.4351^{+8}_{-8}$	$1.00^{+2}_{-2}$	0.45/2
0.4	$0.4987^{+7}_{-7}$	$1.01^{+2}_{-2}$	1.5/2	$0.5056^{+8}_{-9}$	$0.99^{+2}_{-2}$	1.4/2
0.5	$0.5668^{+8}_{-8}$	$1.02^{+2}_{-2}$	1.7/2	$0.5720^{+9}_{-9}$	$1.00^{+2}_{-2}$	1.6/2
1.0	$0.8521^{+10}_{-10}$	$1.00^{+2}_{-2}$	2.6/2	$0.854^{+1}_{-1}$	$1.02^{+3}_{-3}$	0.62/2
1.5	$1.074^{+1}_{-1}$	$1.02^{+3}_{-3}$	2.1/2	$1.075^{+1}_{-1}$	$1.01^{+3}_{-4}$	1.8/2

Table 2.3: The ground state masses of non-degenerate combinations of quark masses. In each case the quark mass given is combined with the lightest mass in our simulations,  $a_t m_q = -0.04$ . As in Table 2.2 the pseudoscalar and vector meson states are shown with the speed of light and the associated  $\chi^2/N_{d.f.}$ . Once again all errors are statistical only and  $\xi_q = 6.17$ .

### 2.3.2 Tuning the Anisotropy in a Dynamical Simulation

In a full QCD simulation the presence of the fermion determinant in the gauge action forces us to simultaneously tune both the gauge and fermion anisotropies. Finding the correctly tuned lattice action with a given anisotropy corresponds to finding a point in a two dimensional plane. This point, denoted  $(\xi'_g, \xi'_q)$ , is found by demanding two conditions are satisfied which ensure the low-energy physics of both the quark and gluon are on a lattice with the appropriate length scale. In principle, all low-energy observations should agree, up to a discrepancy at the order of the leading discretisation errors for the action which are  $O(\alpha_s a_s)$ . The two conditions we apply are the agreement of the sideways potential of Eq. (2.74) along the spatial and temporal axes and, secondly, that the low-momentum pion dispersion relation is relativistic.

In order to find this point  $(\xi'_g, \xi'_q)$ , at least three simulations close to the point are required. If we assume a linear behaviour near the matching point, these three points define a plane. We can then use a flat planar function to interpolate to the point  $(\xi'_g, \xi'_q)$ . Each of the two matching conditions individually define a line in this plane,  $(\xi'_g, \xi'_q)$  is the intersection of these two lines [54].

### 2.3.3 Other parameters

The free parameter  $\omega$  in the gauge action of Eq. (2.40) must be chosen greater than zero to ensure the approach to the QCD continuum is made far away from the critical endpoint in the plane of fundamental-adjoint couplings. Also, the physical quantities should be independent of it. It has been confirmed in Ref. [13] that once the input is set beyond  $\omega = 1$  there is little dependence of physical mass ratios on the precise value of the parameter and thus no fine tuning is required to reproduce continuum results.

The temporal Wilson parameter  $r$  in Eq. (2.64) is chosen to be one to ensure the energy-momentum relation for the fermion has a physical solution only, and the temporal doublers do not appear [19]. The Wilson-like parameter  $s$  is chosen to be  $1/8$  so that the spatial doublers receive a sufficiently large mass. Since  $s$  parameterises a term which removes the spatial doublers and is irrelevant in the continuum limit precise tuning is not required.

# Chapter 3

## Propagators

In QCD results for physical observables are obtained by calculating expectation values,

$$\langle \mathcal{O} \rangle = \frac{1}{Z} \int \mathcal{D}A_\mu \mathcal{O} e^{-\tilde{S}} \quad (3.1)$$

where  $Z$  is the partition function,

$$Z = \int \mathcal{D}A_\mu e^{-\tilde{S}}, \quad (3.2)$$

$\tilde{S}$  is the effective QCD action

$$\tilde{S}[U] = S_G[U] + \log(\det M), \quad (3.3)$$

$M$  is the Dirac operator and  $\mathcal{O}$  is any given combination of operators expressed in terms of time-ordered products of gauge and quark fields.

Expectation values in the path integral approach correspond to time-ordered correlation functions. The quark fields in  $\mathcal{O}$  are, in practice, re-expressed in terms of quark propagators using Wick's theorem for contracting fields. In this way all dependence on quarks as dynamical fields is removed. I will illustrate this below in a sample case for a two-point correlation function. The basic building block for fermionic quantities is, therefore, the Feynman (or quark) propagator,

$$S_F(y, j, b; x, i, a) = (M^{-1})_{x,i,a}^{y,j,b} \quad (3.4)$$

where  $M^{-1}$  is the inverse of the Dirac operator calculated on a given background field. A given element of this matrix  $(M^{-1})_{x,i,a}^{y,j,b}$  is the amplitude for propagation of a quark from site  $x$  with spin-colour  $i, a$  to site-spin-colour  $y, j, b$ .

### 3.1 Point-to-All Propagators

Let us consider the general 2-point correlation function,

$$C^{BA}(\mathbf{p}, t) = \langle 0 | T \sum_{\mathbf{x}} e^{-ip \cdot x} \mathcal{O}^B(\mathbf{x}, t) \mathcal{O}^A(\mathbf{0}, 0) | 0 \rangle \quad (3.5)$$

with  $t > 0$ . The operators  $\mathcal{O}$  are chosen so that they have a large coupling to the meson of interest. This 2-point correlation function gives the amplitude for creating a state with the quantum numbers of the particular meson out of the vacuum at space-time point 0 by the “source” operator  $\mathcal{O}^A$ ; the evolution of the state via the QCD Hamiltonian and finally the annihilation by the “sink” operator  $\mathcal{O}^B$ .

The rules of quantum mechanics tells us that  $\mathcal{O}^A$  will create a state that is a linear combination of all possible eigenstates of the Hamiltonian that have the same quantum numbers as the required meson. The second rule is that on propagating for Euclidean time  $t$ , a given eigenstate with energy  $E$  picks up a weight  $e^{-E_n t}$ . This is because the operators  $\mathcal{O}$  evolve according to  $\mathcal{O}(\mathbf{x}, t) = e^{Ht} \mathcal{O}(\mathbf{x}, 0) e^{-Ht}$  where  $H$  is the Hamiltonian of the system and the insertion of a complete set of eigenstates in Eq. (3.5) will give us these weights. Thus, the 2-point function can be written in terms of a sum over all possible intermediate states

$$\langle 0 | \sum_{\mathbf{x}} e^{-ip \cdot x} \mathcal{O}^B(\mathbf{x}, t) \mathcal{O}^A(\mathbf{0}, 0) | 0 \rangle = \sum_n \frac{\langle 0 | \mathcal{O}^B | n \rangle \langle n | \mathcal{O}^A | 0 \rangle}{2E_n} e^{-E_n t} \quad (3.6)$$

To study the meson at momentum  $\mathbf{p}$  we need to isolate this state from the sum over  $n$ . This first simplification is done through the Fourier projection  $\sum_x e^{-ip \cdot x}$  as it restricts the sum over states to just  $\mathbf{p}$ -momentum states. The second step is to isolate the required meson. This is done through judicious choice of the operators  $\mathcal{O}$  to limit the sum over states, and, secondly, through examining the large  $t$  behaviour

of the 2-point functions where only the contribution of the lowest energy state that couples to  $\mathcal{O}^A$  is significant due to exponential damping,

$$\langle 0 | \sum_{\mathbf{x}} e^{-ip \cdot \mathbf{x}} \mathcal{O}^B(\mathbf{x}, t) \mathcal{O}^A(\mathbf{0}, 0) | 0 \rangle \stackrel{t \rightarrow \infty}{=} \frac{\langle 0 | \mathcal{O}^B | E_0 \rangle \langle E_0 | \mathcal{O}^A | 0 \rangle}{2E_0} e^{-E_0 t}. \quad (3.7)$$

We can extract the energy from the rate of exponential fall off in time.

A straight-forward method of doing this is to take the ratio  $C^{BA}(t)/C^{BA}(t+1)$  and plot the log of this as a function of  $t$ , this is usually called an effective mass plot.

We can see that

$$\log \frac{C^{BA}(\mathbf{p}, t)}{C^{BA}(\mathbf{p}, t+1)} \stackrel{t \rightarrow \infty}{=} E_0, \quad (3.8)$$

so fitting a straight line to the large  $t$  behaviour of an effective mass plot yields the energy of the required state in lattice units. Although effective mass plots are useful to discern a plateau region, in practice the fits are still performed directly to the correlation function. We note also that, for mesons, an identical state propagates backwards and forwards in time, so in practice the fit is performed to  $e^{-E_0 t} + e^{-E_0(T-t)}$ , where the lattice has  $T$  time slices.

The operators  $\mathcal{O}$  take the general form

$$\mathcal{O}^A = \bar{\psi}_1 \Gamma^A \psi_2 \quad \text{and} \quad \mathcal{O}^B = \bar{\psi}_2 \Gamma^B \psi_1 \quad (3.9)$$

for non-degenerate quarks. We can now express Eq. (3.5) in terms of the basic quantities we control in the path integral - the gauge fields and the quark propagator. Using Wick contractions, the correlation function can be written in terms of a product of two quark propagators  $S_F$ ,

$$\begin{aligned} C^{BA}(\mathbf{p}, t) &= \sum_{\mathbf{x}} e^{-ip \cdot \mathbf{x}} \langle 0 | \bar{\psi}_2(\mathbf{x}, t) \Gamma^B \psi_1(\mathbf{x}, t) \bar{\psi}_1(\mathbf{0}, 0) \Gamma^A \psi_2(\mathbf{0}, 0) | 0 \rangle \\ &= - \sum_{\mathbf{x}} e^{-ip \cdot \mathbf{x}} \langle \text{Tr}(S_{F_2}(0; \mathbf{x}, t) \Gamma^B S_{F_1}(\mathbf{x}, t; 0) \Gamma^A) \rangle \end{aligned} \quad (3.10)$$

where the trace is over spin and colour indices. An illustration of this correlation can be seen in Fig. (3-1). Using the hermiticity property  $S_F(0; \mathbf{x}, t) = \gamma_5 S_F(\mathbf{x}, t; 0)^\dagger \gamma_5$ ,

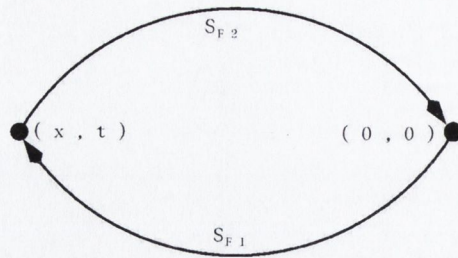


Figure 3-1: A schematic of a 2-point correlation function for local interpolating operators.

we may write this in terms of  $S_F(\mathbf{x}, t; 0)$ . This leads to a huge computational saving, since the propagators from the origin to all other points on the lattice (point-to-all propagators) are thereby sufficient to calculate the correlator for all allowed values of  $t$ . This amounts to calculating just twelve columns of Feynman propagator, Eq. (3.4), one for each spin-colour degree of freedom at the space-time origin. Each of these can be easily calculated using a conjugate gradient solver which solves

$$Mx = y$$

for  $x$  by repeated application of matrix  $M$  given vector  $y$ . It is the most prominent iterative method for solving sparse linear systems. To calculate a column of  $M^{-1}$  we simply place a single non-zero entry in vector  $y$ .

## 3.2 All-to-All Propagators

The use of point-to-all propagators places restrictions on the available physics since we can only calculate quantities that can be extracted from hadron two-point functions (such as in Fig. (3-1)), or a restricted class of multi-point functions that can be reduced to that of connected two-point functions. This primarily restricts us to the flavour non-singlet spectrum since flavour singlet mesons, as well as condensates and other quantities such as mixing phenomena between fermionic and glueball states, contain quark loops, Fig.( 3-2), which require propagators with sources everywhere in space. The calculation of these quark loops would require propagators from all points in space to all other points, or an *all-to-all* propagator.

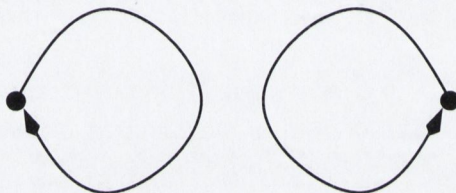


Figure 3-2: A schematic of the disconnected, or hairpin, contribution to correlation functions for local interpolating operators.

Point propagators also throw away a large portion of the information contained in the gauge configurations. One would like to take advantage of self-averaging effects by exploiting the translational invariance of the QCD ground state. Applying this to Eq. (3.10) yields

$$C^{BA}(\mathbf{p}, \Delta t) = -\frac{1}{L^3 T} \sum_{\mathbf{x}, \mathbf{y}, t} e^{-i\mathbf{p} \cdot (\mathbf{x} - \mathbf{y})} \langle \text{Tr}(S_{F2}(\mathbf{y}, t; \mathbf{x}, t + \Delta t) \Gamma^B S_{F1}(\mathbf{x}, t + \Delta t; \mathbf{y}, t) \Gamma^A) \rangle \quad (3.11)$$

where we have taken an average over all  $L^3 T$  point-sources on the lattice. It is likely that a limited number of computationally expensive gauge configurations with light dynamical fermions will be available in the near future, and it will be highly desirable to extract as much information as possible from these lattices. Utilising translational invariance to do this again requires the use of all-to-all propagators in Eq. (3.11).

Furthermore, point propagators restrict the interpolating operator basis used, for

example, to produce early plateaux in effective masses, since a new inversion must be performed for every operator that is not restricted to a single lattice point. An example of this is the extended  $O^{++}$   $P$ -wave operator  $\bar{\psi}\vec{\gamma}\cdot\vec{p}\psi$ , where  $\vec{p}$  is the symmetric spatial difference operator

$$p_j\phi(\mathbf{x}) = U_j(\mathbf{x})\phi(\mathbf{x} + \mathbf{j}) - U_j^\dagger(\mathbf{x} - \mathbf{j})\phi(\mathbf{x} - \mathbf{j}).$$

Since we require information on neighbouring sites to apply this operator, it is not possible to apply it using the point-propagator technique without additional inversions.

All-to-all propagators provide a solution to all the problems associated with point-to-all propagators, but are usually too expensive to compute exactly as this requires an unrealistic number of quark inversions for typical lattice sizes. Stochastic estimation [27, 29, 30, 31, 32, 33, 28] is a common technique used to represent the Feynman propagator. However these estimates tend to be very noisy and variance reduction techniques are crucial in order to separate the signal from the noise.

Others employ the use of a truncated spectral decomposition [25, 26]. It is natural to expect that the long-range physics of QCD is contained in the lowest-lying eigenvectors [35], and these will then dominate in the spectral representation of the mesonic correlator. The issue in this case is knowing how many low-lying eigenmodes suffice to bear out the important features of the long-range physics in practical instances.

Some [28, 34] (and suggested by [36]) have also employed combinations of the two methods to improve efficiency and the error behaviour of results.

The general ideas of these methods shall be explained in the following sections, leading to a particular implementation of a truncated spectral decomposition corrected by a stochastic estimator method which utilises a sub-space thinning technique, *dilution*, to reduce noise.

### 3.3 Stochastic Estimation

Either formally or as a result of numerical practicality, many physical systems, be they classical or quantum mechanical, are boiled down to solving matrix equations. The standard computational tool for systems of this type is the use of a *conjugate gradient* algorithm to solve  $M\mathbf{x} = \mathbf{y}$  for  $\mathbf{x}$ , given  $\mathbf{y}$  and a matrix  $M$ . When the dimension of the relevant matrix grows fast with the physical variables of the problem, the limit of computational feasibility is rapidly approached. The Dirac quark matrix in LQCD is an example of such a system, since the dimension of the matrix grows as  $L^3 \times T$ . This computational limitation is particularly apparent when we wish to calculate the full inverse of the matrix  $M$ , such as in the calculation of the all-to-all propagator.

With a *point* source, where there is only a single non-zero element of the vector  $\mathbf{y}$ , a conjugate gradient algorithm would return a single column from  $M^{-1}$ , such as in the calculation of the point-to-all propagator. For a full inversion, we would need to compute  $N$  of these point source inversions, where  $N$  is the dimension of the matrix. For the Dirac quark matrix this becomes a prohibitive task, for reasonable lattice sizes, due to the scaling behaviour with respect to the lattice volume.

We may limit the number of conjugate gradient inversions by stochastically sampling the vector space of the  $N \times N$  matrix  $M$  and constructing an estimate of the inverse from this sample space. We introduce an ensemble of  $N_R$  independent column vectors,  $\eta_{[1]}, \dots, \eta_{[N_R]}$ , of dimension  $N \times 1$  with the properties of white noise,

$$\langle\langle \eta^i \rangle\rangle = 0 \quad \text{and} \quad \langle\langle \eta^i \eta^{j*} \rangle\rangle = \delta^{ij}, \quad (3.12)$$

where  $\langle\langle \dots \rangle\rangle$  is the expectation value over the ensemble of noise vectors and  $\eta_{[r]}^i$  is the  $i^{\text{th}}$  element of noise vector  $\eta_{[r]}$ . The expectation value of the matrix element  $(M^{-1})^{ij}$  can be obtained by finding the solution,  $\psi_{[r]}$ , to  $M\psi_{[r]} = \eta_{[r]}$  for all  $r$  in the ensemble, and evaluating

$$\langle\langle \psi^i \eta^{j*} \rangle\rangle = \sum_k (M^{-1})^{ik} \langle\langle \eta^k \eta^{j*} \rangle\rangle = (M^{-1})^{ij}. \quad (3.13)$$

So, from  $N_R$  conjugate gradient inversions we can obtain a *noisy* estimate of the full inverse.

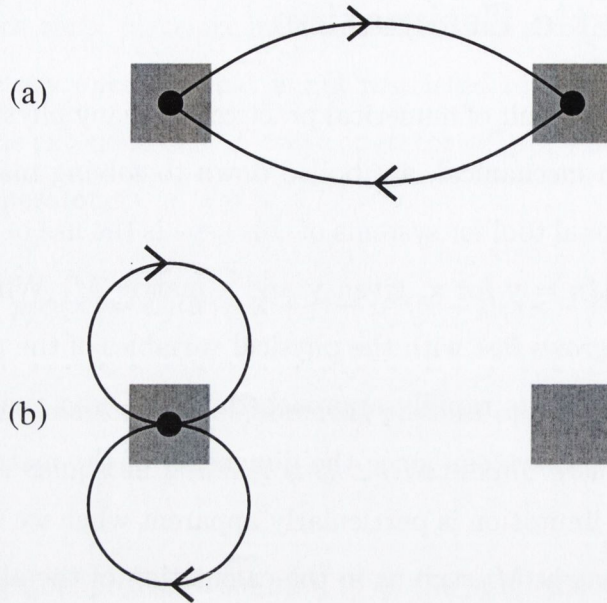


Figure 3-3: Cartoon of the contributions to the noise of the stochastic estimate of a matrix inverse. (a) is the contribution from terms from the first sum in Eq. (3.14) and (b) are contributions from the second sum. With subspace thinning, the shaded boxes indicate that the elements are in the same subspace. In the homeopathic limit, diagram (a) does not contribute. For  $Z(\mathcal{N})$  noise diagram (b) never contributes.

If we let  $X^{ij} = \eta^i \eta^{j*}$ , the variance of the matrix inverse due to the stochastic estimation is composed of two summations [64],

$$\begin{aligned}
 \text{Var}[\text{Tr} M^{-1} X] &\equiv \langle |\sum_{i,j} (M^{-1})^{ij} X^{ji} - \text{Tr} M^2| \rangle \\
 &= \sum_{i \neq j} \left( \langle |X^{ji}|^2 \rangle |(M^{-1})^{ij}|^2 + (M^{-1})^{ij} (M^{-1})^{ji*} \langle (X^{ij})^2 \rangle \right) \\
 &\quad + \sum_i \langle |(X^{ii} - 1)^2| \rangle |(M^{-1})^{ii}|^2.
 \end{aligned} \tag{3.14}$$

The second sum is proportional to the square of the diagonal error only. A graphical representation of the contributions to an elements noise from these summations can be seen in Fig. (3-3).

This technique has an obvious application for all-to-all propagators in lattice QCD. However, in the form above, the correlation functions computed from it are dominated by the noise that we have introduced. Each element of our estimate has the same constant error. For a correlation function of the form of Eq. (3.7), we

are trying to extract an exponentially decaying signal from an all-to-all propagator estimate that has this constant error in all elements. Hence, the signal to noise ratio decays exponentially with the temporal separation of two space-time points.

The first step towards improving this signal to noise ratio is the selection of the type of white noise utilised in the simulation. Any noise satisfying Eq. (3.12) can be used in our estimation. Since  $Z(\mathcal{N})$  noise has no diagonal error, and hence the second summation cannot contribute in Eq. (3.14), it produces a minimal error.

### 3.3.1 Noise Reduction with Subspace Thinning

Much work has gone into methods for reducing further the noise variance of stochastic estimation [27, 30, 31, 32, 33, 34] using both Gaussian and  $Z(\mathcal{N})$  noise. Decomposing the vector space,  $V$ , of the matrix  $M$  into  $s$  disjoint subspaces (*subspace thinning*),

$$V = V^{(1)} \oplus V^{(2)} \oplus V^{(3)} \dots \oplus V^{(s)}, \quad (3.15)$$

is a method employed by many [27, 30, 32, 34]. There are at most  $N$  of these non-overlapping subspaces.

One can then decompose the ensemble of noise vectors into each of the vector subspaces,  $\eta_{[i]} = \sum_{r=1}^s \eta_{[i]}^{(r)}$ , yielding an ensemble,

$$\left\{ \{ \eta_{[1]}^{(1)}, \eta_{[1]}^{(2)}, \dots, \eta_{[1]}^{(s)} \}, \{ \eta_{[2]}^{(1)}, \eta_{[2]}^{(2)}, \dots, \eta_{[2]}^{(s)} \}, \dots, \{ \eta_{[N_R]}^{(1)}, \eta_{[N_R]}^{(2)}, \dots, \eta_{[N_R]}^{(s)} \} \right\}. \quad (3.16)$$

The expectation values of white noise still apply,

$$\left\langle \left\langle \sum_{r,t=1}^s \eta^{i(r)} \eta^{j(t)*} \right\rangle \right\rangle = \delta^{ij}, \quad (3.17)$$

but the subspace decomposition implies

$$\eta^{i(r)} \eta^{j(t)*} = X^{i(r)j(t)*} = \delta^{(r,t)} X^{i(r)j(t)*} \quad (3.18)$$

even before expectation values are taken. In Eq. (3.14), we can see that subspace

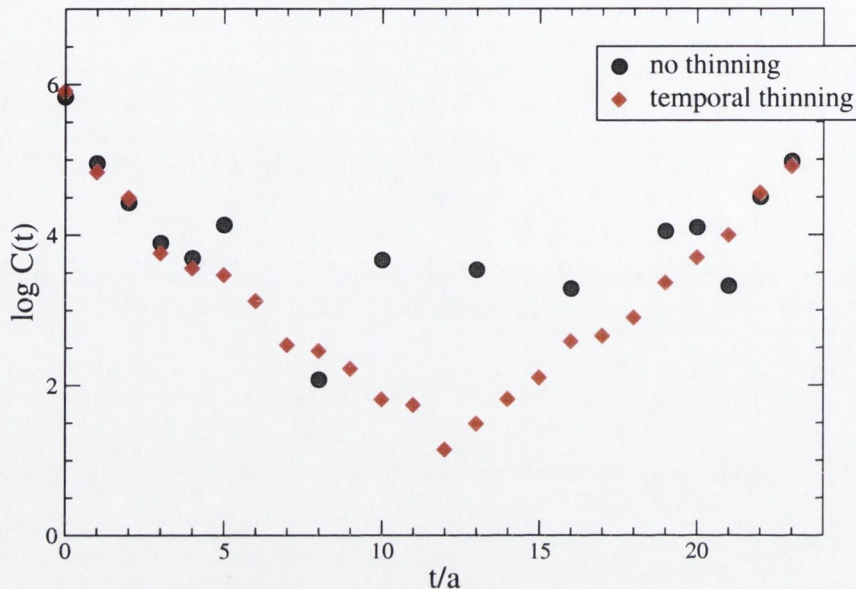


Figure 3-4: The pseudoscalar propagator computed with and without temporal subspace thinning.

thinning will, therefore, reduce the first summation to a sum over  $\sum_{i \neq j}$  where  $i$  and  $j$  are in the same subspace *before* expectation values are taken. This reduction in the summation is true for any white noise and in the *homeopathic* limit of  $s = N$  subspaces this first sum is automatically zero since  $i$  and  $j$  cannot be in the same subspace. For  $Z(\mathcal{N})$  noise the second sum is also zero and we have zero variance in the homeopathic limit.

The cost of this lower variance is  $(s - 1) \times N_R$  additional conjugate gradient inversions. For this method to pay off, we require that its variance is less than that of the original method with the equivalent number of inversions. To illustrate such an equal cost test we employ a method analogous to the “*wall source on every timeslice*” method used by the authors of Ref. [32] for the case where  $M$  is the Dirac matrix. Since we are attempting to measure temporal correlations in hadronic quantities, we decompose the noise vector(s) into pieces that have non-zero support only on a single timeslice,  $\eta = \sum_{t=1}^{NT} \eta^{(t)}$ , splitting the vector space into  $NT$  subspaces, where

$NT$  is the number of timeslices. In Fig. (3-4), we show the effect that this has on a pseudoscalar propagator for a  $12^3 \times 24$ , i.e.  $NT = 24$ , lattice. The circles are the average of 24 noise sources without any thinning and the diamonds are from a single noise vector which has been thinned in temporal subspaces, both using  $Z(4)$  noise.

As expected, for small temporal separations, where the signal is largest, the estimates from both methods agree but, in the case of the original method, as we extend further in the temporal direction the noise overwhelms the signal and the exponential decay of the pseudoscalar propagator is difficult to determine. With temporal subspace thinning we maintain a strong signal right across the lattice and the exponentially decaying behaviour of the correlation function is easily apparent.

The signal decays as  $e^{-m_\Gamma t}$  where  $m_\Gamma$  is the mass of the state we want to measure. Therefore the temporal indices of  $M^{-1}\Gamma$ , which is what we are estimating in a correlation function, are highly diagonally dominant. Temporal subspace thinning excludes all but a small fraction ( $1/NT$  where  $NT$  are the number of timeslices) of the contributions of the largest terms to the noise of an element.

### 3.3.2 Dilution

The fact that temporal subspace thinning can have such a dramatic effect indicates that we may be able to use the physical parameters of the problem to help separate the signal from the noise in our correlation functions. The authors of Ref. [27] found that sub-space thinning in spin space, the “*spin explicit method*”, also yielded dramatic improvements in an equal-cost evaluation of scalar and axial vector insertions. In [30], Wilcox also found that sub-space thinning in spin and colour spaces had strong effects on results for flavour singlet quantities.

Here we follow this process to its logical conclusion and allow thinning in some subset of the spatial, temporal, spin and colour subspaces, as suggested by [30], using  $Z(4)$  noise for each (complex) component of the noise vectors. The particular choice of subset in a simulation we call a “*dilution*” level. As shown above, the homeopathic limit of the dilution procedure, where we have one noise vector for each time, space, colour and spin component, results in the *exact* all-to-all propagator in

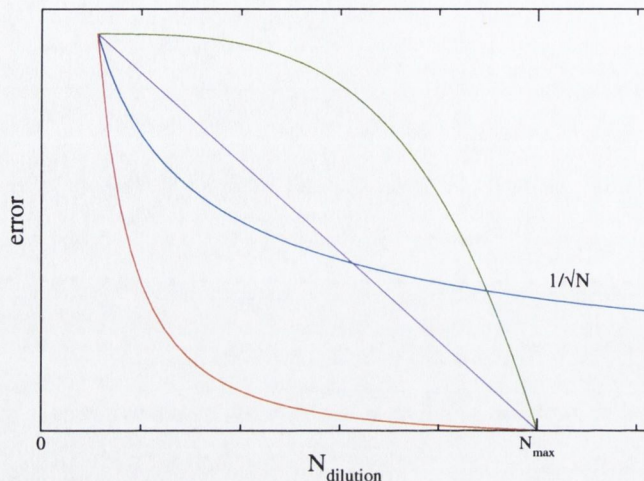


Figure 3-5: A cartoon of possible deviations of the stochastic estimates of the exact solution (at  $N_{dil} = N_{max}$ ) for different dilution paths. Simply adding noise vectors will give a  $1/\sqrt{N}$  behaviour. We have found that simple dilutions typically follow the behaviour exhibited by the bottom curve.

a finite number,  $N$ , of steps due to the diagonal property of  $Z(4)$  noise,

$$\eta_{i\alpha}(x)^* \eta_{i\alpha}(x) = 1, \quad (3.19)$$

where  $i$  denotes colour,  $\alpha$  spin and  $x$  is the space-time index of the complex noise vector component  $\eta_{i\alpha}(x)$  of dimension  $N$ . This limit cannot be reached in practice on reasonable lattices (as discussed previously), but the path of dilution may be optimised so that the noise from the gauge fields dominate the errors in the hadronic quantities of interest with only a small, manageable number of conjugate gradient inversions, see Fig. (3-5).

It is convenient, at this stage, to introduce a dilution index to the noise (and solution) vectors, this shall be contained in brackets to differentiate it from the spin-colour or space-time indices of a vector. A noise source is diluted in some set of variables ( $j$ ) such that  $\eta = \sum_j \eta^{(j)}$ , and each diluted source is inverted, yielding  $N_{dil}$  pairs of vectors,  $\{\psi^{(j)}, \eta^{(j)}\}$ . These then give an unbiased estimator of the Feynman

propagator,  $S_F$ , with a *single* noise source,

$$\sum_{i=0}^{N_{dil}-1} \psi^{(i)}(\mathbf{x}, t) \otimes \eta^{(i)}(\mathbf{x}_0, t_0)^\dagger \stackrel{N_{dil} \rightarrow N}{=} S_F(\mathbf{x}, t; \mathbf{x}_0, t_0), \quad (3.20)$$

where we suppress the spin/colour indices.

It is also convenient to introduce notation for the inner product (dot product),  $\langle u, v \rangle$ , of two quark vectors,  $u$  and  $v$ ,

$$\langle u(t), v(t) \rangle \equiv \sum_{\mathbf{x}, \alpha, i} u_{i\alpha}(\mathbf{x}, t)^* v_{i\alpha}(\mathbf{x}, t). \quad (3.21)$$

If the  $t$ -argument is absent from either of the vectors, the product is taken to be a global dot product, i.e. summed over all  $t$ . Using this notation we may rewrite our equation for the all-to-all correlation function, Eq. (3.11), in terms of the noise and solution vectors,  $\eta^{(i)}$  and  $\psi^{(i)}$ , used in our estimation of the Feynman propagators,

$$C^{BA}(\Delta t) = -\frac{1}{L^3 T} \sum_{i,j,t} \langle \eta_{[1]}^{(i)}(t + \Delta t), \Gamma^B \psi_{[2]}^{(j)}(t + \Delta t) \rangle \langle \eta_{[2]}^{(j)}(t), \Gamma^A \psi_{[1]}^{(i)}(t) \rangle, \quad (3.22)$$

where we use independent noise vectors for each of the two Feynman propagators in the correlation and the momentum projections has been incorporated into the definition of the operators  $\Gamma^A$  and  $\Gamma^B$ .

In Table 3.1 we list the allowed subspace thinnings that we use. We can combine any subspace thinning in each of space, time, spin and colour components of the noise vectors to produce different dilution levels. The number of inversions required for a particular dilution level,  $N_{dil}$  is given by the product of the factors derived from each components subspace thinning. The magnitude of the effect of time dilution was observed to be so significant, for the hadronic correlation functions that we calculated, that it is always included. The only restriction on dilution is placed on the spatial components, since a full spatial dilution would require a prohibitive multiplicative factor of  $L^3$  inversions.

As an illustration of the dilution dependent behaviour of the errors from a correlation function, a quenched simulation was performed using different dilution levels

Component	Dilution Type	Reference	$N_{dil}$ factor
Time	Full	Tf	$NT$
Space	Face Centre Cubic	Sc	8
	Body Centre Cubic	Se	2
	None	Sx	1
Colour	Full	Cf	3
	None	Cx	1
Spin	Full	Gf	4
	Even-Odd	Ge	2
	None	Gx	1

Table 3.1: Details of the available dilutions for each component and the extra multiplicative factor for inversions that they incur. Also included is a quick reference for each of the dilutions.

on a small lattice with an unimproved Wilson action. The parameters of the simulation are given in Table 3.2. The use of a small lattice size allows us to extend to the homeopathic limit so that we can compute the exact all-to-all propagator and, hence, the gauge field fluctuation errors. We can then compare these to the errors obtained by other, non-exact dilution levels which contain both the gauge field fluctuation and the stochastic noise error.

# gauge configurations	10
Volume	$4^3 \times 8$
$\beta$	5.0
$\kappa_s$	0.13
$\kappa_t$	0.13

Table 3.2: Details of the quenched Wilson simulation used in the study of the dilution dependent behaviour of correlation functions.

We study the error behaviour of three interpolating operators that have a large coupling to the pion ( $0^{-+}$ ),  $\rho$  meson ( $1^{--}$ ) and the  $1^{++}$  P-state respectively. The correlation functions for these mesons are determined by substituting

$$\begin{aligned}
(\Gamma^A)^\dagger &= \Gamma^B = \gamma_5 & \text{for } \pi \\
(\Gamma^A)^\dagger &= \Gamma^B = \gamma_z & \text{for } \rho_z \\
(\Gamma^A)^\dagger &= \Gamma^B = (\vec{\gamma} \times \vec{p})_z & \text{for } 1_z^{++},
\end{aligned}$$

in Eq. (3.22),  $\vec{p}$  shall be defined in Eq. (4.10). The possible choices of operators shall be discussed in detail in Section 4.2.

$N_{dil}/NT$	1	2	3	4	6	8
Reference	TfSxCxGx	TfSxCxGe	TfSxCfGx	TfSxCxGf	TfSxCfGe	TfSeCxGf
$N_{dil}/NT$	12	16	24	32	48	96
Reference	TfSxCfGf	TfScCxGe	TfScCfGx	TfScCxGf	TfScCfGe	TfScCfGf

Table 3.3: Table of the dilution levels used in the simulations and reference codes (see Table 3.1) for the subspace thinnings from which they are derived.

In Fig. (3-6), Fig. (3-8) and Fig. (3-9) we plot the value of the correlator at a timeslice and its error, determined by a bootstrap sampling from the ensemble of gauge configurations, against the level of dilution used. In Table 3.3 we list the subspace thinnings that give each dilution level. We do this for three independent timeslices of the lattice in each case. The central value using the exact propagator, given by the homeopathic limit, is used to normalise the values. The gauge fluctuation errors determined from the gauge field ensemble, are given by the dashed horizontal lines.

The calculation of the ground state energy of a pion does not require the extra computational power that an all-to-all propagator method demands, and can be extracted with reasonable accuracy using a point-to-all method. For this reason we also investigate the behaviour of a higher momentum state since the injection of momentum gives rise to increased noise that makes a signal difficult to extract in a point-to-all analysis. In Fig. (3-7) we have an analogous plot to Fig. (3-6) for a pion with a lattice unit of momentum in each spatial direction ( $\vec{p} = \frac{2\pi}{L}(1, 1, 1)$ ). It is interesting to note that while there is an observed increase in the error of the correlator for this higher momentum state, as expected, the gauge fluctuation determined from the homeopathic limit is in fact decreased. The essential behaviour of the two does not, however, appear to change with the injection of momentum.

We can see that in the homeopathic limit, the errors on the correlator for the  $\rho$  meson in Fig. (3-8) are comparable to those of the pion in Fig. (3-6). The P-state is typically very noisy in the point-to-all case, from Fig. (3-9), we can see from the gauge

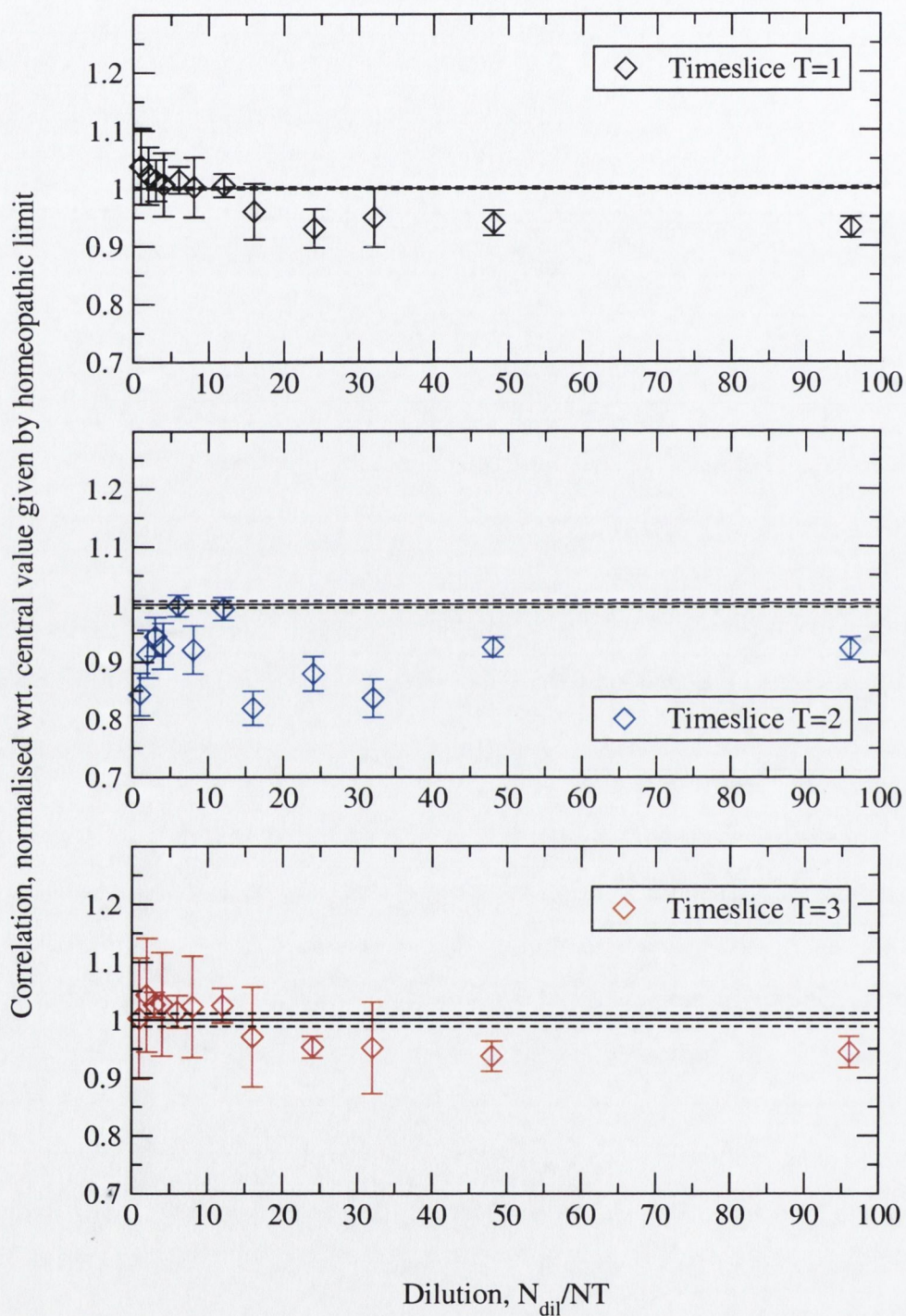
$\pi$ 

Figure 3-6: The normalised value of the correlation function plotted against the dilution level,  $N_{dil}/NT$ , for the pion on three different timeslices. The dashed lines give the gauge field fluctuations about the normalisation.

$\pi$ ,  $P=(1,1,1)$

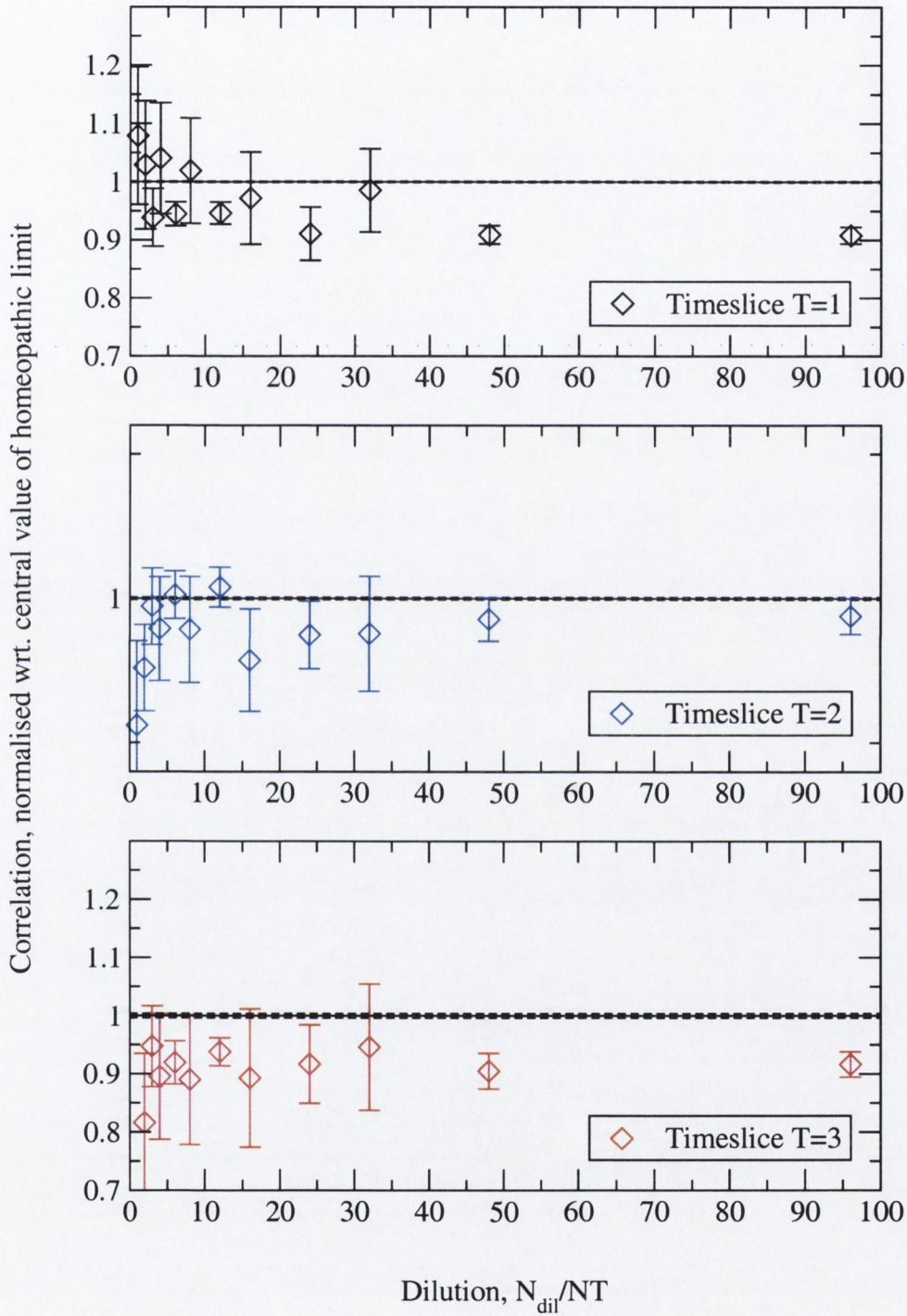


Figure 3-7: The value of the correlation function plotted against the dilution level  $N_{dil}/NT$  for the pion, with a unit of momentum in each spatial direction, on three different timeslices. The dashed lines give the gauge field fluctuations about the normalisation.

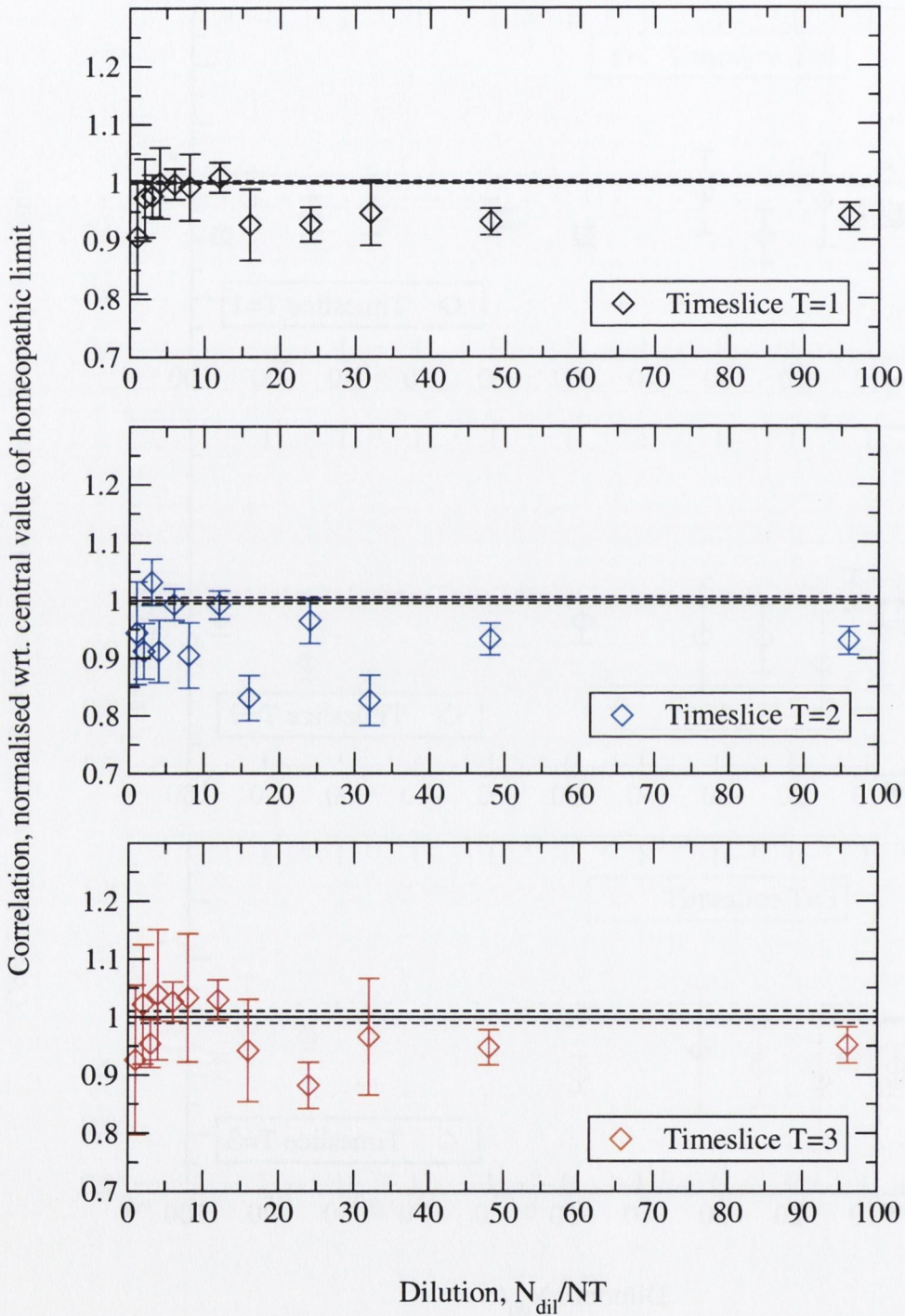
$\rho$ 

Figure 3-8: The value of the correlation function plotted against the dilution level  $N_{dil}/NT$  for the  $\rho$  meson on three different timeslices. The dashed lines give the gauge field fluctuations about the normalisation.

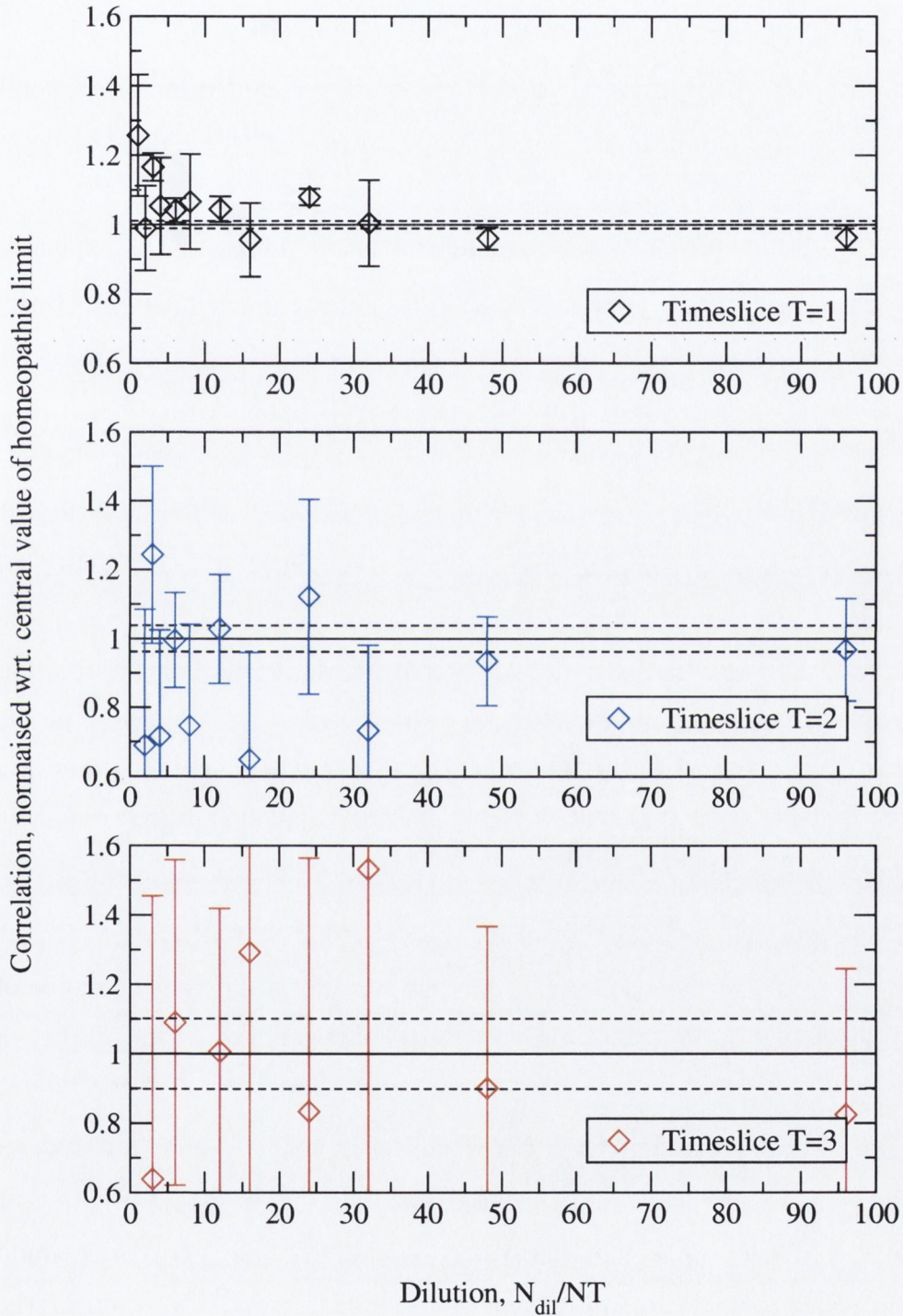
$1^{++}$ 

Figure 3-9: The value of the correlation function plotted against the dilution level  $N_{dil}/NT$  for the  $1^{++}$  P-state on three different timeslices. The dashed lines give the gauge field fluctuations about the normalisation.

field fluctuations that this is inherently so, with gauge errors an order of magnitude higher than the other operators. This would imply that a large number of gauge configurations, and/or the use of an improved fermion action, would be essential for an accurate determination of noisy particles such as the P-state.

It was expected that hadrons with different symmetry properties would respond to different dilution levels in different ways. To investigate this we simulated the  $\rho$  meson and the  $1^{++}$  P-state. From a comparison of Fig. (3-6), Fig. (3-8) and Fig. (3-9) we can see that this variation across operators in response to dilution is not explicitly manifest in our results. The dependence on dilution appears to be similar across the range of operators, for example there is a consistent increase in the determined error between full colour ( $N_{dil}/Nt = 3$ ) and full spin dilution ( $N_{dil}/Nt = 4$ ).

The dependence on dilution itself is, however, manifest in our results. For instance, note the (large) increase in errors on the omission of colour dilution at  $N_{dil}/Nt = 4, 8, 16, 32$ . In general full colour dilution combined with some form of spin dilution (at  $N_{dil}/Nt = 4, 12$ ) yields a consistent and dramatic reduction in the determined error. Perhaps the most notable feature however, is that the dilution does not appear to converge on the value determined from the propagator in the homeopathic limit in either the case of the pion or the  $\rho$  meson. The level of noise in the case of the P-state makes the convergence difficult to determine. The underestimation of the correlation, in the case of the pion and  $\rho$  meson, appears to predominantly occur with the inclusion of face-centre cubic spatial dilution, i.e. at  $N_{dil}/Nt = 16, 24, 32, 48, 96$ . The simulation was repeated for a different ensemble of source noise vectors and the deviation from the observed results was within statistical errors.

The determination of the source of this deviation is difficult since it would require an increase in the lattice volume. Indeed with the self-averaging effects that a larger volume would induce it may disappear altogether. A larger volume would certainly help narrow potential candidates for this error but would also render the determination of the homeopathic limit extremely intensive computationally.

### 3.3.3 Recycling Noise Vectors

As stated previously, the use of dilution gives an unbiased estimator of the Feynman propagator,  $S_F$ , with a single noise source. If it is possible to store a set of diluted noise and solution vectors we can reuse them in the contraction of the correlation function. In other words, one can generate an ensemble of  $N_R$  noise vectors,  $\eta_{[r]}$ , save the corresponding diluted solutions to disk and perform the contraction,

$$C^{BA}(\Delta t) = -\frac{1}{L^3 T N_R (N_R - 1)} \sum_{i,j,t,r < s} \langle \eta_{[r]}^{(i)}(t + \Delta t), \Gamma^B \psi_{[s]}^{(j)}(t + \Delta t) \rangle \langle \eta_{[s]}^{(j)}(t), \Gamma^A \psi_{[r]}^{(i)}(t) \rangle \quad (3.23)$$

utilising  $\sim N_R^2$  samples of the correlation function of Eq. (3.22). The errors correspondingly decrease faster than the naive  $1/\sqrt{N_R}$ , although the measurements are somewhat correlated. We have seen in our preliminary tests that the error reduction is comparable to some dilution choices. It is clear that if one can afford to save the noise and solution vectors, then this is a straightforward method of variance reduction for the specific case of mass-degenerate mesons.

## 3.4 Truncated Spectral Decomposition

A spectral representation of the inverse of a matrix  $M$  of rank  $N$  is given by

$$M^{-1} = \sum_i^N \frac{1}{\lambda_{(i)}} v^{(i)} \otimes v^{(i)\dagger}, \quad (3.24)$$

where  $v^{(i)}$ ,  $\lambda_{(i)}$  are the eigenvectors and eigenvalues of  $M$ , i.e.,  $M v^{(i)} = \lambda_{(i)} v^{(i)}$ . In the case where  $M$  is the Dirac matrix, it is clear that if one can calculate all its eigenmodes, one can construct the all-to-all propagator. Of course, computing all the eigenmodes for a reasonably sized lattice is, again, an unfeasible task.

One can use the lattice however in an effort to obtain insight into the structure of light hadrons by finding the paths that dominate the QCD path integral. The spectra of Wilson-Dirac type matrices have an elliptic shape with the real parts of the eigenvalues being positive. Since the Wilson term is designed to give the doublers

a high energy, the large eigenmodes correspond to these doublers and only the smaller ones should contain physics [37]. There are also theoretical arguments that suggest that low-lying modes of the Dirac operator should embody the important features of fermionic physics in the chiral regime [35, 36]. Both these views are supported by numerical evidence from lattice simulations [25, 34]. For sufficiently light quark masses, expansion in a basis that contains these low-lying modes should cover the essential infrared physics in hadronic interactions.

There are two options to proceed, based on the spectral representations of the Wilson-Dirac matrix  $M$  and the hermitian matrix  $Q = \gamma_5 M$ . In [25], a comparison of the truncated spectral sum of the pion propagator shows poor and ragged convergence for the non-hermitian version when adding additional eigenvectors. The hermitian version shows stable and even convergence. For chiral fermions the choice is irrelevant. Also, the hermiticity of  $Q$  allows for a simple ordering of the orthogonal eigenmodes and a natural definition of the low-lying modes. For these reasons, we choose to proceed with the hermitian matrix  $Q$ . The Feynman propagator is given by  $M^{-1} = Q^{-1}\gamma_5$ , where  $Q^{-1}$  is given by the sum over all eigenmodes,

$$Q^{-1}(\mathbf{y}, y_0; \mathbf{x}, x_0)_{\alpha\beta}^{jk} = \sum_i^N \frac{1}{\lambda^{(i)}} v_{j\alpha}^{(i)}(\mathbf{y}, y_0) \otimes v_{k\beta}^{(i)}(\mathbf{x}, x_0)^\dagger, \quad (3.25)$$

where the index in brackets  $(i)$  denote the eigenmode, the Latin indices  $(j, k)$  denote colour and the Greek indices  $(\alpha, \beta)$  denote spin. One can expect that truncating this sum, Eq. (3.25), at some finite  $N \rightarrow N_{ev}$  should thus yield a good estimate of the quark propagator for practical purposes.

### 3.4.1 Extracting Low-lying Modes

We follow the method of [25] and determine the eigenmodes by use of the Arnoldi package [38]. The Arnoldi method is designed for non-hermitian matrices and reduces, when applied to a hermitian matrix, to the Lanczos method with implicit restarting.

The properties of the Lanczos algorithm imply that we get convergence to those eigenvalues represented in the starting vector and fastest convergence to those in the

ends of the spectrum. The better separated they are from the rest of the eigenvalues, the faster will they converge [39]. In general the relative separation of the lowest eigenvalues is often poor, since the separation is relative to the whole spread of the spectrum, not to the distance to the origin. For this reason we must execute a preparatory step where we map, by means of a suitable polynomial  $q : Q \mapsto q(Q)$ , the low-lying modes from the inside of the spectrum to the surface. To accelerate the convergence, we then use Chebyshev polynomials to precondition the problem by decreasing the level density in the spectral region of interest.

Firstly, construct the polynomial

$$q(Q) = \frac{2}{s^2}Q^2 - (1+r)I \quad (3.26)$$

where  $s$  is the spectral radius of  $Q$  and  $r$  represents a shift operation that controls the window of desired eigenmodes. This maps the spectrum of  $Q$  into the region  $[-1, 1]$  and then shifts the  $r$  sized window outside this region. Since Chebyshev polynomials  $T_N$  of degree  $N$  have a rapid increase outside the interval  $[-1, 1]$ , within which they are close to zero, we can decrease the level density of eigenvalues by their application. We use the recurrence relation for Chebyshev polynomials

$$T_{n+1}(x) = 2xT_n(x) - T_{n-1}(x) \quad (3.27)$$

where  $T_0(x) = I$  and  $T_1(x) = x$  to generate a Chebyshev polynomial of degree  $N$ . We now calculate the the eigenmodes  $v^{(i)}$  of largest moduli of  $T_N \circ q \circ Q$ , which correspond to the low-lying modes of  $Q$ , the eigenvalues of which we obtain through the Rayleigh quotient

$$\lambda^{(i)} = \frac{v^{(i)\dagger} Q v^{(i)}}{v^{(i)\dagger} v^{(i)}} \quad (3.28)$$

There are two main questions that arise from the proposition of truncating the spectral decomposition to approximate the all-to-all propagator. Firstly, does the truncation give a good estimate of the propagator in practice and, secondly, if it does,

how many eigenmodes suffice to bear out the important features of the long range physics in practical instances. Both of these questions have been addressed in detail by [25]. Here we illustrate the behaviour of a truncated spectral representation with respect to an increasing number of eigenmodes by employing the use of two different lattice volumes,  $4^3 \times 4$  and  $4^3 \times 8$ . The parameters used in simulations for both cases are given by Table 3.4.

# gauge configurations	10	10	10
Volume	$4^3 \times 8$	$4^3 \times 4$	$4^3 \times 4$
$\beta$	5.0	5.0	5.0
$\kappa_s$	0.13	0.13	0.1675
$\kappa_t$	0.13	0.13	0.1675

Table 3.4: Details of the quenched Wilson simulations for the study of increased eigenmode dependence of correlation functions using the truncated spectral decomposition method for an all-to-all propagator.

Firstly a simulation was performed at  $\kappa = 0.13$  on the  $4^3 \times 8$  lattice. Of the possible 6144 eigenvectors, just under 3000 of the lowest-lying modes were calculated. In the first column of graphs of Fig. (3-10) we plot the value of the correlation function against the number of eigenmodes used in the truncation for the pion,  $\rho$  meson and  $1^{++}$  meson. Due to the time-inversion symmetry of a lattice with periodic boundary conditions, there are only five independent timeslices of a correlation function determined on a  $4^3 \times 8$  lattice. We evaluate this correlation-eigenmode relationship for the 3 timeslices which are not on the boundaries, i.e  $t = 1, 2, 3$ . The horizontal lines give the values of the correlation determined by the homeopathic limit of dilution.

The most obvious feature of these graphs is that for each particle and each timeslice the eigenmode determination saturates at a point that greatly overestimate the actual value of the correlation. From this saturation point it decreases slowly to the exact value as additional eigenmodes are added. To observe this behaviour completely we restrict ourselves to an identical simulation on a  $4^3 \times 4$  lattice and calculate all eigenmodes. This can be seen in the second column of Fig. (3-10). In this case there are only three independent timeslices of a correlation function and we plot each of these. Only one of these timeslices does not lie on the boundaries of this region,

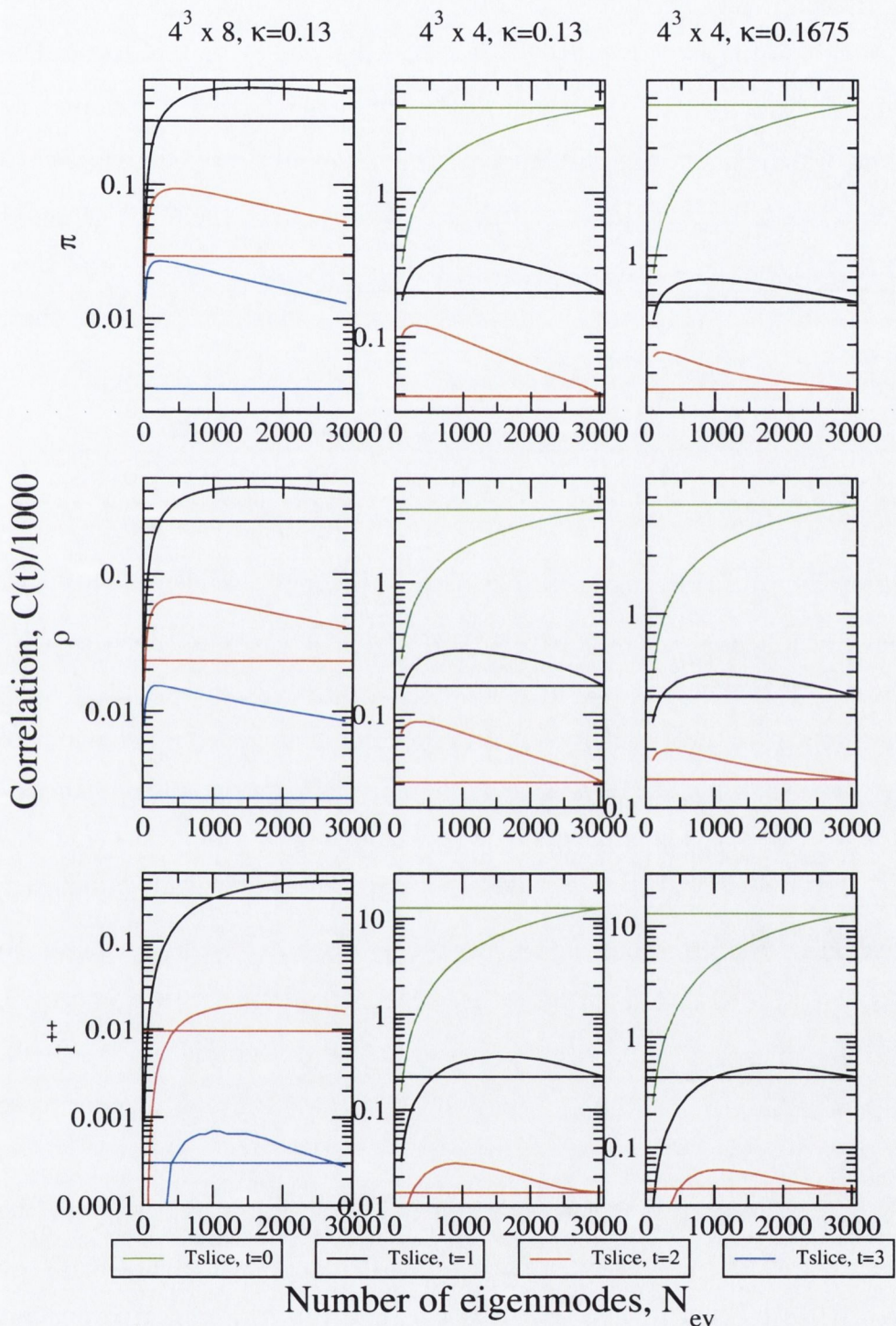


Figure 3-10: The value of the pion correlation function determined from an increasing number of eigenmodes determined for the  $\pi$ ,  $\rho$  and  $1^{++}$  mesons for simulations on both a  $4^3 \times 8$  and a  $4^3 \times 4$  lattice. The horizontal lines give the value of the correlators as determined by the exact propagator.

$t = 1$ , and one should expect large corrections at the boundary points.

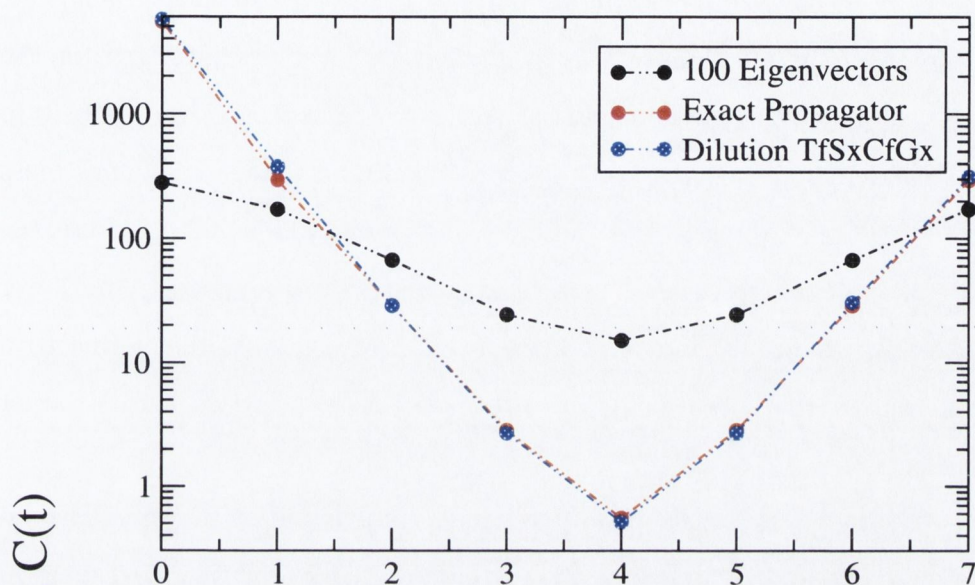
As we might expect, all eigenmodes contribute at small temporal distances which is manifest in the monotonically increasing behaviour at  $t = 0$  for each particle. The behaviour of timeslices  $t = 1, 2$  are similar to that observed for the non-boundary timeslices of the  $4^3 \times 8$  simulation, although one should expect large corrections to the  $t = 2$  in this case due to contamination from the backwards propagating temporal mirror-state. These timeslices saturate at some low number of eigenmodes and then gradually decrease to the value obtained from the exact propagator. We note that, as expected, the value of the correlation determined from the homeopathic limit of dilution and that of the full spectral decomposition match exactly.

From both simulations we observe a saturation point that is a function of both the operator and timeslice. The number of eigenmodes required before saturation varies from operator to operator and is largest in the case of the most troublesome particle, the  $1^{++}$ . At timeslice  $t = 3$ , for example, the saturation occurs at  $\sim 220$  eigenmodes for the pion, at  $\sim 260$  eigenmodes for the  $\rho$  meson and at  $\sim 1000$  eigenmodes for the  $1^{++}$  meson (all on the  $4^3 \times 8$  lattice). For each operator however, the behaviour of the saturation point with respect to increasing temporal separation is identical: as  $t$  increases the lowest-lying eigenmodes become increasingly dominant.

The overestimation of the correlation function at the saturation point, we believe, is a manifestation of the mass dependence of the low-eigenmode dominance. To investigate this we repeat the simulation on the  $4^3 \times 4$  simulation with  $\kappa = 0.1675$ . The results of this simulation can be seen in the third column of graphs in Fig. (3-10). While the overestimation at saturation is still apparent, we observe a large decrease in its magnitude.

This mass dependence can also be observed in Fig. (3-11), where we plot the correlation function of the pion as determined from 100 eigenvectors on the  $4^3 \times 8$  lattice compared to that of the exact propagator determined by the homeopathic limit of dilution, and that of a lower dilution level. We also plot the correlation function of the pion from 100 eigenvectors of a  $12^3 \times 24$ ,  $\kappa = 0.1675$  simulation (whose parameters are given by Table 3.5) against the non-exact dilution level determined on the same

$4^3 \times 8$  Lattice,  $\kappa=0.13$



$12^3 \times 24$  Lattice,  $\kappa=0.1675$

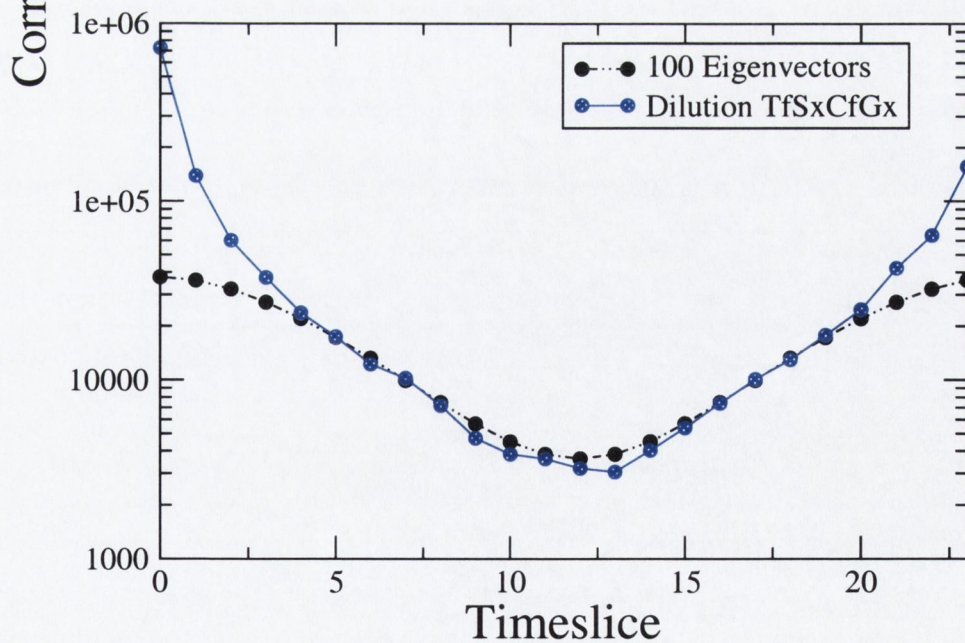


Figure 3-11: The value of the pion correlation function determined from 100 eigenvectors compared to that determined from some dilution levels for simulations on both a  $4^3 \times 8$  and a  $12^3 \times 24$  lattice.

$12^3 \times 24$  lattice. On the  $4^3 \times 8$  lattice, dilution appears to give a good estimate of the exact correlation but, as previously noted, the spectral truncation gives poor matching to the homeopathic limit of dilution. Assuming that the same non-exact dilution level will approximate the correlation equally well on the  $12^3 \times 24$  lattice, the matching between this dilution and 100 eigenvectors is vastly improved for the lower quark mass at  $\kappa = 0.1675$ . We can see that a truncated spectral decomposition does indeed give a good representation of the correlation function for low quark mass in the temporal region of interest, i.e. at large  $t$ , as observed by [25], where the contamination due to higher energy states is exponentially dampened. The lower number of required eigenmodes for a good representation is most likely due to a combination of the increased self-averaging effects given by a lattice with a larger volume and the increased  $\beta$  value.

This temporal dependence of the low-eigenmode dominance for mesonic correlation functions makes anisotropic lattices the ideal candidate for the truncated spectral representation of the all-to-all propagator since the increased resolution in the temporal direction should allow us to isolate a large region where the low-lying eigenmodes dominate. From Fig. (3-10) we can see, however, that the determination of how many eigenmodes suffice to bear out the physics is a non-trivial task and highly dependent on the quark mass and required operator.

One of the problems with a truncated spectral representation is that it violates reflection positivity, making it mandatory to correct it. Reflection positivity is extremely important when studying effective mass plots since it guarantees that the plateau is approached from above. In Fig. (3-12), we shall see that a truncated eigenvector approach clearly violates this property.

### 3.5 A Hybrid Method

Given the preceding discussion, a natural suggestion would be to try to calculate as many as possible of the low-lying eigenmodes exactly and correct for the truncation with the noisy method [36]. This gives rise to two concerns: firstly, the correction should leave the exactly solved low-lying modes intact; and secondly, it should not

introduce large uncertainties in the process. We propose that the use of a stochastic method with noise dilution is a natural way to accommodate both of those concerns.

First, we note that the exact  $N_{ev}$  low-lying eigenmodes obtained separately naturally divide the hermitian Dirac matrix  $Q$  into two subspaces,  $Q = Q_0 + Q_1$ , defined by

$$Q_0 = \sum_{i=1}^{N_{ev}} \lambda_i v^{(i)} \otimes v^{(i)\dagger}, \quad Q_1 = \sum_{j=N_{ev}+1}^N \lambda_j v^{(j)} \otimes v^{(j)\dagger}. \quad (3.29)$$

Similarly, the quark propagator is broken up into two pieces,  $Q^{-1} = \bar{Q}_0 + \bar{Q}_1$ , where  $\bar{Q}_0$  is the truncated version of Eq. (3.25) and  $\bar{Q}_1 = Q^{-1}\mathcal{P}_1$ , where  $\mathcal{P}_1$  is the projection operator

$$\mathcal{P}_1 = \mathbf{1} - \mathcal{P}_0 = \mathbf{1} - \sum_{j=1}^{N_{ev}} v^{(j)} \otimes v^{(j)\dagger}. \quad (3.30)$$

We can correct for the truncation by estimating  $\bar{Q}_1$  using the stochastic method,  $\bar{Q}_1 = \langle\langle \psi \otimes \eta^\dagger \rangle\rangle$  with an ensemble of  $N_R$  noise vectors,  $\{\eta_{[1]}, \dots, \eta_{[N_R]}\}$ . The solutions,  $\psi_{[r]}$ , are given by

$$\psi_{[r]} = \bar{Q}_1 \eta_{[r]} = Q^{-1} (\mathcal{P}_1 \eta_{[r]}). \quad (3.31)$$

This amounts to preconditioning the noise vector with the eigenspace projection  $\mathcal{P}_1$  prior to performing the conjugate gradient inversion.

$\mathcal{P}_1$  is a projector that commutes with  $Q$  (and therefore  $Q^{-1}$ ) and we have

$$\bar{Q}_1 = Q^{-1}\mathcal{P}_1 = \mathcal{P}_1 Q^{-1}\mathcal{P}_1 \quad (3.32)$$

since  $\mathcal{P}_1\mathcal{P}_1 = \mathcal{P}_1$ . Noting also that  $\mathcal{P}_0\mathcal{P}_1 = 0$ , we can use this fact to ensure that our estimator of  $\bar{Q}_1$  explicitly satisfies  $\mathcal{P}_0\bar{Q}_1^{(\text{est})} = 0$  by using the representation  $\bar{Q}_1 = \langle\langle \mathcal{P}_1\psi \otimes \eta^\dagger \rangle\rangle$ . In practice this amounts to applying the projector  $\mathcal{P}_1$  to the solution vector after performing the conjugate gradient inversion. We can then use this explicitly orthogonal vector as an improved solution vector,  $\mathcal{P}_1\psi_{[r]} \rightarrow \psi_{[r]}$ . In simulations, this projection yields a  $\sim 10\%$  improvement in the accuracy of the conjugate gradient inversion at nominal computational cost.

Of course, the commutativity of  $\bar{Q}_1$  and  $\mathcal{P}_1$  also implies that one could perform

the projection  $\mathcal{P}_1$  on the solution vector without the need to firstly precondition the noise vector. The benefit of this projection however is that  $\overline{Q}_1$  has a lower condition number than that of  $Q^{-1}$  since we have removed  $N_{ev}$  of the low-lying modes. A similar idea, “*mode-shifting*”, was employed by [34]; both help solve the critical slowing down of conjugate gradient inversion algorithms induced by low-lying eigenmodes of the Dirac operator for light quarks.

We now apply the idea of dilution to the stochastic estimation of  $\overline{Q}_1$ . Each random noise vector,  $\eta_{[r]}$ , that is generated will be diluted *then* orthogonalised (with respect to  $v^{(i)}$ ) and used to obtain  $\psi_{[r]}$  by means of a conjugate gradient inversion of  $Q$ . In other words, we now have the following set of noise vectors:

$$\left\{ \left( \eta_{[1]}^{(1)}, \dots, \eta_{[N_r]}^{(1)} \right), \dots, \left( \eta_{[1]}^{(N_{dil})}, \dots, \eta_{[N_r]}^{(N_{dil})} \right) \right\} \quad (3.33)$$

where the upper indices denote the dilution and the lower indices label the different noise samples.

We note that there is a natural way to combine the truncated spectral decomposition with dilution to estimate the all-to-all quark propagator. The similarity in the structure of Eq. (3.25) and Eq. (3.20) suggests that one construct the following “hybrid list” for the source and solution vectors:

$$\begin{aligned} w^{(i)} &= \left\{ \frac{v^{(1)}}{\lambda_1}, \dots, \frac{v^{(N_{ev})}}{\lambda_{N_{ev}}}, \eta^{(1)}, \dots, \eta^{(N_{dil})} \right\} \\ u^{(i)} &= \left\{ v^{(1)}, \dots, v^{(N_{ev})}, \psi^{(1)}, \dots, \psi^{(N_{dil})} \right\} \end{aligned} \quad (3.34)$$

where the indices run over  $N_{HL} = N_{ev} + N_{dil}$  elements. The unbiased, variance reduced estimate of the all-to-all quark propagator (for a single diluted random noise vector) is then given by

$$\sum_{i=1}^{N_{HL}} u^{(i)}(\mathbf{x}, x_4) \otimes w^{(i)}(\mathbf{y}, y_4)^\dagger \gamma_5, \quad (3.35)$$

since  $Q = \gamma_5 M \Rightarrow M^{-1} = Q^{-1} \gamma_5$ .

Using the pion as an example, we can demonstrate how reflection positivity is

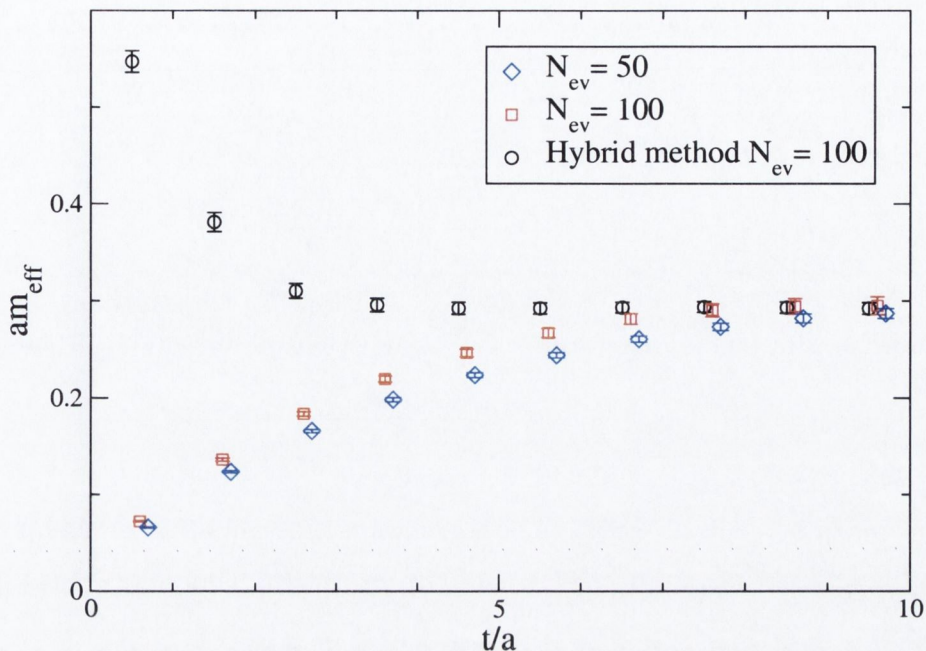


Figure 3-12: The pion effective mass from 50, 100 eigenvectors and from the hybrid method with 100 eigenvectors and a time-diluted noise vector. The parameters of the simulation are given by Table 3.5.

recovered from the truncated propagator using this hybrid method. In Fig. (3-12), we show the effective mass of the pion determined from the truncated propagator and from the hybrid method with a time, spin, colour and space (even-odd) diluted noise vector using the *same* source and sink operators. We see that the truncated propagator yields an effective mass that approaches the asymptotic value from below, which is a manifestation of the violation of reflection positivity. This is corrected by the addition of the diluted noisy propagator.

The use of a truncated eigenvector approach meant that our concerns were no longer with the error in our estimate, since our representation of the eigenvector subspace was exact, but with the question of whether we correctly represented the physics and, if we did, what level of truncation was sufficient to do this. The incorporation of dilution means that we regain all of the physics but at the cost of re-introducing some level of noise.

We perform a quenched simulation using a  $12^3 \times 24$  lattice volume to investigate the error performance of the hybrid method, and compare it to that of a dilution only method on the same configurations. The parameters of the simulation are given in

# gauge configurations	75
Volume	$12^3 \times 24$
$\beta$	5.7
$\kappa_s$	0.1675
$\kappa_t$	0.1675

Table 3.5: Details of the quenched Wilson simulation for the study of error dependence of correlation functions using dilution and hybrid methods for an all-to-all propagator.

Table 3.5, corresponding to a value of  $m_\pi/m_\rho = 0.5$  [40]. In this analysis we study the behaviour of the percentage error of the correlation function at a particular timeslice ( $t = 3$ ) as a function of the dilution level for both the dilution and hybrid methods. The table of dilutions used in this study are given by Table 3.6.

$N_{dil}/NT$	1	2	3	4
Reference	TfSxCxGx	TfSxCxGe	TfSxCfGx	TfSxCxGf
$N_{dil}/NT$	6	8	12	24
Reference	TfSxCfGe	TfSeCxGf	TfSxCfGf	TfSeCfGf

Table 3.6: Table of the dilution levels used in the  $12^3 \times 24$  lattice volume simulations and reference codes (see Table 3.1) for the subspace thinnings from which they are derived.

For the case of the pion, in Fig. (3-13) we note negligible dependence on dilution, particularly in the case of the hybrid method, with the percentage error remaining constant at  $\sim 5\%$  and a consistent determination of this value from the two methods. This is most likely a combination of two factors, firstly that the pion is the least noisy of all particles since its signal to noise ratio have the same temporal dependence whereas this ratio decreases in all other cases [41]. Secondly, in the case of the hybrid method, we observed in the last section the saturation point for eigenmodes was lowest for the pion. It appears that the 100 low-lying eigenmodes of the quark propagator so dominate the correlation function (at this timeslice) that the stochastic correction has no effect on its determination.

For the  $\rho$  meson in Fig. (3-14), in addition to the dilution and hybrid methods, we also plot the optimal  $1/\sqrt{N_R}$  error reduction that would be achieved by increasing

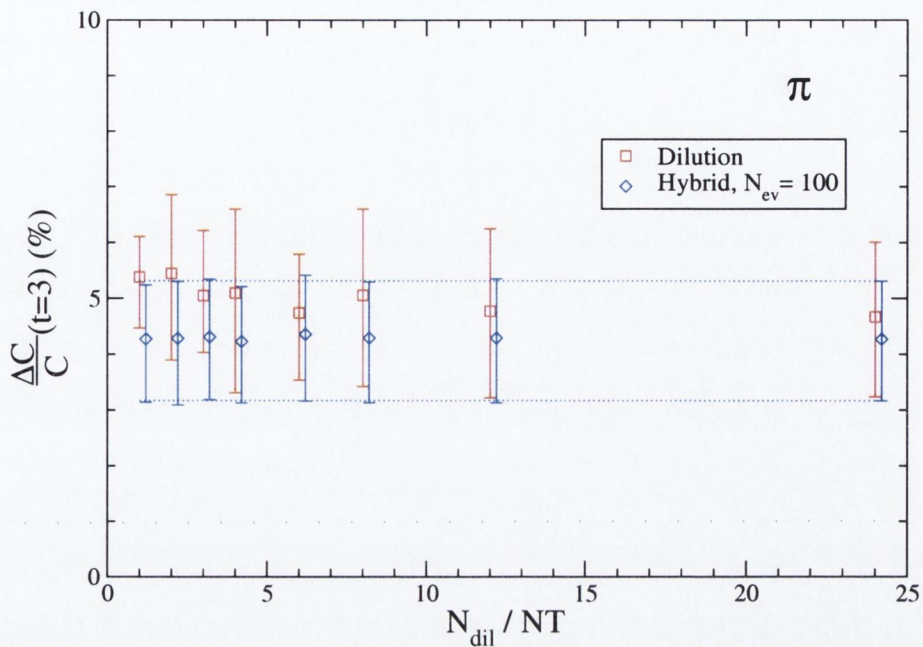


Figure 3-13: The percentage error of the correlation function of the pion at timeslice 3 plotted against the level of dilution,  $\frac{N_{dil}}{NT}$ , for both the hybrid and dilution methods.

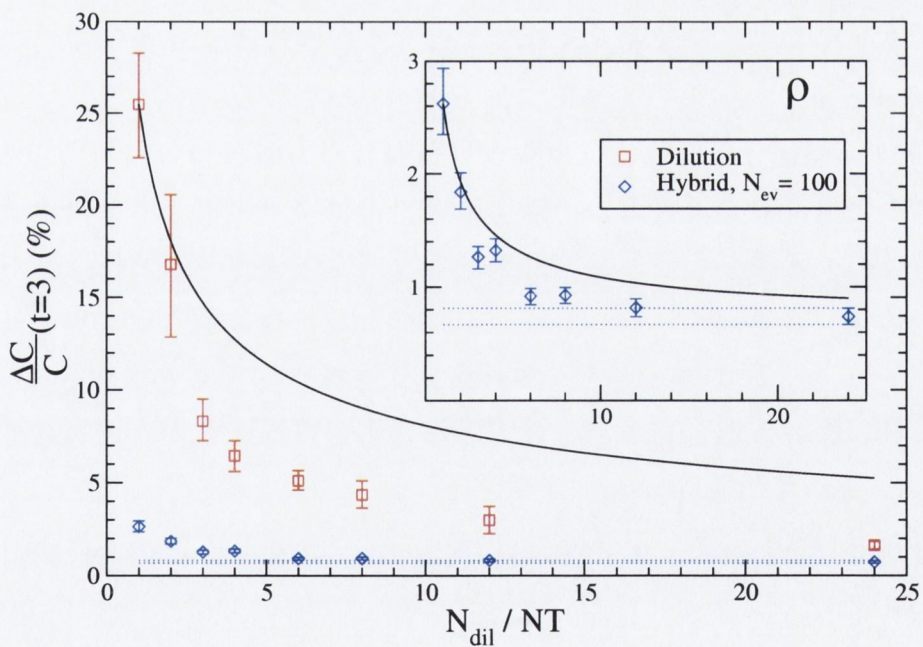


Figure 3-14: The percentage error of the correlation function of the  $\rho$  meson at timeslice 3 plotted against the level of dilution,  $\frac{N_{dil}}{NT}$ , for both the hybrid and dilution methods. The continuous line gives the optimal  $1/\sqrt{N_R}$  error behaviour that one would gain from increasing an ensemble of time-diluted noise vectors. The inset plot is a magnification of the hybrid method behaviour.

the ensemble size,  $N_R$ , of time-diluted noise vectors which is given by

$$\sigma_{N_R}^2 = \frac{\sigma_1^2 - \sigma_\infty^2}{N_R} + \sigma_\infty^2, \quad (3.36)$$

where  $\sigma_\infty$  is the gauge noise, i.e. the statistical uncertainty resulting from having a finite number of gauge configurations. We have assumed that the gauge noise is given by the errors from the hybrid method with our highest dilution level,  $\sigma_g = \sigma_{24}^{hyb}$ . We see that both methods consistently perform better than this behaviour. The most notable feature is the dramatic reduction in percentage error upon the use of the 100 eigenmodes in the hybrid method. Only the highest levels of the dilution method are comparable to the lowest levels in the hybrid method. This feature is so pronounced that the error dependence is difficult to determine on the scale induced by the dilution method. For this reason we also include an inset plot of the hybrid method adjusted to its own scale. The reduction in percentage error is still superior to that obtained by additional statistics in almost all cases. However, the additional computational cost of dilutions greater than colour and spin even/odd (at  $N_{dil}/NT = 6$ ) does not appear to justify the small decreases in the percentage error at these values. We note that it appears that a 1% error level has been achieved by the hybrid method for this case.

The behaviour of the  $1^{++}$  meson in Fig. (3-15) is broadly similar to that of the  $\rho$  meson. The percentage errors in this case are far greater however, and large levels of dilution are required to achieve errors  $\sim 5\%$  level with the dilution only method. For the hybrid method we achieve errors at the  $\sim 10\%$  level at the lowest dilution level and errors of  $< 2\%$  at  $N_{dil}/NT = 6$ .

In general we observe a dramatic reduction in the noise of correlation functions determined using the hybrid method for estimation of the all-to-all quark propagator at low quark masses. To illustrate the increased accuracy that this method allows over the more traditional point-to-all method, we study the behaviour of the effective masses of the pion and  $\rho$  mesons determined from both the point-to-all and hybrid method, see Fig. (3-16), on the same number of configurations. In the case of P-waves (as well as hybrids, and of course isoscalar mesons) all-to-all propagators may

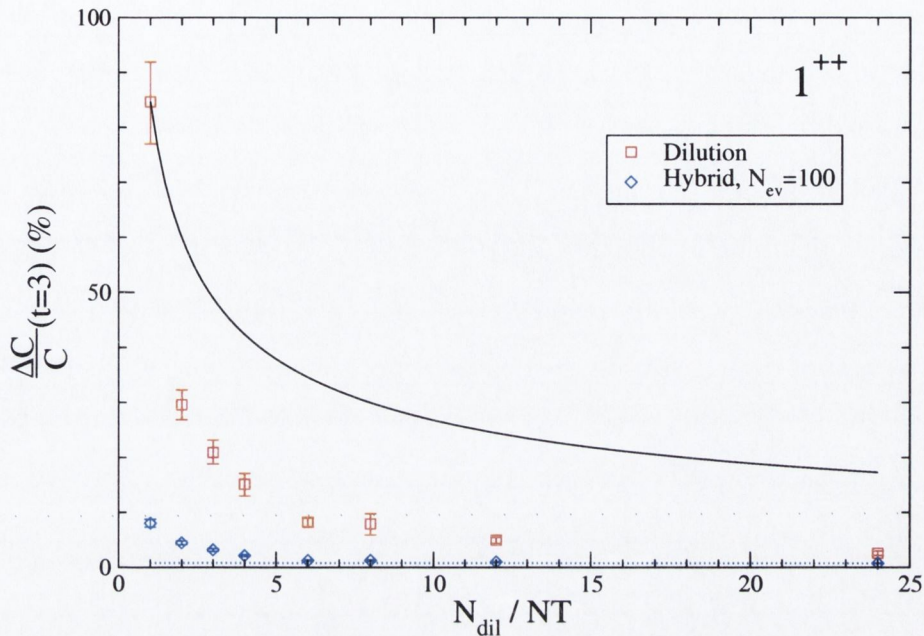


Figure 3-15: The percentage error of the correlation function of the  $1^{++}$  meson at timeslice 3 plotted against the level of dilution,  $\frac{N_{dil}}{NT}$ , for both the hybrid and dilution methods. The continuous line gives the optimal  $1/\sqrt{N_R}$  error behaviour that one would gain from increasing an ensemble of time-diluted noise vectors.

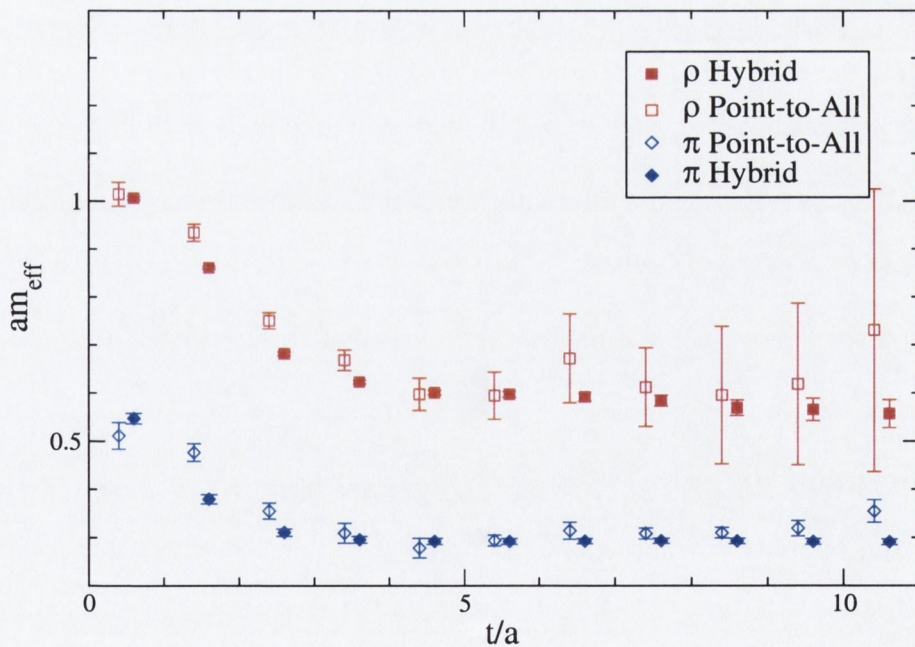


Figure 3-16: The pion and  $\rho$  meson effective masses as determined from a point-to-all propagator method and an all-to-all propagator estimated by the hybrid method approach.

be the only way of obtaining acceptable signal at all. The open symbols are the effective masses determined from the point-to-all method and the closed are those of the hybrid method.

For the pion, since it has the highest signal to noise ratio at large temporal distance, the behaviour of the two methods is broadly similar. The errors from the hybrid are, however, lower by a factor of 2 or more than those of the point-to-all method. At the largest temporal spacing we observe a marked improvement of the hybrid over the point-to-all method. The effective masses determined from both these methods are consistent and have similar confidence levels. The improved signal for the pion does not fully justify the extra computational expense that such a large level of dilution would require.

The behaviour in the case of the  $\rho$  meson is entirely different however. In the point-to-all case the error on the effective mass increases greatly in magnitude with increasing temporal separation. Comparing this to the behaviour of the pion in the point-to-all case, we see this as a manifestation of the point, alluded to earlier, that the noise for all mesons decreases as  $\exp(-M_\pi t)$  while the signal decreases as  $\exp(-Mt)$ . Consequently for all states for which  $M > M_\pi$ , the errors will increase with  $t$  [41].

This is only mildly seen in the hybrid method case however, where the errors increase only slowly in magnitude with increasing temporal separation. The ability to choose a plateau region is greatly improved in the hybrid case with the confidence level of the effective mass determined from this graph vastly superior to that of its point-to-all counterpart.

In general, the hybrid method for estimation of the all-to-all quark propagator allows us to expand our operator basis and greatly improve on the results obtained from existing operators, where these operators give noisy results using a point-to-all method.

# Chapter 4

## Correlation Functions

As discussed previously, in field theory results for physical observables are obtained by calculating expectation values. In the path integral approach these expectation values correspond to time-ordered correlation functions. For all-to-all propagators, we saw that a general isovector two-point correlation function for the creation of a particle at timeslice  $t$  with the operator  $\Gamma_A$  and its annihilation at timeslice  $t + \Delta t$  with the operator  $\Gamma_B$  was given by Eq. (3.11),

$$C^{BA}(\mathbf{p}, \Delta t) = -\frac{1}{L^3 T} \sum_{\mathbf{x}, \mathbf{y}, t} \langle \text{Tr}(S_{F2}(\mathbf{y}, t; \mathbf{x}, t + \Delta t) \Gamma^B(\mathbf{p}) S_{F1}(\mathbf{x}, t + \Delta t; \mathbf{y}, t) \Gamma^A(\mathbf{p})) \rangle, \quad (4.1)$$

where we incorporate phases for momentum projections into the definition of the operators  $\Gamma_A$  and  $\Gamma_B$ .

We also saw that  $C(t) \sim e^{-mt}$  for large  $t$ , which led us to the definition of an effective mass  $m_{eff}(t) = \log(C(t)/C(t+1))$ . An example of an effective mass plot can be seen in Fig. (3-16). The convergence of an effective mass plot to its asymptotic value,  $m$ , can be from above or below depending on the choice of operators  $\Gamma_A$  and  $\Gamma_B$ . Only for  $\Gamma_A = \Gamma_B^\dagger$  is the correlation function positive definite and the convergence is monotonic and from above. For  $\Gamma_A \neq \Gamma_B^\dagger$ , the convergence depends on subtle cancellations between contributions of various states and cannot be guaranteed to be either monotonic or from above. For Fig. (3-16), we have  $\Gamma_A = \Gamma_B^\dagger$  for both the  $\pi$  and  $\rho$  mesons, as we can see the contribution of excited states is most obvious at small  $t$ .

In the *plateau* region at larger  $t$ , one assumes that, within numerical precision, only the lowest state contribution is significant and it is possible to extract  $m$  from this region.

The location in  $t$  of the onset and the length of the plateau region depend on the interpolating operators used. It is also possible to lessen the contribution of excited states by the use of *smearing* techniques [43] which induce an earlier onset of the effective mass plateau region. Smearing operators can be incorporated into our definition of  $\Gamma_A$  and  $\Gamma_B$ . One could also extract the masses of higher resonances by the use of the *variational* approach [42].

We shall employ both of these techniques in our exploratory study of meson spectroscopy using the variant of the ARIA action detailed in Section 2.3.1 with the hybrid all-to-all propagator technique described in Section 3.5.

## 4.1 Meson Operators

In Section 3.5 we saw that using the hybrid technique we may estimate the all-to-all quark propagator  $S_F(\mathbf{x}, x_4; \mathbf{y}, y_4)$  by

$$\sum_{i=1}^{N_{HL}} u^{(i)}(\mathbf{x}, x_4) \otimes w^{(i)}(\mathbf{y}, y_4)^\dagger \gamma_5,$$

suppressing colour and spin indices. The hybrid lists  $w^{(i)}$  and  $u^{(i)}$  are given by

$$\begin{aligned} w^{(i)} &= \left\{ \frac{v^{(1)}}{\lambda_1}, \dots, \frac{v^{(N_{ev})}}{\lambda_{N_{ev}}}, \eta^{(1)}, \dots, \eta^{(N_{dil})} \right\} \\ u^{(i)} &= \left\{ v^{(1)}, \dots, v^{(N_{ev})}, \psi^{(1)}, \dots, \psi^{(N_{dil})} \right\}, \end{aligned}$$

where  $v^{(i)}$  and  $\lambda_i$  are the (low-lying) eigenmodes of the hermitian Dirac quark matrix  $\gamma_5 M$ ,  $\eta^{(i)}$  are (diluted)  $Z(4)$  noise vectors and  $\psi^{(i)}$  are solutions to  $M\psi^{(i)} = \gamma_5(I - P_0)\eta^{(i)}$  where  $P_0 = \sum_{j=1}^{N_{ev}} v^{(j)} \otimes v^{(j)\dagger}$ .

Using this estimation, the correlation function of Eq. (4.1) may be written in

terms of the hybrid lists  $w^{(i)}$  and  $u^{(i)}$ ,

$$C^{BA}(\mathbf{p}, \Delta t) = -\frac{1}{L^3 T} \sum_{i,j,t} \langle w_{[2]}^{(i)}(t + \Delta t), \gamma_5 \Gamma^B(\mathbf{p}) u_{[1]}^{(j)}(t + \Delta t) \rangle \langle w_{[1]}^{(j)}(t), \gamma_5 \Gamma^A(\mathbf{p}) u_{[2]}^{(i)}(t) \rangle \quad (4.2)$$

where the inner product  $\langle \cdot, \cdot \rangle$  has been defined in Eq. (3.21) and we have one set of hybrid lists for each of the quark propagators in our correlation function. We may write this in terms of *meson operators* defined by

$$\mathcal{O}_{[r,s]}^{(i,j)A}(\mathbf{p}, t) \equiv \langle w_{[r]}^{(i)}(t), \gamma_5 \Gamma^A(\mathbf{p}) u_{[s]}^{(j)}(t) \rangle. \quad (4.3)$$

Incorporating the phase for the momentum projection into our definition of the operator  $\Gamma^A(\mathbf{p})$  ( $\Gamma^B(\mathbf{p})$ ) allows us to think of the meson operator matrix  $\mathcal{O}_{[1,2]}^{(i,j)A}(\mathbf{p}, t)$  ( $\mathcal{O}_{[2,1]}^{(j,i)B}(\mathbf{p}, t + \Delta t)$ ) as a meson creation (annihilation) operator for a state with definite momentum  $\mathbf{p}$  at timeslice  $t$  ( $t + \Delta t$ ) using the quark propagator estimates for  $S_{F1}$  and  $S_{F2}$ .

The correlation function is then simply constructed as a product of a source meson operator,  $\mathcal{O}_{[1,2]}^{(i,j)A}$ , and a sink meson operator,  $\mathcal{O}_{[2,1]}^{(j,i)B}$ , on different timeslices,

$$C^{BA}(\mathbf{p}, \Delta t) = -\frac{1}{L^3 T} \sum_{i,j,t} \mathcal{O}_{[2,1]}^{(j,i)B}(\mathbf{p}, t + \Delta t) \mathcal{O}_{[1,2]}^{(i,j)A}(\mathbf{p}, t). \quad (4.4)$$

Defining and constructing meson operators in this way also allows a straightforward implementation of the noise-recycling technique outlined in Section 3.3.3. For  $N_R$  estimates of the quark propagator  $S_F$ , a degenerate quark mass correlation function is given by,

$$C^{BA}(\mathbf{p}, \Delta t) = -\frac{1}{L^3 T N_R (N_R - 1)} \sum_{s=1, r < s}^{N_R} \sum_{i,j,t} \mathcal{O}_{[s,r]}^{(j,i)B}(\mathbf{p}, t + \Delta t) \mathcal{O}_{[r,s]}^{(i,j)A}(\mathbf{p}, t). \quad (4.5)$$

The use of meson operators is not restricted and can, for example, be used to

construct particle decay correlations functions,

$$C^{CBA}(\Delta t) = \sum_t \sum_{i,j,k} \mathcal{O}_{[1,3]}^{(i,k)C}(-\mathbf{p}, t + \Delta t) \mathcal{O}_{[3,2]}^{(k,j)B}(\mathbf{p}, t + \Delta t) \mathcal{O}_{[2,1]}^{(j,i)A}(\mathbf{0}, t). \quad (4.6)$$

where we neglect the normalisation constant.

The benefit of the construction of meson operators is that they allow access to additional statistics and physics without the need to repeat a large part of the analysis. We have shown this for noise-recycling and the case of a particle decay correlation function but they also have applications to decay constants and form factors.

## 4.2 Mesonic Interpolating Operators

If we extract the momentum projection from the definition of  $\Gamma_A$  ( $\Gamma_B$ ) in Eq. (4.4), a meson operator may be written as

$$\mathcal{O}_{[r,s]}^{(i,j)A}(\mathbf{p}, t) = \sum_{\mathbf{x}} e^{i\mathbf{p}\cdot\mathbf{x}} \mathcal{O}_{[r,s]}^{(i,j)A}(\mathbf{x}, t), \quad (4.7)$$

where

$$\mathcal{O}_{[r,s]}^{(i,j)A}(\mathbf{x}, t) = \text{Tr}(w_{[r]}^{(i)}(\mathbf{x}, t)^\dagger \gamma_5 \Gamma^A u_{[s]}^{(j)}(\mathbf{x}, t)), \quad (4.8)$$

the trace is over the suppressed spin and colour indices and  $n = +1$  ( $n = -1$ ) for the creation (annihilation) operator  $\Gamma_A$  ( $\Gamma_B$ ). The factor of  $\gamma_5$  comes from our use of the hermitian quark propagator  $\gamma_5 M$  in the construction of our hybrid lists. Using this definition, the meson interpolating operators  $\Gamma_A$  and  $\Gamma_B$  can denote any local or spatially extended interpolating operator. This greatly increases the basis of potential operators that can be used in the application of the variational technique (detailed in Section 4.4). It also allows the straightforward incorporation of source and/or sink smearing operators.

Here, we consider the construction of bosonic operators that contain a quark and an antiquark. The general form of the operator we consider is

$$\bar{\psi}(\mathbf{x}) F(P) \Gamma \psi(\mathbf{x}) \quad (4.9)$$

where  $\Gamma$  is one of the sixteen independent  $\gamma$ -matrix combinations and  $F(P)$  is a some path dependent operator that spatially separates the two quark fields, joining them by a product of gauge links along the particular path  $P$ . This is a gauge invariant construction. We shall construct operators with a given set of quantum numbers by taking linear combinations with different paths and different expressions for  $\Gamma$ , as detailed in [44] and reproduced here. Operators constructed in this way are directly applicable in Eq. (4.8).

In the continuum the hadrons are classified according to their total angular momentum  $J$  and parity  $P$ . For mass degenerate quark and antiquark, we also classify mesons by their charge conjugation,  $C$ . For the case where there is no path between the quark and antiquark, and we have a local quark bilinear operator, the  $\gamma$ -matrix combinations have the  $J^{PC}$  values listed in Table 4.1.

$\Gamma$	$J^{PC}$	Name
1	$0^{++}$	$\delta$
$\gamma_4$	$0^{+-}$	<i>exotic</i>
$\vec{\gamma}$	$1^{--}$	$\rho$
$\vec{\gamma}\gamma_4$	$1^{--}$	$\rho$
$\gamma_5$	$0^{-+}$	$\pi$
$\gamma_5\gamma_4$	$0^{-+}$	$\pi$
$\gamma_i\gamma_j$	$1^{+-}$	B
$\gamma_5\vec{\gamma}$	$1^{++}$	$A_1$

Table 4.1: The 16 independent  $\gamma$ -matrix bilinears and their continuum  $J^{PC}$  values. The names for the isovector non-strange mesons with those quantum numbers is also included.

A full study of mesons with orbital angular momentum needs non-local operators. The general case will involve discussion of the properties of the path under rotations reflections and charge conjugation. Since the spinor structure is in a fixed basis, it is sufficient to consider separately the transformation properties of the path  $P$  connecting the quark fields and combine the result with that of Table 4.1 for quark bilinears.

The group of rotations and inversions for a three dimensional spatial lattice is the cubic group  $O_h$ . Thus this is the appropriate classification group for bosonic transfer

matrix eigenstates with momentum zero. For the case of non-zero momentum, not discussed here, the space group needs to be used instead.

The representations of  $O_h$  are labeled by their parity  $P$  and charge conjugation  $C$  in the same way as bosonic representations of the  $SU(2)$  rotation group appropriate to the continuum formulation. Thus the essential difference between the lattice eigenstates and continuum eigenstates lies in the ‘spin’.

Whereas a state of spin  $J$  has  $2J+1$  spin components which are degenerate in mass and form a  $2J + 1$  dimensional representation in the continuum, for  $O_h$  there exist only 1,2 and 3-dimensional representations. The 1-dimensional representations are labeled  $A_1$  and  $A_2$ , there is a 2-dimensional  $E$  representation and the 3-dimensional representations are  $T_1$  and  $T_2$ . The relationship of these representations to those of  $SU(2)$  can be derived by restricting the  $SU(2)$  representations to the rotations allowed by cubic symmetry and classifying them under  $O_h$ . This process is called *subducing* and yields the results tabulated (to  $J = 3$ ) in Table 4.2.

$J = 0$	$A_1$
$J = 1$	$T_1$
$J = 2$	$ET_2$
$J = 3$	$A_2T_1T_2$

Table 4.2: Result of subducing the  $SU(2)$  rotation group representations to those appropriate to  $O_h$ .

Optimal signal to noise comes from constructing operators on a lattice which create states of given  $O_h$  representation. Here the lattice constructs are the paths  $P$  between the quark fields along the links of the lattice. These paths must be classified according to the representations of the cubic group  $O_h$ . The projection table of Ref. [45] gives the relevant combination of paths with different cubic rotations for each representation.

As well as the spatial path  $P$ , the mesonic operator will have a spin component coming from the quark spinors. On a lattice, where the spatial symmetry is  $O_h$ , the only change in the classification of these bilinears is that the singlets ( $J = 0$ ) become  $A_1$  while the triplets ( $J = 1$ ) become  $T_1$ . We need to combine the  $O_h$  representation of this quark bilinear with that of the spatial path  $P$ . The combined operator will

lie in a representation given by the Clebsch-Gordan decomposition of the product of representations. When the quark bilinear is in the  $A_1$  representation the final representation is just that of the spatial path. For the  $T_1$  representation of quark bilinears we need the decomposition in Table 4.3.

$$\begin{aligned}
T_1 \otimes A_1 &= T_1 \\
T_1 \otimes A_2 &= T_2 \\
T_1 \otimes E &= T_1 \oplus T_2 \\
T_1 \otimes T_1 &= A_1 \oplus T_1 \oplus T_2 \oplus E \\
T_1 \otimes T_2 &= A_2 \oplus T_1 \oplus T_2 \oplus E
\end{aligned}$$

Table 4.3: Clebsch-Gordan decomposition of the product of  $T_1$  with the  $O_h$  representations

Since the general path with no symmetry will contribute to all  $O_h$  representations in principle, one can create operators with all quantum numbers. We shall discuss states that can be constructed from more symmetric paths: straight, L-shaped and U-shaped.

The simplest case is to consider a straight line joining quark to antiquark along a lattice axis, which gives the  $A_1$ ,  $T_1$  and  $E$  representations in Table 4.4 where

$$p_j \phi(\mathbf{x}) = U_j(\mathbf{x})\phi(\mathbf{x} + \mathbf{j}) - U_j^\dagger(\mathbf{x} - \mathbf{j})\phi(\mathbf{x} - \mathbf{j}) \quad (4.10)$$

$$\text{and } s_j \phi(\mathbf{x}) = U_j(\mathbf{x})\phi(\mathbf{x} + \mathbf{j}) + U_j^\dagger(\mathbf{x} - \mathbf{j})\phi(\mathbf{x} - \mathbf{j}) \quad (4.11)$$

and  $j = 1, 2, 3$  denote the spatial axes  $x, y, z$ . Conventional normalisation factors are omitted for simplicity. These three representations correspond partly to the  $S$ -,  $P$ - and  $D$ -wave orbital excitations of the naive quark model. The path combinations given play the role of spherical harmonics in  $SU(2)$ .

$$\begin{array}{ll}
A_1^{++} & s_1 + s_2 + s_3 \\
T_1^{--} & p_1, p_2, p_3 \\
E^{++} & s_1 - s_2, 2s_3 - s_1 - s_2
\end{array}$$

Table 4.4:  $O_h$  representations given by a straight line path along a lattice axis joining the quark and antiquark.

We consider the states that can be constructed by combining these path repre-

representations with the quark bilinears. The combinations of the straight-path representations with the bilinears that we employ are given in Table 4.5. The lowest  $J$ -value corresponding to the  $O_h$  representation is also given.

$\bar{q}\Gamma q$	Path	State	Operator	$J^{PC}$
$A_1^{-+}$	$A_1^{++}$	$A_1^{-+}$	$\gamma_5(s_1 + s_2 + s_3)$	$0^{-+}$
$A_1^{-+}$	$T_1^{--}$	$T_1^{+-}$	$\gamma_5\vec{p}$	$1^{+-}$
$T_1^{--}$	$T_1^{--}$	$A_1^{++}$	$\vec{\gamma} \cdot \vec{p}$	$0^{++}$
$T_1^{--}$	$T_1^{--}$	$T_1^{++}$	$\vec{\gamma} \times \vec{p}$	$1^{++}$
$T_1^{--}$	$T_1^{--}$	$T_2^{++}$	$\gamma_k p_i + \gamma_i p_k$	$2^{++}$
$A_1^{-+}$	$E^{++}$	$E^{-+}$	$\gamma_5(s_1 - s_2), \gamma_5(s_3 - s_1 - s_2)$	$2^{-+}$

Table 4.5:  $O_h$  representations given by some of the combinations of the quark bilinears with straight-path representations in Table 4.4.

To access the  $D$ -wave meson with  $J^{PC} = 3^{--}$  we need an operator in the  $A_2^{-}$  representation. This is accessible through the use of a ‘straight diagonal’ path from quark to antiquark. Such a path is the sum of two L-shaped paths going to the far corner of a square via the sides. We use the notation  $[ij]$ ,  $[i\bar{j}]$ ,  $[\bar{i}j]$  to describe such a path to the  $(i, j)$ ,  $(i, -j)$ ,  $(-i, -j)$  diagonal corner from the origin,

$$\begin{aligned}
[ij]\phi(\mathbf{x}) &= \left( U_i(\mathbf{x})U_j(\mathbf{x} + \mathbf{i}) + U_j(\mathbf{x})U_i(\mathbf{x} + \mathbf{j}) \right) \phi(\mathbf{x} + \mathbf{i} + \mathbf{j}), \\
[i\bar{j}]\phi(\mathbf{x}) &= \left( U_i(\mathbf{x})U_j^\dagger(\mathbf{x} + \mathbf{i} - \mathbf{j}) + U_j^\dagger(\mathbf{x} - \mathbf{j})U_i(\mathbf{x} - \mathbf{j}) \right) \phi(\mathbf{x} + \mathbf{i} - \mathbf{j}), \\
[\bar{i}j]\phi(\mathbf{x}) &= \left( U_i^\dagger(\mathbf{x} - \mathbf{i})U_j^\dagger(\mathbf{x} - \mathbf{i} - \mathbf{j}) + U_j^\dagger(\mathbf{x} - \mathbf{j})U_i^\dagger(\mathbf{x} - \mathbf{i} - \mathbf{j}) \right) \phi(\mathbf{x} - \mathbf{i} - \mathbf{j}).
\end{aligned}$$

The appropriate combination of these for the  $T_2^{++}$  spatial operator is,

$$t_k = [ij] - [i\bar{j}] - [j\bar{i}] + [\bar{j}i], \quad (4.12)$$

with  $i, j, k$  cyclic. Combining this with the  $T_1^{--}$  quark bilinear as  $\vec{\gamma} \cdot \vec{t}$  gives an  $A_2^{-}$   $O_h$  representation state with corresponding  $J$ -value  $3^{--}$ .

### 4.2.1 Hybrid Mesons

Hybrid mesons are defined as having the gluonic field excited in a non-trivial way. One of the consequences of these excited gluonic modes is that hybrid mesons can

have  $J^{PC}$  values not allowed to mesons which have their gluonic degrees of freedom in the ground state. We are interested in constructing mesonic operators with that have *exotic* quantum numbers which are not present in the naive quark model, such as the  $J^{PC} = 1^{-+}$  state.

If we take the picture of a hybrid state with exotic quantum numbers as arising from gluonic excitations then we expect that operators with no gluonic excitation are not particularly promising in forming an exotic representation in the sense that the coupling may be very small and hence swamped by noise in practice. A direct way to create exotic states is to use a path which is not straight. We employ the use of a U-shaped ('staple') path.

Static quark results [46] show that the lowest energy hybrid states come from an operator which is the difference of staple paths from quark to antiquark of the form  $\square - \sqcup$ . We obtain a  $T_1^{+-}$  representation path by

$$u_k = ij - ji - \bar{i}j + \bar{j}i \quad (4.13)$$

where we use the staple path combinations

$$\begin{aligned} ij\phi(\mathbf{x}) &= \left( U_j(\mathbf{x})U_i(\mathbf{x}+\mathbf{j})U_j^\dagger(\mathbf{x}+\mathbf{i}) - U_j^\dagger(\mathbf{x}-\mathbf{j})U_i(\mathbf{x}-\mathbf{j})U_j(\mathbf{x}+\mathbf{i}-\mathbf{j}) \right) \phi(\mathbf{x}+\mathbf{i}), \\ \bar{i}j\phi(\mathbf{x}) &= \left( U_j(\mathbf{x})U_i^\dagger(\mathbf{x}-\mathbf{i}+\mathbf{j})U_j^\dagger(\mathbf{x}-\mathbf{i}) - U_j^\dagger(\mathbf{x}-\mathbf{j})U_i^\dagger(\mathbf{x}-\mathbf{i}-\mathbf{j})U_j(\mathbf{x}-\mathbf{i}-\mathbf{j}) \right) \phi(\mathbf{x}-\mathbf{i}), \end{aligned}$$

and  $i, j, k$  are cyclic. Combining this with the  $T_1^{--}$  quark bilinear, we obtain the  $T_1^{-+}$  representation operator  $\vec{\gamma} \times \vec{u}$  which has corresponding  $J^{PC} = 1^{-+}$ .  $\vec{u}$  can also be combined with the  $\gamma_5$  bilinear to form a the  $T_1^{--}$  representation operator  $\gamma_5 \vec{u}$ , corresponding to the  $J^{PC} = 1^{--}$  state.

We can also study gluonic excitations where the quarks are not separated and the gluonic path is closed. The simplest choice is a square path with one corner at the quark and antiquark source. We can construct the chromomagnetic field from such paths,

$$B_k = \frac{\{ij\} - \{ji\}}{2i} - \frac{1}{N_f} \text{Tr} \left( \frac{\{ij\} - \{ji\}}{2i} \right) \quad (4.14)$$

where

$$\begin{aligned}
\{ij\}\phi(\mathbf{x}) = & \left( U_i(\mathbf{x})U_j(\mathbf{x} + \mathbf{i})U_i^\dagger(\mathbf{x} + \mathbf{j})U_j^\dagger(\mathbf{x}) \right. \\
& + U_j^\dagger(\mathbf{x} - \mathbf{j})U_i^\dagger(\mathbf{x} + \mathbf{i} - \mathbf{j})U_j(\mathbf{x} + \mathbf{i} - \mathbf{j})U_i^\dagger(\mathbf{x}) \\
& + U_i^\dagger(\mathbf{x} - \mathbf{i})U_j^\dagger(\mathbf{x} - \mathbf{i} - \mathbf{j})U_i(\mathbf{x} - \mathbf{i} - \mathbf{j})U_j(\mathbf{x} - \mathbf{j}) \\
& \left. + U_j(\mathbf{x})U_i^\dagger(\mathbf{x} - \mathbf{i} + \mathbf{j})U_j^\dagger(\mathbf{x} - \mathbf{i})U_i(\mathbf{x} - \mathbf{i}) \right) \phi(\mathbf{x}), \quad (4.15)
\end{aligned}$$

and  $i, j, k$  are cyclic. This also gives a  $T_1^{+-}$  representation path and we can again form the  $J^{PC} = 1^{-+}$  state from  $\vec{\gamma} \times \vec{B}$  and the  $J^{PC} = 1^{--}$  state from  $\gamma_5 \vec{B}$ .

The implementation of all of these operators using our hybrid method estimation of the quark propagator is identical to their implementation in  $\bar{\psi}(\mathbf{x})F(P)\Gamma\psi(\mathbf{x})$ , i.e., we substitute directly

$$\Gamma^A = (F^A(P)\Gamma^A)^\dagger \quad \text{and} \quad \Gamma^B = F^B(P)\Gamma^B$$

for the creation (annihilation) operator  $\Gamma^A$  ( $\Gamma^B$ ) in Eq. (4.4). The complete list of operators used and the  $J$  values corresponding to their  $O_h$  representations are listed in Table 4.6. All of these operators have definite hermiticity and can be applied identically at source and sink.

$J^{PC}$	Operator(s)
$1^{--}$	$\vec{\gamma}, \gamma_5 \vec{u}, \gamma_5 \vec{B}$
$0^{-+}$	$\gamma_5, \gamma_5(s_1 + s_2 + s_3)$
$0^{++}$	$1, \vec{\gamma} \cdot \vec{p}$
$1^{++}$	$\gamma_5 \vec{\gamma}, \vec{\gamma} \times \vec{p}$
$2^{++}$	$\gamma_k p_i + \gamma_i p_k$
$1^{+-}$	$\gamma_i \gamma_j, \gamma_5 \vec{p}$
$2^{-+}$	$\gamma_5(s_1 - s_2), \gamma_5(s_3 - s_1 - s_2)$
$3^{--}$	$\vec{\gamma} \cdot \vec{t}$
$1^{-+}$	$\vec{\gamma} \times \vec{u}, \vec{\gamma} \times \vec{B}$

Table 4.6: Interpolating operators used and the  $J$  values corresponding to their  $O_h$  representations.

### 4.3 Smearing

We require operators which couple strongly to the low-lying states in the hadron spectrum and weakly to the high-lying states. The main idea of *smearing* quark fields [47, 48] is to use extended source and sink fields to dampen out couplings to the short-wavelength, high-momentum modes. Gaussian suppression of the high momentum modes is perhaps the simplest method one can use. Since a Gaussian in momentum space remains a Gaussian in coordinate space, we employ a gauge-covariant smearing scheme [43] in which the smeared quark field at a given site is defined as a Gaussian weighted average of the surrounding sites on the same timeslice:

$$\tilde{\psi}(\tilde{\mathbf{x}}) \sim \int d^3r e^{-\frac{\tilde{\mathbf{r}}^2}{4\sigma_s^2}} \psi(\tilde{\mathbf{x}} + \tilde{\mathbf{r}}) \sim e^{+\frac{\sigma_s^2 \Delta}{4}} \psi(\tilde{\mathbf{x}}) \quad (4.16)$$

In practice this expression is approximated by

$$\tilde{\psi}(\mathbf{x}) = \left( 1 + \frac{\sigma_s^2}{4n_\sigma} \Delta \right)^{n_\sigma} \psi(\mathbf{x}) \quad (4.17)$$

$$\text{where } \Delta\psi(\mathbf{x}) = \sum_{k=\pm 1, \pm 2, \pm 3} \left( U_k(\mathbf{x}) \psi(\mathbf{x} + \hat{\mathbf{k}}) - \psi(\mathbf{x}) \right), \quad (4.18)$$

and  $\Delta$  denotes the three dimensional gauge-covariant Laplacian. The two parameters to tune in this smearing procedure are the smearing radius  $\sigma_s$  and the integer number of iterations  $n_\sigma$ .

In a point-to-all propagator approach it is not possible to easily adjust the smearing parameters at the point-source since we have information on the quark field only at a single point. The use of an all-to-all propagator technique allows us to optimise the smearing parameters of the quark fields at both the source and sink without the need to perform any additional conjugate gradient inversions.

For local hadron operators it is well known that the use of locally smeared operators has proven crucial. For extended operators, one expects the quark field smearing to be equally important, but the relevance and interplay of the gauge field smearing is less well known. In Section 2.1.3, we detailed the analytic smearing scheme, known as stout-link smearing [9], which we use. While a systematic study of the relation-

ship of the two is not undertaken here, a study of these smearing schemes for the case of extended baryon operators has been undertaken in [49]. This study indicates that quark-field smearing dramatically diminishes couplings to the short wavelength modes, whereas stout-link smearing reduces the noise in operators with displaced quarks.

## 4.4 Variational Approach

The most appealing approach to obtain ground and higher state resonances is to apply *variational* methods. Firstly, we compute a matrix of correlation functions  $C^{AB}(t)$  in Eq. (4.4) where the operators  $\mathcal{O}^I$  form a basis of operators of definite quantum numbers of size  $r$ . For every  $t \geq 0$ , if  $\lambda_\alpha(t)$  are the eigenvalues of this correlation matrix ordered such that  $\lambda_1 \geq \lambda_2 \geq \dots \geq \lambda_r$ , then for all  $\alpha = 1, \dots, A$  (where  $A$  is the number of pure 2-particle states) we have

$$\lambda_\alpha(t) \underset{t \rightarrow \infty}{\approx} c_\alpha e^{-tE_\alpha} \left[ 1 + O(e^{-t\Delta E_\alpha}) \right], \quad (4.19)$$

where  $c_\alpha > 0$ ,  $E_\alpha$  are the ordered energy levels and  $\Delta E_\alpha$  is the distance of  $E_\alpha$  from other spectral values  $E_\beta$  [42].

The error term in Eq. (4.19) is not necessarily small however since correlation functions cannot, in general, be determined accurately for large  $t$ . If we consider instead the generalised eigenvalue problem

$$C(t)\phi = \lambda(t, t_0)C(t_0)\phi, \quad (4.20)$$

where  $t_0$  is small and fixed, the eigenvalues again satisfy Eq. (4.19), however the amplitudes  $c_\alpha$  are different. Using an ordered spectral decomposition of  $C(t)$ , we can expect the truncation to the  $r$  highest-lying modes,

$$C_0^{BA}(t) = \sum_{\alpha=1}^r v_\alpha^{B*} v_\alpha^A e^{-tE_\alpha}, \quad (4.21)$$

to approximate  $C(t)$  rather well. The spectrum of eigenvalues,  $\lambda_\alpha^0(t, t_0)$ , of the associated generalised eigenvalue problem is *exactly* given by

$$\lambda_\alpha^0(t, t_0) = e^{-(t-t_0)E_\alpha} \quad \text{for all } \alpha = 1, \dots, r. \quad (4.22)$$

We write  $C = C_0 + C_1$  and treat  $C_1$  as a perturbation. The larger eigenvalues, particularly those of interest, should not be strongly affected by this perturbation and they are thus approximately equal to  $\lambda_\alpha^0(t, t_0)$ .

To apply this approximation, we find a basis of eigenvectors  $V(t)$  that diagonalises the transfer matrix  $C(t_0)^{-1}C(t)$  for  $t = t_0 + 1$  for some  $t_0$  close to the source (where the inversion of  $C(t_0)$  does not become numerically unstable). We can then determine the spectrum from the eigenvalues of

$$V(t_0 + 1)^{-1}C(t_0)^{-1}C(t)V(t_0 + 1) \quad (4.23)$$

at subsequent times, since they should exhibit the behaviour of Eq. (4.22).

This method relies on constructing a basis of operators  $\mathcal{O}^I$  that provides a good description of the states of interest. We can construct a fuller variational basis from a combination of the multiple operators for each  $O_h$  representation state (from Table 4.1 and Table 4.6 for example) and from the application of different smearing operators to the quark fields.

## 4.5 Isovector Mesons

In Eq. (4.1), for the special case of the pion, we can have  $\Gamma_A = \Gamma_B = \gamma_5$ . Using the hermiticity property  $S_F(\mathbf{y}, t; \mathbf{x}, t + \Delta t)^\dagger = \gamma_5 S_F(\mathbf{x}, t + \Delta t; \mathbf{y}, t) \gamma_5$ ,  $C^\pi(\Delta t)$  has the maximum value on each configuration. Furthermore, for degenerate up and down quarks,  $S_{F1} = S_{F2}$  which means this correlation is the absolute square of the propagator. Other spin-parity states involve  $\gamma$  matrices, since these have both plus and minus signs the various spinor terms in the trace have cancellations. Also, since the integration measure for QCD is positive, each configuration contributes with the same sign. Thus,  $C^\pi(\Delta t) \geq C^{BA}(\Delta t)$  for all  $\Delta t$ . As we saw earlier, since  $C(t) \sim e^{-mt}$ , this inequality implies that the pion is the lightest meson.

Furthermore, for a state with  $N$  valence quark lines, where  $N = 2(3)$  for mesons (baryons), the errors are controlled by the square of the correlator which has  $2N$  lines. The state of lowest energy in the squared correlator is, therefore, two pions for mesons and three pions for baryons. Thus, while the signal decreases as  $\exp(-mt)$  the noise only decreases as  $\exp(-m_\pi t \times N/2)$ . Consequently, for all states for which  $m > Nm_\pi/2$ , the errors will increase with  $t$ . The only exception to this being the pion, for which the signal and noise have the same  $t$  dependence [41].

As such, the pion is the yard-stick by which we measure the quality of correlation functions, its resolution should determine the limit of accuracy achievable by other correlation functions. We have already seen in Section 2.3.1 that, for the quenched simulation whose parameters are given in Table 3.5, that we achieve roughly identical results for all levels of dilution using the hybrid all-to-all propagator technique for the pion, see Fig. (3-13). Dramatically improved error behaviour with increased dilution was observed for other, heavier, states however (for example see Fig. (3-15)).

In Fig. (4-1), we show the effective mass plots of the pion, rho and P-wave states using the highest level of dilution of Table 3.6 for the quenched Wilson simulation whose parameters are detailed in Table 3.5 [28]. For the pion the behaviour is exactly as expected, with no apparent increase in noise with increasing time. The optimised smearing parameters used here allow an obvious plateau region to form from timeslice 3 onwards.

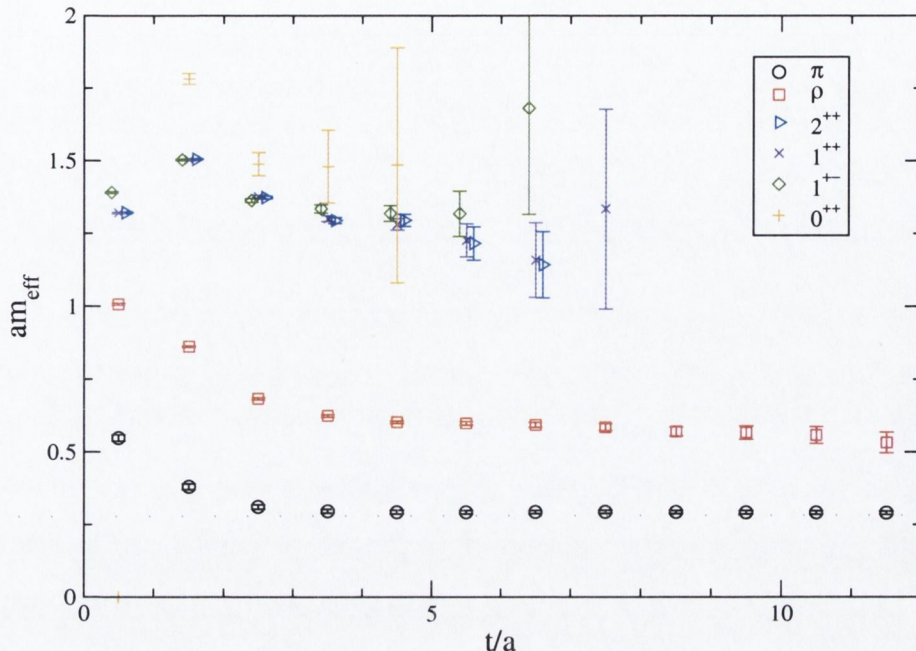


Figure 4-1: Effective masses for isovector mesons with 100 eigenvectors, time, colour, spin and space-even-odd dilution and 75 configurations.

Focusing on the  $\rho$  meson, we can see the formation of a plateau region from timeslice 4 onwards. As expected, due to the higher mass of this meson we observe an increase in statistical noise with increasing temporal extent. This increase remains controlled however, and the a good signal extending to the centre of the lattice at timeslice 12.

The signals for the  $2^{++}$ ,  $1^{++}$  and  $1^{+-}$   $P$ -wave states are degenerate within errors and the signal in all cases is swamped by noise by timeslice 6. Noting from Table 4.6 that the  $P$ -wave states shown here all use extended interpolating operators, we believe these large errors to be due to large fluctuations in the gauge fields from configuration to configuration for the Wilson action.

#### 4.5.1 Dynamical Simulation

While the results of the quenched Wilson simulation show promising signals in traditionally noisy channels, the employment of an improved action in a dynamical anisotropic simulation should prove a more interesting and realistic challenge.

This exploratory study was performed on  $N_f = 2$  dynamical background con-

Number of Gauge Configurations	250	$\beta$	1.522
Volume	$8^3 \times 48$	Bare Quark Anisotropy, $\xi_q$	8.3
Target Anisotropy, $\xi_r = a_s/a_t$	6	Bare Gauge Anisotropy, $\xi_g$	7.44
$a_s$	0.2fm	$a_t m_q$	-0.057

Table 4.7: Run parameters for the dynamical simulation.

figurations. These configurations were generated using the anisotropic gauge action (detailed in Section 2.1.4), a variant of ARIA (Eq. (2.64), where the clover term was set to zero and  $\mu_r$  was set to 1) and stout-link smearing. The bare sea quark mass was set at  $a_t m_o = -0.057$  which corresponded to the strange quark mass in the quenched simulation of the same quark action in Section 2.3.1. The renormalised anisotropy in this simulation was close to six for determinations from both the dispersion relation of the pion and the sideways potential but did require further tuning [54]. The tuning procedure for dynamical lattices has been outlined in Section 2.3.1. The parameters of the simulation are given in Table 4.7. The spatial lattice spacing determined from the static inter-quark potential, and confirmed in a study of the charmonium spectrum on the same background configurations, was found to be approximately 0.2fm ( $a_s^{-1} \sim 1\text{GeV}$ ). With an anisotropy ratio of  $\xi = 6$ , this corresponds to a temporal lattice spacing of 0.033fm ( $a_t^{-1} \sim 6\text{GeV}$ ).

In Fig. (4-2) we plot the spectrum for some of the operators of Table. (4.6). In this plot we observe good signals with controlled error behaviour for all states except the  $1^{-+}$  exotic hybrid state. This simulation proved to be in a relatively small volume, given the lattice spacing and dimension, and it is probably important that a larger volume is used since the wavefunction of the exotic hybrid could be quite large and would be squeezed in the small lattices we use here. A table for the effective masses of these states (calculated using uncorrelated fits), and the operators used to obtain them, is given in Table 4.8.

We use the derivative based operators for all the  $P$ -states ( $1^{++}, 2^{++}, 1^{-+}$ ) except the  $0^{++}$  scalar where the identity operator was seen to produce a much cleaner signal. This is contrary to expectation since in the heavy quark limit the spin components that the identity operator excites decouple, so we would expect a poor overlap with

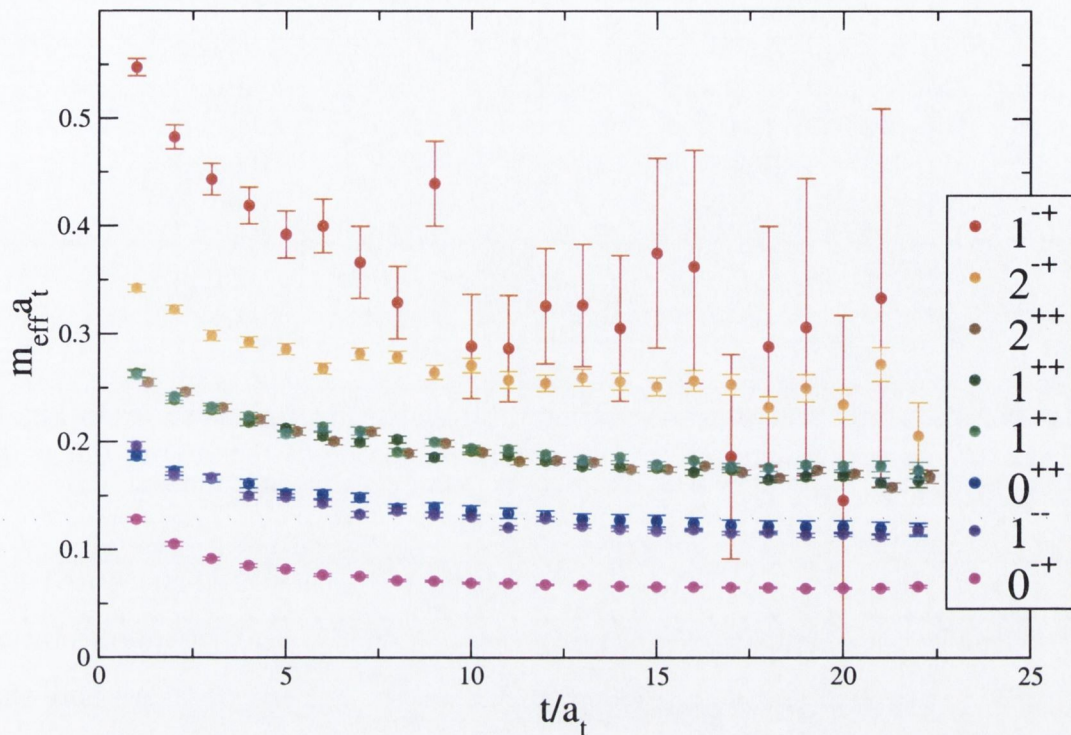


Figure 4-2: Effective masses for isovector mesons with 100 eigenvectors, time and colour dilution and 250 dynamical anisotropic configurations.

the  $0^{++}$  state, even with lighter quarks. Within errors, from Table 4.8 we can see a small splitting between the masses of the  $P$ -states that use extended derivative based operators. This contradicts the information we observe in Fig. (4-2) where there would appear to be an obvious degeneracy between these states. This is due to random noise introduced at each timeslice in the dilution procedure. This noise makes locally measured quantities such as an effective mass fluctuate more than they would with point propagators. These *local fluctuations* are correlated across our ensemble and do not affect the exponential fits [62].

This effect is most notable in the noisiest state, the hybrid  $1^{-+}$ . The effective mass appears extremely noisy and erratic, however we are still able to obtain a fit with low errors and a good  $\chi^2$  over a reasonably large number of lattice sites. The fit corresponds to a mass of  $\sim 1830$  MeV which is in qualitative agreement with that of Ref. [50] who measured the mass of an  $s\bar{s}$   $1^{-+}$  hybrid meson to be  $2100 \pm 120$  MeV.

In Fig. (4-3) we demonstrate a fit for the  $1^{+-}$  and  $1^{++}$   $P$ -states using the variational technique. Although there is some indication of the splitting, the local fluctu-

State	$a_t m_{eff}$	Operator	Fit Region	$\chi^2_{P_{DOF}}$
$0^{-+}$	$0.0680^{+7}_{-7}$	$\gamma_5$	[15, 20]	0.0002
$1^{--}$	$0.1169^{+11}_{-12}$	$\gamma_z$	[15, 20]	0.01
$0^{++}$	$0.1219^{+61}_{-55}$	1	[17, 21]	0.0001
$1^{+-}$	$0.1788^{+10}_{-11}$	$\gamma_5 p_z$	[15, 21]	0.05
$1^{++}$	$0.1699^{+10}_{-11}$	$(\vec{\gamma} \times \vec{p})_z$	[16, 21]	0.09
$2^{++}$	$0.1732^{+11}_{-11}$	$\gamma_z p_x + \gamma_x p_z$	[15, 20]	0.14
$2^{-+}$	$0.2548^{+16}_{-15}$	$\gamma_5 (s_1 - s_2)$	[11, 19]	0.27
$1^{-+}$	$0.3051^{+33}_{-32}$	$(\vec{\gamma} \times \vec{u})_z$	[14, 21]	0.44

Table 4.8: Table of effective masses, using uncorrelated fits, for the states in Fig. (4-2). Also shown is the operator used to obtain them, the fit region and the  $\chi^2$  per degree of freedom.

ations affect our perception of this. Also in this figure we show the first excited state of the same lattice operators. These are in the  $T_1^{+-}$  and  $T_1^{++}$  lattice representations and their first excited states correspond to  $J^{PC}$  values  $3^{+-}$  and  $3^{++}$ . We note that, while a clear signal is apparent to the centre of the lattice, the effective mass does not plateau. This is another indication that the lattice volume needs to be increased since we have higher state contributions to the correlation function at all times, making it difficult to extract a reliable effective mass. This manifests itself in as a characteristic slow downwards drift in the effective mass plots that can be seen for all states (at the appropriate scale). This drift can be seen for both the  $1^{+-}$  and  $1^{++}$   $P$ -states in Fig. (4-3) and also for the  $1^{--}$   $\rho$  meson in Fig. (4-4).

Increasing the volume to counteract this effect should help us to resolve  $P$ -wave splittings further and allow us to fit in extended regions.

In Fig. (4-4) we show an example of the how the overlap with state of interest depends on the operator used. We plot the effective mass of the  $\rho$  meson as determined from each of the three types of operator listed in Table 4.6. We note that the overlap with the quark bilinear and staple operators are the same within error but that the operator which uses the chromomagnetic field has larger contamination from higher states, and poorer error behaviour. This behaviour might also indicate that the  $1^{-+}$  operator may still not have sufficient overlap with the hybrid exotic state of interest and another improved operator may be required for higher accuracy measurements.

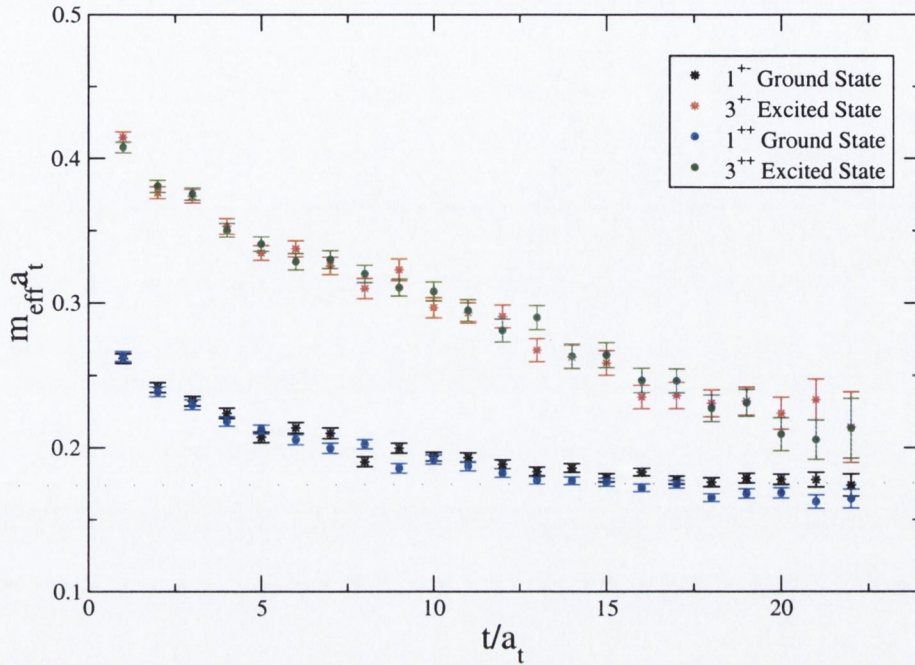


Figure 4-3: The ground and first excited states of the  $T_1^{+-}$  and  $T_1^{++}$  lattice operators. The ground states correspond to  $J^{PC}$  values  $1^{+-}$  and  $1^{++}$ , the excited states correspond to  $3^{+-}$  and  $3^{++}$ .

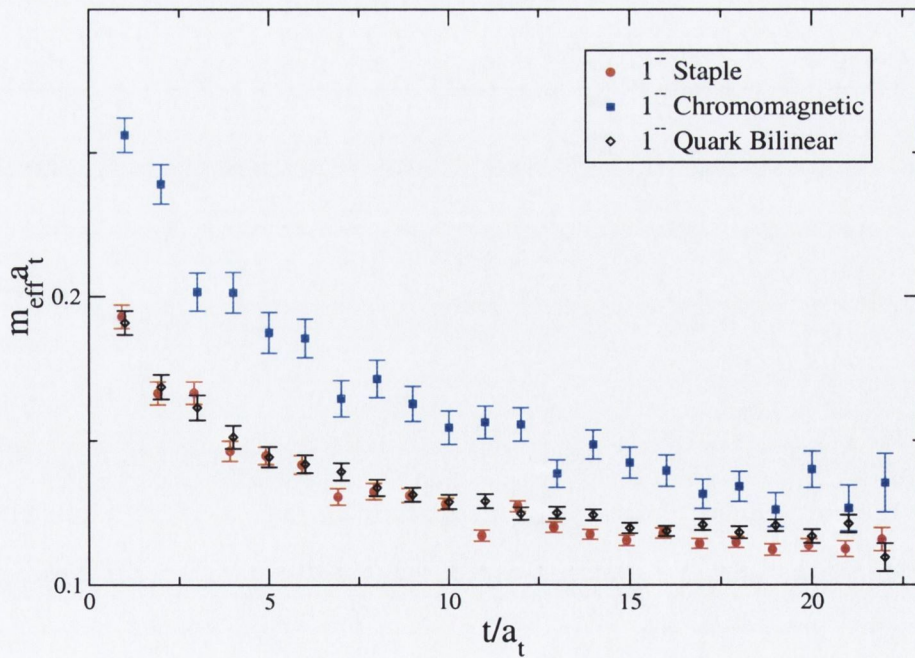


Figure 4-4: Effective masses for the  $\rho$  ( $1^{--}$ ) meson using the three different interpolating operators as described in Table 4.6.

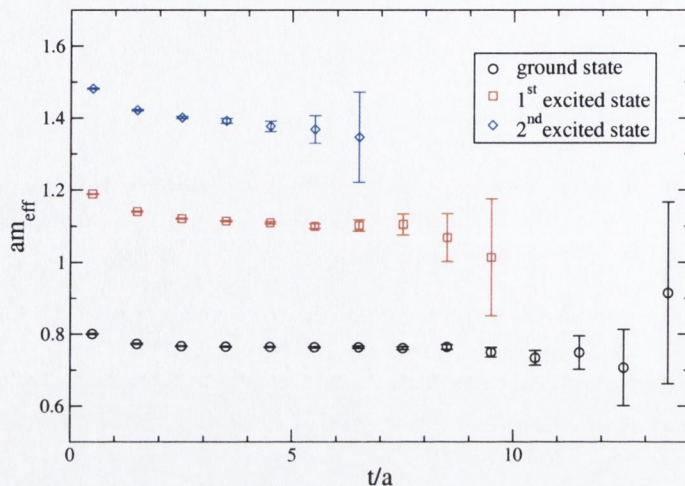


Figure 4-5: Effective masses for the three lowest-lying states of the static-light S-wave.

## 4.5.2 Static-light Mesons

The simulation of hadrons containing one or more heavy quarks,  $Q$ , can be problematic for lattice calculations because systematic errors which scale with the quark mass can make simulations with isotropic relativistic actions unreliable. The static limit, where  $m_Q \rightarrow \infty$ , is the lowest order term in a  $\frac{1}{m_Q}$  expansion of the Heavy Quark Effective Theory (HQET) Lagrangian [51]. In this limit the approximate heavy quark spin and flavour symmetries become exact. Although it is believed that calculations in this limit can be relevant to  $b$ -physics, historically the signal-to-noise ratio in static-light correlation functions has been particularly poor. Estimates of all-to-all propagators have been used in previous static-light systems since they lead to an increase in statistics by placing source and sink operators at every spatial site on the lattice [33, 52].

A detailed analysis of the construction of operators, and results from simulations using the dilute all-to-all propagator technique, for this system can be found in [53]. Here, we illustrate the effectiveness of the method in Fig. (4-5) for a quenched simulation of the static-light S-wave meson with the parameters given in Table 3.5 [28].

We simply note that the high resolution of the signal allows us to accurately obtain the ground, first *and* second excited states by use of the variational method with five operators differing by the smearing parameters of the light quark.

## 4.6 Isoscalar mesons

In a classical field theory, symmetries of the Lagrangian must be reflected by symmetries of the physical phenomena which such a theory is supposed to describe. In a quantum field theory this is not necessarily true, since quantum fluctuations of the vacuum can spoil the classical symmetries. However, one then expects to obtain remnants of this symmetry breaking in physical observables, e.g. the occurrence of (massless) Goldstone bosons in the case of a spontaneously broken global symmetry.

The  $U(1)$  flavour symmetry of the QCD Lagrangian predicts baryon number conservation, which is well realised in nature. Likewise, we would expect an ‘*axial* baryon number conservation’, i.e., a parity doubling of the baryon states from the  $U_A(1)$ . Since the particle spectrum does not exhibit such a parity doubling, one would suppose that the symmetry is broken spontaneously. However, there is no light pseudoscalar meson which could be identified with the corresponding Goldstone boson. The  $\eta'$  has the correct quantum numbers but is simply too heavy. This is the so-called  $U(1)$  problem of QCD: The  $U_A(1)$  symmetry of the QCD Lagrangian seems to be broken by quantum fluctuations, but apparently there is no remnant of this symmetry breaking visible in the particle spectrum.

A possible solution to this problem came from G.’t Hooft [58], who showed that non-trivial excitations of the vacuum, instantons, can produce a non-vanishing contribution to physical observables. Since flavour singlet phenomena seem to be so closely related to the quantum structure of the vacuum it seems appropriate to utilise models of the QCD vacuum in attempting to understand them.

Instantons are classical solutions to the euclidean equations of motion. From them a crude picture of quark motion in the vacuum can be formulated. Instantons act as a potential well, in which light quarks can form bound states (the zero modes). If instantons form an interacting liquid, quarks can travel over large distances by hopping from one instanton to another, similar to electrons in a conductor. Just like the conductivity is determined by the density of states near the Fermi surface, the quark condensate is given by the density of eigenstates of the Dirac operator near zero virtuality. If the distribution of instantons in the QCD vacuum is sufficiently

random, there is a non-zero density of eigenvalues near zero and chiral symmetry is broken. Previous calculations show that removing non-instanton components of the gluon configurations by cooling [59] reproduces the essential features of the instanton model, and observables calculated with all gluons are similar to those obtained using only instantons that survive cooling [63].

The authors of [55] take a step toward confirming the conventional wisdom that the flavour singlet  $\eta'$  receives its special mass from instantons by sorting the gauge fields into bins of their topological charge,  $Q$ . The large  $N_c$  approximation gives qualitative understanding that the strength of the flavour singlet interaction  $m_0^2$  (or singlet/non-singlet mass gap,  $m_0^2 = m_{\eta'}^2 - m_\pi^2$ ) is linked to instantons. To leading order in  $1/N_c$  one finds the Witten-Veneziano formula [56, 57],

$$m_0^2 = \frac{2N_f\chi}{f_\pi^2}, \quad (4.24)$$

where  $N_f$  is the number of flavours,  $\chi$  is the topological susceptibility and  $f_\pi$  is the pion decay constant.

The fermionic zero-modes are associated with the topological charge of a gauge configuration via the index theorem. In the continuum, integrating out the anomaly equation of the flavour singlet axial vector current gives the relation

$$Q = m\text{tr}(\gamma_5 S_F) \quad (4.25)$$

where  $S_F$  is the fermion propagator. Resolving the propagator in a sum over eigenmodes of  $\mathcal{D}$ , and noting that all modes with a nonzero eigenvalue come in conjugate pairs, one gets the index theorem:

$$Q = n_+ - n_-, \quad (4.26)$$

where  $n_+(n_-)$  are the number of positive(negative) chirality zero-modes. If the  $\eta'$  is particularly sensitive to the topological charge of a configuration, then one must also expect it to be sensitive to the presence or absence of fermionic zero-modes.

On the lattice, both sides of the index equation are slightly distorted. The flavour singlet  $\gamma_5$  does not exactly commute with  $\mathcal{D}$ , so the trace of  $\gamma_5 S_F$  cannot be collapsed into a trace in the zero-mode sector alone. Further, due to the Wilson term there are no exact zero-modes, nor is there an exact definition of topological charge. Nevertheless, if we are sufficiently close to the continuum, we should obtain something like the conventional picture. The importance of the eigenmodes and the influence of the topological charge has been investigated in [26, 25]. The value of the topological charge as determined from the field theoretical definition and that of the fermionic determination above has been investigated in [27] with strong correlations observed between the two, indicating that index theorem may still remain valid on the lattice.

The advantages of the hybrid all-to-all propagator method should prove two-fold in this scenario. We should have the benefit of the self-averaging effects of translational invariance in the calculation of the disconnected correlation as well as explicitly including the important low-modes of the Dirac operator.

#### 4.6.1 Flavour Singlet Correlation Functions

Let us consider an  $N_f$  flavour meson with the interpolating operator  $P = \sum_i \bar{\psi}_i \Gamma \psi_i$ , where the sum is over the number of flavours. The time dependence of the momentum zero projection of its propagator is given by

$$G_P(0, t) = \sum_{\mathbf{x}} \left\langle \sum_i \bar{\psi}_i(\mathbf{0}, 0) \Gamma^\dagger \psi_i(\mathbf{0}, 0) \sum_j \bar{\psi}_j(\mathbf{x}, t) \Gamma \psi_j(\mathbf{x}, t) \right\rangle. \quad (4.27)$$

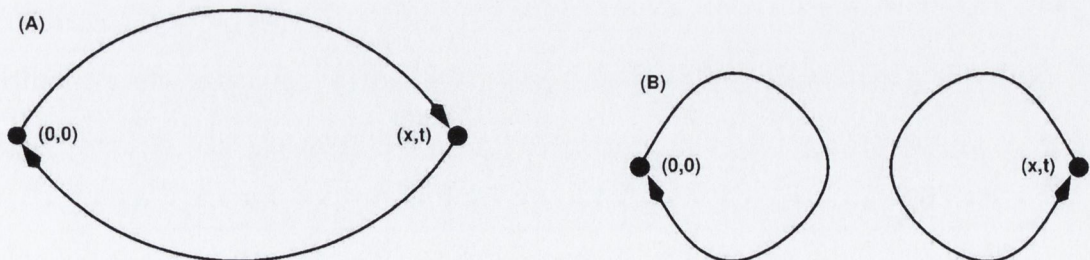


Figure 4-6: (A) are the connected contributions to the propagator and (B) are the disconnected contributions.

If we now perform all possible contractions of the quark operators  $\psi$  we will get

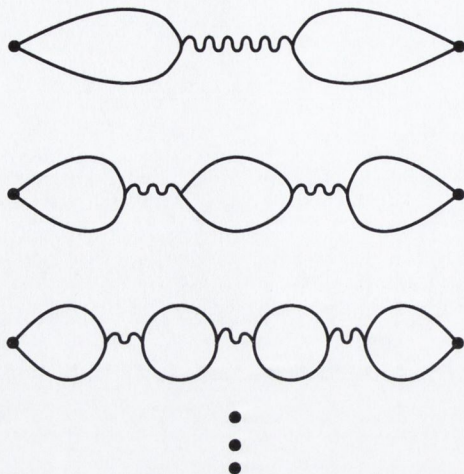


Figure 4-7: Vacuum effects on disconnected diagrams

$N_f$  contributions to the propagator from terms like

$$\left\langle \overbrace{\sum_i \bar{\psi}_i(\mathbf{0}, 0) \Gamma^\dagger \psi_i(\mathbf{0}, 0)} \underbrace{\sum_j \bar{\psi}_j(\mathbf{x}, t) \Gamma \psi_j(\mathbf{x}, t)} \right\rangle. \quad (4.28)$$

These terms are called connected terms since the meson states at time 0 and  $t$  are explicitly connected by quarklines and have the graphical representation of (A) in Fig. (4-6). We will also get  $N_f^2$  contributions to the propagator from terms like

$$\left\langle \overbrace{\sum_i \bar{\psi}_i(\mathbf{0}, 0) \Gamma^\dagger \psi_i(\mathbf{0}, 0)} \sum_j \overbrace{\bar{\psi}_j(\mathbf{x}, t) \Gamma \psi_j(\mathbf{x}, t)} \right\rangle. \quad (4.29)$$

Correspondingly these second terms are called disconnected and have the graphical representation of (B) in Fig. (4-6). Note that these terms violate the OZI rule. They are highly sensitive to the details of the vacuum structure since the correlation between the quark loops at time 0 and  $t$  is mediated by quantum effects, multiple gluons and internal quark loops which we represent graphically in Fig. (4-7). In the quenched approximation only the first (hair-pin) interaction occurs.

The physical light mesons are 2-flavour triplet (pions for the pseudo scalar), 3-flavour octet (Kaons,  $\eta$  for the pseudo scalar) or 3-flavour singlet ( $\eta'$  for the pseudo scalar) combinations of quarks. Due to the Wick contraction procedure, one expects the disconnected contributions to cancel each other largely for the non-singlet

combinations (up to a presumably negligible flavour symmetry breaking they cancel exactly), and to contribute additively to the singlet state. From this point of view we can identify the connected contribution with the normal ‘Goldstone’ part of the mesons and the disconnected contribution with the anomalous topological part.

For isoscalar mesons we must, therefore, include a disconnected correction to the correlation function of Eq. (4.4),

$$C_{(I=0)}^{BA}(\mathbf{p}, \Delta t) = -\frac{1}{L^3 T} \sum_t \left( \sum_{i,j} \mathcal{O}_{[2,1]}^{(j,i)B}(\mathbf{p}, t + \Delta t) \mathcal{O}_{[1,2]}^{(i,j)A}(\mathbf{p}, t) - N_f \mathcal{O}_{[2,2]}^B(\mathbf{p}, t + \Delta t) \mathcal{O}_{[1,1]}^A(\mathbf{p}, t) \right), \quad (4.30)$$

where  $\mathcal{O}_{[r,r]}^\Gamma(\mathbf{p}, t)$  is simply a trace over the hybrid list indices of the meson operator of Eq. (4.3) with identical noise vectors.

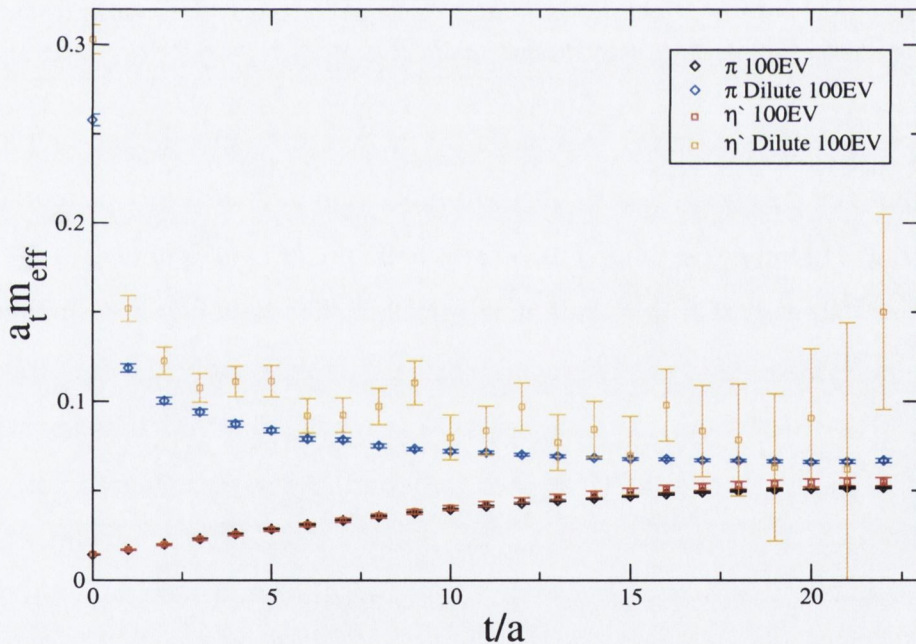


Figure 4-8: Effective masses for isovector and isoscalar  $0^{-+}$  meson with 100 eigenvectors, time and colour dilution and 250 dynamical anisotropic configurations. Also included is the calculation with 100 eigenvectors only.

Using the simulation detailed in Table 4.7, we calculate the correlation functions of both the  $0^{-+}$  and  $0^{++}$  isoscalar mesons. We can see the effective mass of the  $\eta'$  in Fig. (4-8). For comparison, also plotted is the isovector meson, the pion, and

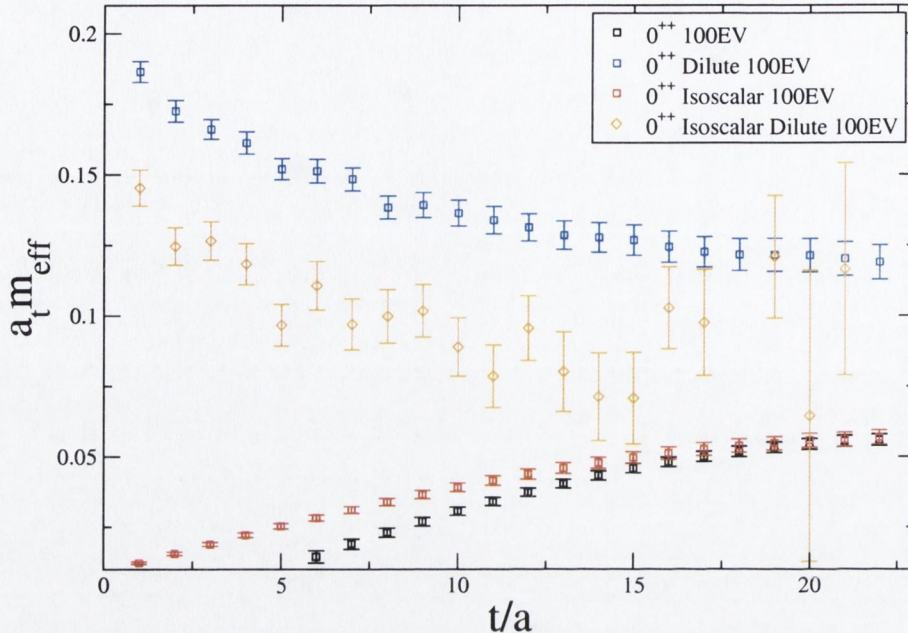


Figure 4-9: Effective masses for isovector and isoscalar  $0^{++}$  meson with 100 eigenvectors, time and colour dilution and 250 dynamical anisotropic configurations. Also included is the calculation with 100 eigenvectors only.

the same two states determined using only eigenvectors. One of the first points to note is that the effective mass of the pion determined from the two methods does not overlap. This may be due to an insufficient number of eigenmodes used in the calculation or another manifestation of the insufficient temporal extent of the lattice.

The noise introduced by the disconnected correction is doomed to be large at large Euclidean time since it involves differences of terms whose errors increase with time. We can see this for the hybrid propagator, where the errors, which are relatively large to begin with, grow with increased time. Again we note however that while the hybrid method  $\eta'$  appears extremely noisy it is possible to obtain a fit of  $a_t m_{eff} = 0.0808_{-36}^{+37}$  with  $\chi_{P_{DOF}}^2 = 0.026$ . This corresponds to a mass of  $\sim 503$  MeV which, again, is in good qualitative agreement with that of Ref. [60] and Ref. [61], who measured  $\sim 520$  MeV and  $\sim 823$  MeV respectively. One would hope that increased dilution combined with a slightly higher number of eigenvectors and a larger lattice volume would help resolve the mass to high accuracy.

In Fig. (4-9) we have an identical plot for the case of the  $0^{++}$  isovector and isoscalar mesons. We observe a large discrepancy between the effective masses determined

from the eigenvector and hybrid methods for the isovector states which again would indicate that additional eigenvectors might increase the accuracy of our results and that a larger temporal extent is required. Similar to the  $0^{-+}$  case we observe large errors for the isoscalar particle which increase with  $t$ . The mass-gap, while not resolved with accuracy according to this effective mass plot, is obvious. Notably, the isoscalar state is lighter than the isovector state. Performing a fit to this state yields  $a_t m_{eff} = 0.0838_{-33}^{+38}$  with  $\chi_{PDof}^2 = 0.038$ .

We note that the lattice operator used for this state was the identity operator which, as previously discussed, one would expect in general to have a poor overlap with the  $0^{++}$  state. That the disconnected correction is so large is also a puzzling aspect of this operator. It will be interesting to see whether this behaviour persists on a larger lattice volume.

The signals we obtain for both isoscalar states are still not entirely satisfactory. It seems apparent that additional dilution and eigenvectors, as well as a larger lattice volume, are required to increase the accuracy of these results. The influence of the topology of the gauge fields has not been explored directly either and determinations of topological charge of configurations and the dependence of mass gap on this would be interesting studies to carry out in the larger volume case.

## 4.6.2 Mixing of Scalar Glueballs and Flavour-Singlet Scalar Mesons

In quenched QCD there are two distinct types of scalar meson:  $q\bar{q}$  mesons and scalar glueballs. In full QCD these two types of state will mix and on a lattice, much as in experiment, one will obtain the mass values of the resulting mixed states. The correlation of the mixed element of a final state is given by

$$C^A(\Delta t) = \sum_t \phi(t + \Delta t) \mathcal{O}_{[1,1]}^A(t), \quad (4.31)$$

where  $\phi$  is the scalar glueball operator of interest.

The significance of this mixing has been investigated by Ref. [65] who found

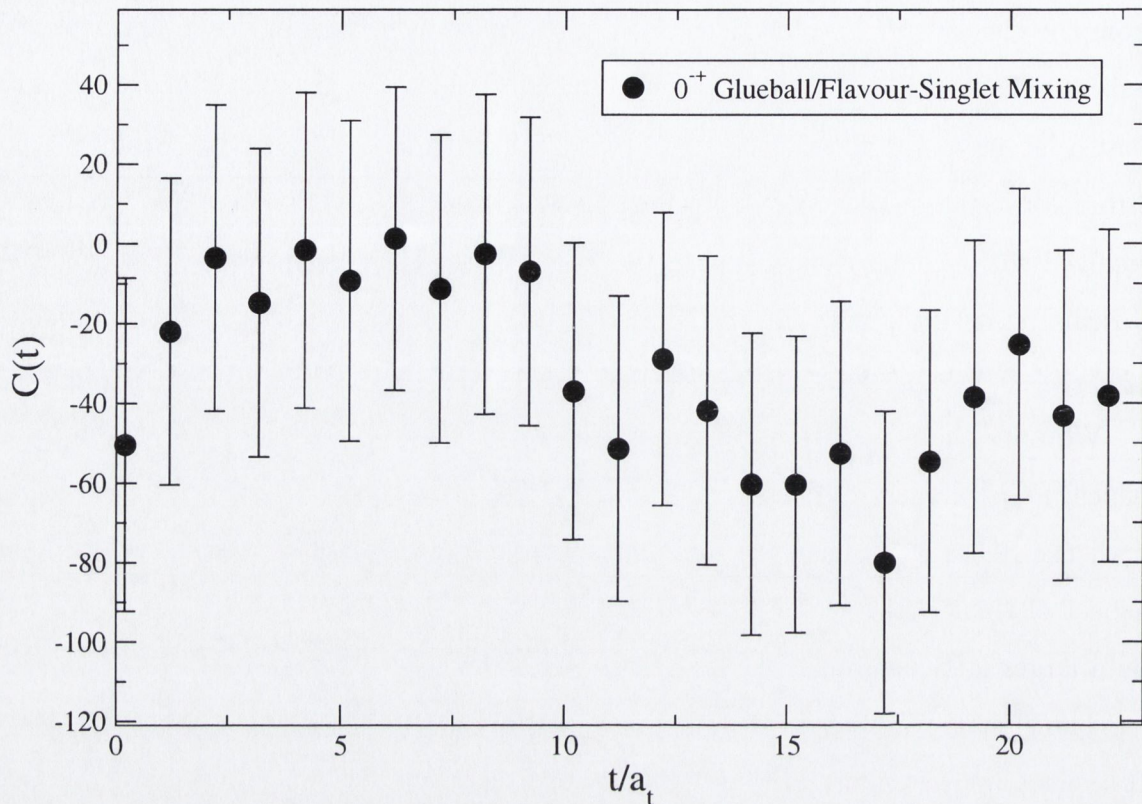


Figure 4-10: Correlation of the mixing of the  $0^{-+}$  glueball with the  $0^{-+}$  flavour-singlet meson.

that, when physical states are considered as mixed states, analysis supported the interpretation of  $f_0(1710)$  as composed mainly of the lightest scalar glueball. Ref. [66] also showed how mixing could be explored in a lattice study, in particular for the case of the scalar meson and the scalar glueball, and found that the mixing could have large effects (albeit with large systematic errors) on the meson mass as determined in full QCD.

We evaluate this mixing correlation for the simulation of Table 4.7 for both the  $0^{-+}$  and  $0^{++}$  states. The result for the  $0^{-+}$  state can be seen in Fig. (4-10). We can see that the correlation is zero within errors. That the mixing of the  $\eta/\eta'$  with the pseudoscalar glueball is small is most likely because their mass difference is large.

There appears to be a large mixing for the  $0^{++}$  state however, which can be seen in Fig. (4-11). This preliminary calculation supports the conclusions of Refs. [65, 66] to some extent. While there are large statistical errors on this result, it is still extremely

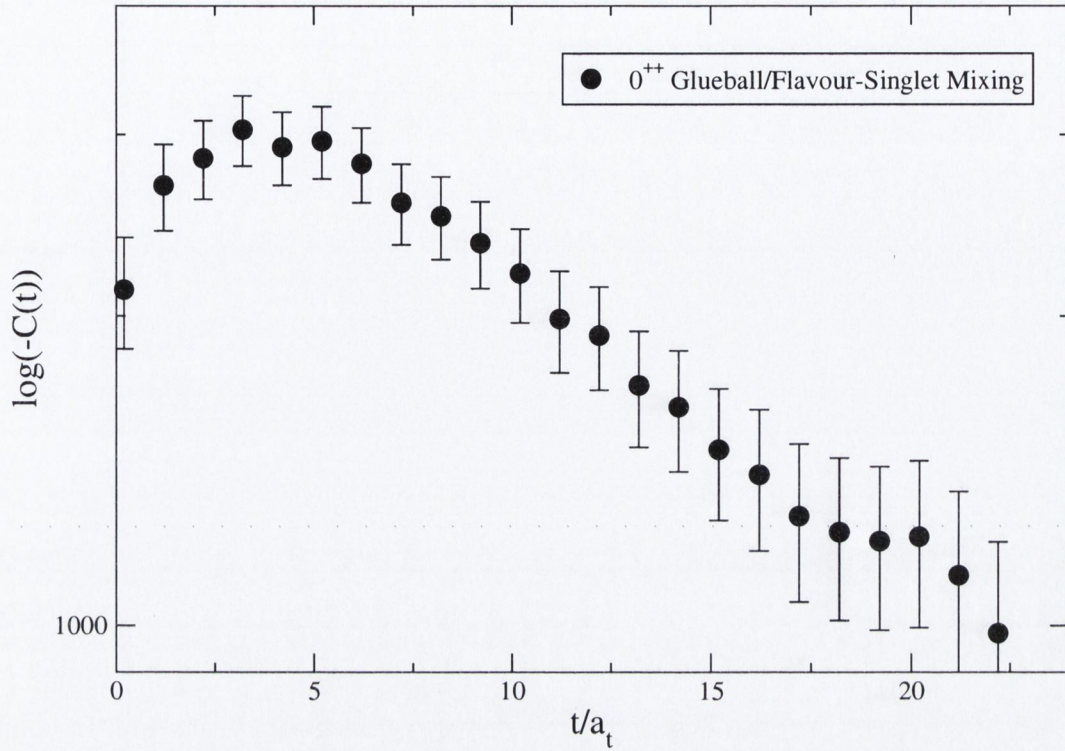


Figure 4-11: Correlation of the mixing of the  $0^{++}$  glueball with the  $0^{++}$  flavour-singlet meson.

interesting. Applying a fit to this figure yields an effective mass of  $a_t m_{eff} = 0.097_{-9}^{+11}$  with  $\chi_{P_{DOF}}^2 = 0.5$ . This is merely the starting point for the mixing calculation but would seem to be a potentially fruitful avenue of research.

# Chapter 5

## Conclusions

In this thesis, we have concerned ourselves primarily with improving the accuracy of the determination of correlation functions in lattice QCD. We have detailed two avenues of improvement and have implemented them both separately and in combination.

The first was the use of an improved anisotropic action which is classically correct to  $O(a_s^3, a_t^2)$ . The employment of an anisotropic lattice introduces the anisotropy ratio,  $\xi = a_s/a_t$ , which we tune non-perturbatively. In a quenched lattice simulation, we found that the mass dependence of the tuning of this parameter was weak and a single tuning would suffice for a range of quark masses from the strange quark mass to well above charm quark mass. For a simulation with dynamical fermions we saw that the tuning procedure was more difficult due to the fact that the anisotropy parameter must be tuned *simultaneously* for both the gauge and the quark actions.

The signal for a correlation function falls as  $\sim e^{-E_0 t}$  for large  $t$ , where  $E_0$  is the ground state. The primary benefit an anisotropic action is that it allows us an increased number of lattice sites in the temporal direction with which to study this dependence. For low  $t$ -values the correlators contain contamination from higher states and anisotropic lattices allow us to accurately determine when these states cease to significantly contribute and in what region it is possible to accurately extract the ground state mass.

The second improvement was in the accuracy of the determination of the cor-

relation function itself. This involves the computation of the full lattice Feynman propagator,  $S_F$ , or *all-to-all* propagator. A common simplification is to use the hermiticity property  $(\gamma_5 S_F)^\dagger = \gamma_5 S_F$ , to reduce this to the calculation of a single column of the propagator, a *point-to-all* propagator. We noted that this neglects the self-averaging effects of the translational invariance of the lattice and also limits the available physics.

We proposed and implemented a novel procedure for calculating the all-to-all propagator. This is a hybrid method that combines the dominating effects of the low-lying fermion modes (for light quarks) with a stochastic estimation technique, *dilution*, that gives the exact inverse in a finite number of steps. This maintains the reflection positivity of the propagator, which in turn allows us to apply variational techniques in our determination of effective masses of correlation functions.

In quenched Wilson simulations, we found that it was possible to dramatically reduce the errors of correlation functions with different dilution combinations and ultimately to a level of gauge field noise. The dominance of the low-lying eigenmodes was found to depend strongly on the quark mass but, for sufficiently light quarks, their use in union with a diluted stochastic correction gave even further decreases in error, particularly for traditionally noisy states.

Each of these methods give significant, and independent, improvements in their own right. In combination however, exploratory dynamical quark studies show dramatic and highly promising results. Using the two methods in combination we found that it was possible to achieve high accuracy mass determinations for all states attempted, including a hybrid exotic meson. The level of accuracy achieved also allowed the determination of both a first and second excited state in a static-light study using the variational technique.

Use of the all-to-all propagator technique also allowed us to determine disconnected diagram contributions to both the  $0^{++}$  and  $0^{-+}$  isoscalar mesons and extract masses for both these states.

These results indicate that these methods are promising avenues of research and future work will involve their use on larger lattice volumes and a range of quark

masses. The significance of specific dilution schemes is also yet to be fully determined but certainly time-dilution appears to be essential in a stochastic estimation procedure.

The methods employed here are also applicable to systems other than mesons. It is hoped in the near future to extend this work to include baryons, decays and electroweak insertions. Further work will also continue on static-light and charm systems as well as dilutions more suited to disconnected diagrams.

# Appendix A

## Algorithm Implementation

There are two main, interconnected matters associated with the implementation of the hybrid all-to-all propagator method, computational cost and data storage. There are also three stages in the generation of correlation functions themselves, that of the generation of the propagator data, creating the *meson operators* and the computation of the meson correlation functions.

### A.1 Propagator Data

The dilution procedure is straightforward in the sense that, once a dilution level is defined, we simply take a noise vector, dilute it and perform the associated number of conjugate gradient inversions. For example, for a time and colour dilution level, we would perform  $NT * 3$  (where there are  $NT$  time slices) conjugate gradient inversions. If we are creating mesonic correlation functions this must be repeated for each of the constituent quarks. The cost of these inversions is dependent on the quark mass with a critical slowing down for light quark mass. So, to some extent, the dilution level is limited by the amount of computational time we are willing to spend generating the diluted data.

Of course, by the inclusion of the low-lying eigenvector projection, it is possible for us to lower the condition number of the hermitian Dirac matrix  $Q$  and thereby speed up the inversions. Note that we do not lower the condition number of the Dirac

matrix,  $M$ , and that the conjugate gradient inversions *must* be performed with the hermitian matrix  $Q$  for a computational speed-up effect.

Apart from the computational cost, there is also an issue with the storage of the propagator data. If we have an ensemble of 250 configurations with time-colour dilution above for a  $8^3 \times 48$  lattice then we require space to store

$$250 \times NT \times N_{\text{COLOUR}} \times N_{\text{QUARKS}}$$

quark field vectors. The size of each quark field for a lattice of this volume is roughly  $4.6\text{MB}$ . To store this data requires roughly  $330\text{GB}$ . If it were not for the fact that it is possible to store the diluted noise vectors as a single quark field we would require twice this amount of storage. If we wanted to, for example, increase the dilution level to include spin, this data storage requirement would increase by a factor of 4. Similarly, each eigenvector is a quark field and must also be stored, particularly if we wish to use them to lower the condition number of  $Q$ , although the scaling is not so severe.

If the conjugate gradient inversions are computationally cheap, such as for heavier masses, then there is no need to store the noise data and we can regenerate data as required. The lighter the quark mass we require, the more important it becomes to store the data. However, as we noted, the lighter the quark mass the more dominant the eigenvectors, and a high level of dilution may not be required for accurate results.

## A.2 Meson Operators

Firstly, we remind ourselves of our definition of a meson operator (from Section 4.1)

$$\mathcal{O}_{[r,s]}^{(i,j)A}(\mathbf{p}, t) = \sum_{\mathbf{x}} e^{i\mathbf{p}\cdot\mathbf{x}} \mathcal{O}_{[r,s]}^{(i,j)A}(\mathbf{x}, t), \quad (\text{A.1})$$

where

$$\mathcal{O}_{[r,s]}^{(i,j)A}(\mathbf{x}, t) = \text{Tr}(w_{[r]}^{(i)}(\mathbf{x}, t)^\dagger \gamma_5 \Gamma^A u_{[s]}^{(j)}(\mathbf{x}, t)), \quad (\text{A.2})$$

and the trace is over the suppressed spin and colour indices and  $n = +1$  ( $n = -1$ ) for a creation (annihilation) operator. We focus initially on the disk space required to store this object. The final object contains a temporal index and two hybrid list indices for each operator  $\Gamma^A$  and each momentum  $\mathbf{p}$ . A matrix formed from a combination these indices will contain many zeros however. Since time-dilution has been used as a minimum dilution level our hybrid lists are at least of length  $NT$ , on each time timeslice of a meson operator only the terms that are in the timeslice subspace  $t$  are non-zero in the  $w$  hybrid list. So, although the  $i$  index extends over the full hybrid list, we only need to store a  $1/NT$  fraction of this matrix. When we include eigenvectors, this argument is still valid to a large extent and in this more general case the number of elements in a meson operator is

$$(N_{ev} + \frac{N_{dil}}{NT})(N_{ev} + N_{dil}) \times NT,$$

where  $N_{ev}$  are the number of eigenvectors and  $N_{dil}$  is the number of dilution elements in the hybrid list. Note that the number of elements in a hybrid list is given by  $N_{ev} + N_{dil}$ .

The typical size for such an array is heavily dependent on the dilution level used and the number of eigenvectors. The dimensions of the lattice volume *only* appear in the temporal extent as  $NT$ , both explicitly and also within  $N_{dil}$ . For the largest dilutions level possible (under the schemes applicable from Table 3.1) on a  $8^3 \times 48$  lattice with 100 eigenvectors, a meson operator would require about  $680MB$  of storage space. Without this compactification we would have required over  $16GB$  of storage.

There are also large computational savings to be made using the same method. We shall use the same estimate of the propagator for many different operators  $\Gamma^A$  in Eq. (A.2). In general  $\Gamma^A$  will be composed of three parts, a smearing on each quark field and the interpolating operator,

$$\Gamma^A = S^w \Gamma S^u$$

where  $S^w$  is the smearing on the  $w$  hybrid list,  $S^u$  is the smearing on the  $u$  hybrid list

and  $\Gamma$  is the interpolating operator. Normally we will have a set of different smearing that we would like to try as well as a set of interpolating operators.

In Eq. (A.2), since the  $w$  hybrid list has only  $(N_{ev} + \frac{N_{dil}}{NT})$  non-zero elements (on timeslice  $t$ ) it is possible to store these non-zero elements in RAM. In practice, the number of  $w$  hybrid list smearings,  $N_{smear}^w$  and the number of operators  $N_\Gamma$  can be chosen so that it is possible to store

$$N_\Gamma \times N_{smear}^w \times (N_{ev} + \frac{N_{dil}}{NT})$$

quark field time slices in RAM, where we think of  $S^w$  and  $\Gamma$  as acting to the left in Eq. (A.2). We then read each element of the  $u$  hybrid list quark field timeslice one at a time and apply the smearing operations  $S^u$  acting on this timeslice. The inner product of this set of quark field timeslices is then performed with our stored set of quark field timeslices and the meson operator arrays are filled in this manner.

The computational saving of this system is enormous. If we consider a set of, for example,  $N_{smear}^w = 3$ ,  $N_\Gamma = 3$  and  $N_{smear}^u = 3$  and an  $8^3 \times 48$  lattice with maximum dilution and 100 eigenvectors, instead of applying over 28 billion operations on quark field timeslices we apply just over 750000. If we include the possible momenta factors the effect is even more pronounced.

The only overhead is that since the data is computed in chunks for each meson operator, it must be written to disk as we cycle through the elements of the  $u$  hybrid list since we have no available storage in RAM. In practice, this overhead is negligible.

### A.3 Correlation Functions

Correlation functions are calculated using

$$C^{BA}(\mathbf{p}, \Delta t) = -\frac{1}{L^3 T} \sum_{i,j,t} \mathcal{O}_{[2,1]}^{(j,i)B}(\mathbf{p}, t + \Delta t) \mathcal{O}_{[1,2]}^{(i,j)A}(\mathbf{p}, t). \quad (\text{A.3})$$

There is little difficulty in making correlation functions from the meson operators if they are stored as described above. In their uncompactified format it would be

impossible, for a large number of dilutions, to store two meson operators simultaneously in RAM on a serial computer. With the above method however, only extremal circumstances would not allow two to be held in the  $2GB$  of RAM available on most workstations.

## A.4 A Black Box

Perhaps the most appealing aspect of the hybrid method is that it requires very little external input to start generating results. It needs only the gauge field configurations, the conjugate gradient inverter for the required action and an operator. With just these few objects it is possible for it to produce a precise result.

The all-to-all propagator method simplifies operator construction and these operators are added to the algorithm simply as an external function which takes a quark field timeslice as an argument, performs the operation and returns a resultant quark field timeslice. It is possible to add the action in an identical manner and use an in-built inverter.

Ultimately, the user does not need to know anything about the inner workings of a suite of code that employs the hybrid all-to-all propagator method. One can simply supply this small amount of information and gather the results from this black box.

# Bibliography

- [1] H. J. Rothe, World Sci. Lect. Notes Phys. **59** (1997) 1.
- [2] R. Gupta, arXiv:hep-lat/9807028.
- [3] H. B. Nielsen and M. Ninomiya, Nucl. Phys. B **193** (1981) 173.
- [4] K. G. Wilson, CLNS-356 *Presented at Cargese Summer Inst., Cargese, France, Jul 12-31, 1976*
- [5] G. P. Lepage, arXiv:hep-lat/9607076.
- [6] K. Symanzik, Nucl. Phys. B **226**, 187 (1983).
- [7] Parisi, High Energy Physics 1980, AIP Conference Proceedings No. 68
- [8] G. P. Lepage and P. B. Mackenzie, Phys. Rev. D **48**, 2250 (1993) [arXiv:hep-lat/9209022].
- [9] C. Morningstar and M. J. Peardon, Phys. Rev. D **69**, 054501 (2004) [arXiv:hep-lat/0311018].
- [10] C. Morningstar and M. Peardon, Nucl. Phys. B (Proc. Suppl.) **47**, 258 (1996)
- [11] C. J. Morningstar and M. J. Peardon, Phys. Rev. D **60**, 034509 (1999) [arXiv:hep-lat/9901004].
- [12] C. Morningstar, Nucl. Phys. Proc. Suppl. **53**, 914 (1997) [arXiv:hep-lat/9608019].
- [13] C. Morningstar and M. J. Peardon, Nucl. Phys. Proc. Suppl. **83**, 887 (2000) [arXiv:hep-lat/9911003].
- [14] C. J. Morningstar and M. J. Peardon, Phys. Rev. D **56**, 4043 (1997) [arXiv:hep-lat/9704011].
- [15] M. G. Alford, W. Dimm, G. P. Lepage, G. Hockney and P. B. Mackenzie, Phys. Lett. B **361**, 87 (1995) [arXiv:hep-lat/9507010].
- [16] A. Patel, R. Gupta, G. Guralnik, G. W. Kilcup and S. R. Sharpe, Phys. Rev. Lett. **57**, 1288 (1986).
- [17] U. M. Heller, Nucl. Phys. Proc. Suppl. **47**, 262 (1996) [arXiv:hep-lat/9509010].

- [18] C. Morningstar and M. J. Peardon, Nucl. Phys. Proc. Suppl. **73**, 927 (1999) [arXiv:hep-lat/9808045].
- [19] M. G. Alford, T. R. Klassen and G. P. Lepage, Nucl. Phys. B **496**, 377 (1997) [arXiv:hep-lat/9611010].
- [20] J. Foley, A. O’Cais, M. Peardon and S. M. Ryan [TrinLat Collaboration], arXiv:hep-lat/0405030.
- [21] S. Hashimoto and M. Okamoto, Phys. Rev. D **67**, 114503 (2003) [arXiv:hep-lat/0302012].
- [22] J. Harada, A. S. Kronfeld, H. Matsufuru, N. Nakajima and T. Onogi, Phys. Rev. D **64**, 074501 (2001) [arXiv:hep-lat/0103026].
- [23] A. X. El-Khadra, A. S. Kronfeld and P. B. Mackenzie, Phys. Rev. D **55**, 3933 (1997) [arXiv:hep-lat/9604004].
- [24] M. G. Alford, I. T. Drummond, R. R. Horgan, H. Shanahan and M. J. Peardon, Phys. Rev. D **63**, 074501 (2001) [arXiv:hep-lat/0003019].
- [25] H. Neff, N. Eicker, T. Lippert, J. W. Negele and K. Schilling, Phys. Rev. D **64**, 114509 (2001) [arXiv:hep-lat/0106016].
- [26] L. Venkataraman and G. Kilcup, arXiv:hep-lat/9711006.
- [27] J. Viehoff *et al.* [TXL Collaboration], Nucl. Phys. Proc. Suppl. **63**, 269 (1998) [arXiv:hep-lat/9710050].
- [28] J. Foley, K. Jimmy Juge, A. O’Cais, M. Peardon, S. M. Ryan and J. I. Skullerud, Comp. Phys. Commun. **172**, 145-162 (2005) [arXiv:hep-lat/0505023].
- [29] S. J. Dong and K. F. Liu, Phys. Lett. B **328** (1994) 130 [arXiv:hep-lat/9308015].
- [30] W. Wilcox, arXiv:hep-lat/9911013.
- [31] G. M. de Divitiis, R. Frezzotti, M. Masetti and R. Petronzio, Phys. Lett. B **382**, 393 (1996) [arXiv:hep-lat/9603020].
- [32] Y. Kuramashi, M. Fukugita, H. Mino, M. Okawa and A. Ukawa, Phys. Rev. Lett. **71**, 2387 (1993).
- [33] C. Michael and J. Peisa [UKQCD Collaboration], Phys. Rev. D **58**, 034506 (1998) [arXiv:hep-lat/9802015].
- [34] A. Duncan and E. Eichten, Phys. Rev. D **65**, 114502 (2002) [arXiv:hep-lat/0112028].
- [35] T. L. Ivanenko and J. W. Negele, Nucl. Phys. Proc. Suppl. **63** (1998) 504 [arXiv:hep-lat/9709130] and references therein.
- [36] R. G. Edwards, Nucl. Phys. Proc. Suppl. **106**, 38 (2002) [arXiv:hep-lat/0111009].

- [37] H. Neff, Nucl. Phys. Proc. Suppl. **106**, 1055 (2002) [arXiv:hep-lat/0110076].
- [38] [www.caam.rice.edu/software/ARPACK/](http://www.caam.rice.edu/software/ARPACK/)
- [39] R. Lehoucq and D. Sorenson. Implicitly Restarted Lanczos Method (Section 4.5). In Z. Bai, J. Demmel, J. Dongarra, A. Ruhe and H. van der Vorst, editors, *Templates of the Solution of Algebraic Eigenvalue Problems: A Practical Guide*, pages 67-80, SIAM, Philadelphia, 2000.
- [40] F. Butler, H. Chen, J. Sexton, A. Vaccarino and D. Weingarten, Nucl. Phys. B **430** (1994) 179 [arXiv:hep-lat/9405003].
- [41] P. Lepage, 1989 TASI Lectures, Eds. T. Degrand and D. Toussaint, World Scientific, 1990.
- [42] M. Luscher and U. Wolff, Nucl. Phys. B **339** (1990) 222.
- [43] M. G. Alford, T. Klassen and P. Lepage, Nucl. Phys. Proc. Suppl. **47**, 370 (1996) [arXiv:hep-lat/9509087].
- [44] P. Lacock, C. Michael, P. Boyle and P. Rowland [UKQCD Collaboration], Phys. Rev. D **54** (1996) 6997 [arXiv:hep-lat/9605025].
- [45] C. Michael, Acta Phys. Polonica B21 (1990) 119.
- [46] S. Perantonis and C. Michael, Nucl. Phys. B **347** (1990) 854.
- [47] S. Gusken, Nucl. Phys. Proc. Suppl. **17** (1990) 361.
- [48] C. R. Allton *et al.* [UKQCD Collaboration], Phys. Rev. D **47**, 5128 (1993) [arXiv:hep-lat/9303009].
- [49] S. Basak *et al.*, Proc. Sci. **LAT2005** (2005) 076 [arXiv:hep-lat/0509179].
- [50] C. Bernard *et al.*, Phys. Rev. D **68** (2003) 074505 [arXiv:hep-lat/0301024].
- [51] A. G. Grozin, arXiv:hep-ph/9908366.
- [52] A. M. Green, J. Koponen, C. McNeile, C. Michael and G. Thompson [UKQCD Collaboration], Phys. Rev. D **69** (2004) 094505 [arXiv:hep-lat/0312007].
- [53] J. F. Foley, Ph. D Thesis, in preparation.
- [54] R. Morrin, M. Peardon and S. M. Ryan, arXiv:hep-lat/0510016.
- [55] Y. Kuramashi, M. Fukugita, H. Mino, M. Okawa and A. Ukawa, Phys. Rev. Lett. **72** (1994) 3448.
- [56] E. Witten, Nucl. Phys. B **156** (1979) 269.
- [57] G. Veneziano, Nucl. Phys. B **159** (1979) 213.

- [58] G. 't Hooft, Phys. Rev. D **14** (1976) 3432 [Erratum-ibid. D **18** (1978) 2199].
- [59] B. Berg, Phys. Lett. B **104**, 475 (1981).
- [60] T. Struckmann *et al.* [TXL Collaboration], Phys. Rev. D **63** (2001) 074503 [arXiv:hep-lat/0010005].
- [61] C. McNeile and C. Michael [UKQCD Collaboration], Phys. Lett. B **491** (2000) 123 [Erratum-ibid. B **551** (2003) 391] [arXiv:hep-lat/0006020].
- [62] K. J. Juge, A. O'Cais, M. B. Oktay, M. J. Peardon and S. M. Ryan, arXiv:hep-lat/0510060.
- [63] M. C. Chu, J. M. Grandy, S. Huang and J. W. Negele, Phys. Rev. D **48** (1993) 3340 [arXiv:hep-lat/9306002].
- [64] S. Bernardson, P. McCarty and C. Thron, Comput. Phys. Commun. **78** (1993) 256.
- [65] W. J. Lee and D. Weingarten, Phys. Rev. D **61** (2000) 014015 [arXiv:hep-lat/9910008].
- [66] C. McNeile and C. Michael [UKQCD Collaboration], Phys. Rev. D **63** (2001) 114503 [arXiv:hep-lat/0010019].